Modeling of Complex Chemical Reactions and Macromolecular Orientation Phenomena in Confined Geometries

Dissertation zur Erlangung des Grades
“Doktor der Naturwissenschaften”

am Fachbereich Chemie
der Johannes Gutenberg-Universität
in Mainz

vorgelegt von
Rodrigo Maghdissian Cordeiro
geboren in Brasilien

Mainz, 2007

Tag der mündlichen Prüfung: 22.05.2007

Die vorliegende Arbeit wurde im Zeitraum Oktober 2003 bis April 2007 am Max-Planck-Institut für Polymerforschung in Mainz angefertigt.

Contents

1

Introduction

1.1 Motivation

Nature is full of examples of molecular processes taking place under spatial restrictions. To begin with, the cell is essentially a confined environment [Minton'92]. In this sense, spatial restrictions may be a key factor cleverly explored by the cell machinery. From the technological point of view, there has been an increasing interest in chemical and physical processes taking place under confinement. Several catalysers used in industry are essentially nanoporous materials, as is the case of zeolites. In such materials, there is a huge area of contact between the catalyst surface and the reactants. This contributes to the increased rate of reactant conversion. In addition to that, the sterical hindrance imposed by the small pores may also have an impact on chemical processes. Very large molecules or those which do not have chemical affinity with the porous material are less likely to penetrate into the porous structure and be converted to products. Analogously, the generation of molecules which do not fit into the pore structure is expected to be hindered. Of course, zeolites constitute only a particular example of confined environment. Lipid vesicles, emulsions, small droplets and thin films may all be considered as confined systems. Furthermore, since its advent, the field of nanotechnology has enabled the development of new materials and engineering of new devices, and thanks to that there is today a myriad of materials whose nanoscopic structure could be explored for instance as nanoreactors. Carbon nanotubes are just one example.

Although the engineering and production of the materials cited above is already quite advanced, several basic aspects related to the chemistry and physics under space restrictions still need to be understood. The issue is complex since there are several ways according to which confinement may completely change the dynamics of a system or its equilibrium state. First, there are finite size effects associated with confinement, so that the correlation length associated with some processes may be comparable to the size of the nanoscopic system. Second, there are boundary effects in the sense that, due to space restrictions, molecules can react with a finite number of neighbors in their proximity [Provata'93]. Not to mention that physical processes like diffusion and molecular orientation may be strongly influenced by confinement as well.

There were mainly two practical questions which motivated this work and were the starting point of all other additional investigations performed here. It is known experimentally that, in thin polymer films, polymer chain segments are preferably oriented parallel to the surface of the film [Prest'79, Prest'80, Russel'83, Boese'92, Lin'93, Lin'94, Ree'94, Coburn'94, Li'97, Li'99, Lee'03, McBranch'95, Tammer'02, Koynov'04, Koynov'06]. There is a great interest in this topic because polymer films are commonly used for technological applications. It is for instance known that, in organic light emitting diodes (OLEDs), the intensity of light emitted perpendicular to the film surface depends intrinsically on the chain orientation within the film [Friend'99]. There is still a considerable need for modeling and simulation to get an improved basic understanding of the orientation phenomena and the influence of parameters such as film thickness, molecular weight and chain rigidity on the chain packing morphology of thin films. These were the main aspects we wanted to address with our simulations of macromolecular orientation in confined geometries.

Parallel to that, we were faced with an additional question dealing with interfacial phenomena in polymer films. It is known that, when a solvent droplet is placed at soluble polymer surfaces, a characteristic pattern is formed as the droplet evaporates [Sequeira'03, Gonuguntla'04, Bonaccurso'05, Sequeira'06]. The pattern has the shape of a well surrounded by a ringlike deposit. Microwells may find applications as chemical microreactors or as masks for the molding of microlenses [Sequeira'03, Bonaccurso'05, Sequeira'06]. Microwells produced by inkjet printing have been also applied in the generation of the so called *via-hole interconnections* in organic thin film transistors [Kawase'01]. We performed simulations to elucidate the

influence of molecular interactions during the process of pattern formation. In a latter stage, we combined these simulations with those dealing with polymer chain orientation to investigate the impact of chain orientation within the film on the final shape of the pattern.

In addition to these questions, following the growing interest of the scientific community in chemistry in nanoreactors, we also simulated the effect of confinement on polymerization and other complex chemical reactions in confined geometries. A summarized account of the various studies performed in this work will be given in Section (1.3).

1.2 Tasks and Strategies

The general aim of the present work is to understand aspects related to the impact of space restrictions on chemical and physical processes taking place under confinement.

Motivated by the facts exposed in the previous section, we performed in-lattice Monte Carlo simulations of physical processes and complex chemical reactions taking place in confined geometries. We adopted the so called *cooperative motion algorithm* previously developed by Pakula [Pakula'04]. With this method, it is possible to simulate systems with molecular resolution and with different degrees of complexity, ranging from simple molecules to polymer chains. Its main advantage is that molecular rearrangements are performed by the computer in a collective way, so that high density systems can be simulated in a lattice fully occupied by molecular elements.

The initial concept of this work was to model the experimentally observed chain orientation phenomena in thin polymer films. The initially proposed task was to understand by means of molecular simulations the behavior of polymer chains in thin films, focusing mainly on the aspect of macromolecular orientation induced by confinement. At this stage, we adopted a research strategy combining model calculations and experimental investigations of polymer chain orientation in order to establish structure/property relations.

Parallel to that, we became aware of the experimental effect of pattern formation at soluble polymer surfaces by droplet deposition, as described above. We

investigated this effect by means of molecular simulations in order to clarify the role of molecular interactions in the process. In a later stage, the effect of chain orientation within the film on the final shape of the pattern was also investigated.

Nevertheless, we did not restrict ourselves only to these tasks. In the course of this work, we extended our studies to other effects related to geometrical confinement. An additional task was to understand how space restrictions may influence the dynamics of chemical reactions and the respective equilibrium states. The first example of chemical reaction that we investigated was the case of reversible polymerization reactions taking place inside lamellae, pores and droplets. Later, we extended the approach to the more complex case of oscillating chemical reactions in confined geometries.

1.3 Organization

1.3.1. Basic Organization of the Present Work

The work presented here consists of several interconnected chapters. In spite of that, every chapter was written as an independent block, so that each one contains its own introductory description of the scientific background related to the topic being discussed. Furthermore, a precise account of implementation details is given in each chapter and should be considered as a complement of the general description of the Monte Carlo method given in Chapter 2. After exposition and discussion of the results, each chapter has its own section dedicated to concluding remarks. In order to guide the reader through this work, we proceed now to a summarized description of the contents of each chapter. The succession of the chapters is presented in a systematical way, not in chronological order.

1.3.2. Simulation Methods (Chapter 2)

We start by giving in this chapter a summarized description of the Monte Carlo method, with emphasis on the particular case of the *cooperative motion algorithm*, adopted here as the simulation method. The knowledge summarized in this chapter is well established. It is mainly based in the works of Landau, Binder and Pakula, in which the reader may find a more detailed and extensive treatment [Landau’00, Binder’04, Pakula’04].

1.3.3. Implementing Geometrical Confinement in Simulations (Chapter 3)

In this chapter, we provide details about how to generate confined systems in molecular simulations. In a lattice simulation, systems with the geometry of a lamella or a tubular pore are easily generated simply by using a simulation box with the appropriate shape and boundary conditions. Maybe the most important contribution of this chapter lies on the method proposed to generate small droplets as confined systems. We devised a method to simulate explicitly the liquid-vapor equilibrium in a multiphase system, i.e., we were able to generate liquid droplets at solid surfaces and in equilibrium with their own vapor. It is demonstrated that such droplets behave realistically and follow basic laws of thermodynamics. For a comprehensive account of the method, we refer the reader to a recent publication of our group [Cordeiro'05].

One of the interesting points in investigating the effect of confinement over phenomena taking place inside such droplets lies on the fact that they have soft and mobile boundaries, different from the simpler cases of lamellae and pores exposed before. Hence, it is possible to investigate for instance not only the effect that confinement has on chemical reactions taking place inside the droplet, but also possible changes in the shape of the system induced by processes taking place on it.

1.3.4. Polymerization in Nanoreactors (Chapter 4)

In this chapter, the kinetics and thermodynamics of a reversible step-growth polymerization in confined environment were studied. The effect of confinement was investigated by simulating the reaction in the systems described in Chapter 3. In the end, emphasis is given to the polymerization inside liquid monomer droplets. Polymerization reactions start from systems constituted by non-bonded monomers and the following processes are considered simultaneously and independently: molecular diffusion, polymerization and chain rearrangements preserving polymer chain connectivity. We start by comparing the equilibrium average chain length resulting from polymerization between two rigid walls with bulk polymerization. When the distance between walls decreases (keeping constant the total volume of the system), the average length of the chains decreases in comparison with the bulk system. We propose a lattice theory to explain the results and show that, as confinement increases, encounters between molecules and walls become more frequent at expense of intermolecular encounters. Since the first ones do not lead to a

chemical reaction, the polymerization rate decreases. However, bond breaking does not require encounters between two molecules and therefore its rate is not changed by the presence of the walls. As a consequence, the equilibrium constant changes as function of confinement penalizing the formation of longer chains. The effect is shown to be a function of the area/volume ratio of the reaction compartment even if the confinement geometry is more complex, as is the case for tubes or droplets. Due to the mathematical simplicity and generality of the kinetic lattice model, it could be easily extended to other kinds of reactions.

In the case of polymerization inside droplets sitting at surfaces, we observed that the contact angles after polymerization were usually higher in comparison to droplets constituted by free monomers. Droplets seem to have a tendency to decrease their own area/volume ratio and compensate the conformation restrictions imposed by confinement upon the growing chains.

1.3.5. Polymer Chain Orientation in Confined Geometries (Chapter 5)

Different from Chapter 4, now polymer chains were placed in the simulation box at the beginning and were not allowed to undergo chemical transformation. We were now not interested in the dynamics of chain growth, but in the orientation of pre-formed chains in confined environment. Simulations of chains under athermal conditions show that they are preferably oriented parallel to the surface of the film. Orientation increases as the molecular weight increases or as the film thickness decreases. As literature shows, this is in qualitative agreement with the behavior of low molecular weight polystyrene. It is demonstrated that the orientation of simulated chains results from a confinement effect, i.e. it is a function of the ratio between end-to-end distance and film thickness. The study was complemented by experimental investigations of spin-coated and drop-cast films of MEH-PPV and polyfluorene. Waveguide prism coupling and polarized optical transmission and reflection spectroscopy were used to determine the anisotropy of the refractive index of these films, which is an indication of the degree of orientation of polymer chains. With increasing molecular weight, the anisotropy of both materials is strongly enhanced. However, for MEH-PPV, the anisotropy does not depend on the film thickness in the range between 0.07 – 10 μm, which is a considerably larger range as compared to the contour length of the chains. This contradiction with the predictions from simulations

is discussed by considering additional effects that may contribute to orientation, such as interchain interactions and drying induced stresses during film preparation. For a comprehensive account of the experimental results, we refer the reader to recent publications of our group [Koynov'04, Koynov'06].

1.3.6. Patterning of Polymer Film Surfaces by Droplet Deposition (Chapter 6)

It was recently shown that it is possible to generate patterns in a soluble polymer surface by depositing on top of it a solvent droplet and letting it evaporate while substrate is being swollen. The pattern generated this way has the shape of a well surrounded by a ringlike deposit [Sequeira'03, Sequeira'06]. Here, we adopted the method proposed in Chapter 3 for the simulation of droplets sitting at surfaces and investigated the case in which the surface is soluble in the droplet. By choosing the appropriate parameters, we were able to reproduce in simulations the effect of pattern formation. At this stage, the surface was considered as being formed by single molecules. The results of the first part of this chapter can also be found in a recent publication of our group [Cordeiro'05].

In a second part, we combined the method of droplet generation exposed in Chapter 3 with the simulations of polymer chains in a thin film discussed in Chapter 5 and considered explicitly the presence of polymer chains at the surface, with emphasis given to the influence of chain orientation on the pattern formation.

1.3.7. Oscillating Chemical Reactions in Confined Geometries (Chapter 7)

Our interest in the influence of spatial restrictions on the dynamics of chemical reactions has grown after we were able to demonstrate this point in Chapter 4. Because of that, we searched for other examples of chemical reactions which could also show a strong influence of geometrical confinement. Due to their large sensitivity to reaction parameters, the so called *oscillating chemical reactions* are good candidates. Experimental examples are the Belousov-Zhabotinsky and Briggs-Rauscher reactions [Epstein'96, Kondepudi'98, Kuhn'00, Atkins'02]. They consist of a sequence of reactions comprising autocatalytic steps. If reactants are continuously fed into the reactor and the right parameters are chosen, the concentration of certain components oscillates in time.

In Chapter 7, the effect of simple geometrical confinement on a hypothetical oscillating reaction following the mechanism of the *periodically forced Brusselator*

[Hao’83, Kruel’90, Liu’96] is studied by means of lattice Monte Carlo simulations. Results were obtained for reactions taking place in the bulk and under confinement between rigid and non-interacting parallel walls. It is shown that a reaction which is chaotic in the bulk may be driven to periodicity by confinement and vice-versa, indicating that geometrical confinement may also be regarded as a bifurcation parameter. To explain the results, a lattice mean field theory is proposed. Transitions from chaos to periodicity and vice-versa occur because the reaction rate constants change as a function of confinement due to steric hindrances imposed by the walls. It is shown that the theory fits well the simulation results in the regions of the parameter space where the system is not much sensible to the noise introduced by thermal fluctuations. In order to separate noise from oscillations, the study of the time series was complemented by Fourier analysis.

2

Simulation Method

2.1 The Monte Carlo Method

2.1.1. Historical and Fundamental Aspects

During the 1940s, scientists like Fermi, Metropolis and others began considering the use of random numbers to examine different problems in Physics from a stochastic perspective [Landau'00]. Due to its probabilistic character, the method was named after the region of Monte Carlo in Monaco, which is famous for its casinos. Progresses in computational power and the versatility of the method turned computer simulations into a consistent part of scientific research. In the following we proceed to a brief overview of the Monte Carlo method. For a more detailed description of this topic, the reader may find an extensive and well established literature [Landau'00, Binder'04, Pakula'04], which was used as the main basis for the present chapter.

Regarding its applicability, the Monte Carlo method is well suited to problems which can be solved by a stochastic approach and whose solution does not depend on the rigorous and explicit consideration of Newton's equations of motion. An important advantage is that problems which are analytically intractable due to their complexity can be easily solved by the Monte Carlo method. Moreover, since the parameters in a computer simulation can be fully controlled, it is possible to isolate several simultaneous effects in a given system. The aim of Monte Carlo simulations is not to provide a curve fitting, but to control the parameters in the system and evaluate their impact on the final result. Monte Carlo simulations are also good tests for

theoretical predictions when these cannot be experimentally realized with the technology available. Particularly interesting is the possibility to simulate discretized systems with molecular resolution. Simulations in a lattice can be used to describe solids. Taking into account the necessary approximations, lattices can be also applied for liquids and gases. In the simplest cases, an atom or molecule is represented by a single lattice site. However, with the appropriate scaling of the coarse-graining, each site may represent a molecular aggregate. The motion of a fluid may be studied by considering "blocks" of fluid as individual particles, but each block will be far larger than individual molecules. Polymer chains can be simulated as well by implementing connections or bonds between different lattice sites.

During a Monte Carlo simulation of any molecular system, many microscopic states are randomly sampled and averaged. The accuracy of the result depends on the thoroughness with which the phase-space is probed. Important factors are also the quality of the random number generator, limitations of time and memory, the precision of mathematical operations performed by the computer and the statistical error. The influence of such factors tends to be minimized by progresses in computational techniques.

2.1.2. Statistical Thermodynamics – The Canonical Ensemble

In most of the cases, Monte Carlo simulations with molecular resolution deal with systems constituted by a fixed amount of particles (N), a constant volume (V) and a constant temperature (T). In the experimental reality, this would be equivalent to a closed system in equilibrium with a thermal bath. In Thermodynamics, the description of systems with fixed N, V and T is based on the statistics of the so called *canonical ensemble.* Different ensembles may be also simulated [Creutz'83], but they are outside the scope of this work. Returning to the particular case of the canonical ensemble, it can be shown that the probability that the system assumes any particular microstate is given by [McQuarrie'76, Hill'86]:

$$P_i = \frac{e^{-E_i/kT}}{\sum_j e^{-E_j/kT}}, \qquad (2.01)$$

where E_i is the energy or Hamiltonian when the system is in the *i*th state, k the Boltzmann constant and T the temperature. Equation (2.01) represents a Boltzmann distribution. The sum in the denominator is a normalization factor called partition function, which in the following will be represented as Q for simplicity. In a deeper sense, it contains all of the essential information about the system under consideration and is the central function of the canonical ensemble. Any macroscopic property M of the system can be obtained by averaging it over all the possible microstates:

$$\langle M \rangle = \sum_i P_i M_i \,. \tag{2.02}$$

By means of these arguments, thermodynamic properties like internal energy E, entropy S and free Helmholtz energy F can be easily expressed as function of the partition function Q. In the case of the internal energy:

$$\langle E \rangle = \sum_i P_i E_i = kT^2 \left(\frac{\partial \ln Q}{\partial T} \right)_{N,V} . \tag{2.03}$$

Entropy is in turn related to Ω, the number of realization possibilities of a given system. In a statistical approach this is equivalent to:

$$S = k \ln \Omega = -k \sum_i P_i \ln P_i = kT \left(\frac{\partial \ln Q}{\partial T} \right)_{N,V} + k \ln Q \,. \tag{2.04}$$

The free Helmholtz energy is then obtained by:

$$F = E - TS = -kT \ln Q \,. \tag{2.05}$$

Any quantity calculated as the average of different microstates will be associated with statistical fluctuations. The standard deviation is a measure of the spread of a given quantity in a distribution and is defined as:

$$s_M = \left(\langle M^2 \rangle - \langle M \rangle^2 \right)^{1/2} . \tag{2.06}$$

By means of the so called *fluctuation-dissipation theorem* it is possible to show for instance that the specific heat C_V is directly derived from fluctuations in energy:

$$C_V = \left(\frac{\partial E}{\partial T} \right)_V = \frac{\left\langle E^2 \right\rangle - \left\langle E \right\rangle^2}{kT^2}. \qquad (2.07)$$

It can be readily seen that the magnitude of the relative fluctuation in energy will be proportional to $N^{-1/2}$. This result shows that, in experiments with a typical closed isothermal system, the relative fluctuation is extremely small. In computer simulations, however, fluctuations become very significant due to the small system sizes. Besides that, factors such as the proximity to a critical point may also affect the magnitude of fluctuations.

2.1.3. Importance Sampling

Consider a closed system constituted by a three-dimensional lattice. Half of its sites is occupied by elements representing for instance single molecules of a given substance. These molecules are assumed to interact with each other by means of nearest neighbor interactions. The remaining elements or lattice sites are simply regarded as vacancies. Furthermore, the number of elements, the volume and the temperature will be regarded as constant, corresponding to the statistics of the canonical ensemble. It is clear that there are several ways to distribute molecules in space. Each configuration will be associated with an energy level. In order to be consistent with reality, each state must be sampled by the computer with the same frequency or importance predicted by the formalism of the canonical ensemble. Only in this way is the Monte Carlo method able to find the equilibrium condition of the system and to calculate its thermodynamic properties.

The first step is to choose an initial state. For instance, let the molecules be initially arranged in a nearly spherical cluster surrounded by empty sites. Starting from this first arbitrarily chosen state, the computer will generate a new state by choosing a random element in the lattice and changing its position with one of its neighbors, regardless of its identity. The process of creating a new state from the previous one is then repeated several times. A process in which the conditional

probability of producing a given state is independent of all states with exception of the immediate predecessor is called a *Markov process*. It is a central concept in Monte Carlo simulations. The sequence of states produced this way follows a time ordered path which is referred to as Monte Carlo time. The time-dependent behavior is described by the following master equation [Landau'00]:

$$\frac{\partial P_n(t)}{\partial t} = -\sum_m \left[P_n(t) W_{n\to m} - P_m(t) W_{m\to n} \right], \tag{2.08}$$

where $P_n(t)$ is the probability of the system being in state n at time t, and $W_{n \to m}$ is the transition rate for $n \to m$. During a given transient time, the configurations created in sequence may not be representative of the equilibrium condition. However, when equilibrium is reached, $\partial P_n(t)/\partial t = 0$ and Equation (2.08) is satisfied by setting the two terms in its right-hand side as equal. The resultant expression is known as *detailed balance*:

$$P_n(t) W_{n\to m} = P_m(t) W_{m\to n} . \tag{2.09}$$

It can be further developed by considering the probability of a state as given by Equation (2.01):

$$W_{n\to m} / W_{m\to n} = \mathrm{e}^{-(E_m - E_n)/kT} . \tag{2.10}$$

Any transition rate which satisfies detailed balance is acceptable. The first choice of rate which was used in statistical physics is the Metropolis form [Metropolis'53]:

$$\begin{aligned} W_{n\to m} &= t_0^{-1} \mathrm{e}^{-\Delta E / kT}, \qquad \Delta E > 0 \\ &= t_0^{-1}, \qquad \Delta E \le 0 \end{aligned} \tag{2.11}$$

where ΔE stays for the difference in energy between the attempted and the present state and t_0 for the time required for one motion attempt.

An example of importance sampling Monte Carlo scheme can be summarized in the following sequence of steps [Landau'00]:

1) choice of an initial state;
2) choice of a random element and a random neighbor;
3) calculation of the energy change that results if the positions of the elements are exchanged (ΔE);
4) generation of a random number r so that $0 \leq r < 1$;
5) acceptance of the new configuration and execution of the motion only if $r < \mathrm{e}^{-\Delta E / kT}$ (Metropolis test);
6) repetition of the process starting from step 2.

After a certain number of motion attempts has been considered, the system is at a specific state whose properties are determined and added to the statistical average which is being kept [Landau'00]. However, before the computer starts sampling the states for the statistical average, it is necessary to be sure that the system has had enough time to relax from the arbitrary initial condition to the equilibrium condition. In other words, the sampling procedure should start only after a given transient time, during which the thermodynamical properties of the system relax from an initial value to the equilibrium value. The thermodynamic properties at equilibrium oscillate around a mean value as function of time due to thermal fluctuations but there is no time dependence in a deterministic sense. The standard measure of Monte Carlo time is the Monte Carlo step/site (MCS/site) [Landau'00]. In other words, one time unit is considered to have passed when an average of one motion attempt per element has been performed. Once equilibrium is achieved, the algorithm described above is able to generate states with a probability distribution consistent with Equation (2.01). Following Equation (2.02), the desired averages simply become arithmetic averages over the entire sample of states which is being kept.

2.1.4. Ergodicity

A very important concept in simulations is the one of ergodicity. The formalism of the canonical ensemble considers that every state can be reached with a non-zero probability, although some of them are more probable than others. The so

called ergodicity principle states that all possible configurations of the system should be attainable. In this sense, respecting the constraints of the problem being investigated, Monte Carlo simulations must allow a complete exploration of the phase space. Only under this condition the calculated properties may be considered realistic. A danger for simulations is that specialized algorithms may be unintentionally non-ergodic by blocking the access to specific states [Landau'00]. Besides that, in the process of relaxation towards the equilibrium condition, some systems may be "trapped" in local energy minima, not reaching the global minimum. In this case, relaxation leads the system not to equilibrium but to a metastable condition. An useful way to test whether an algorithm is ergodic or not is to perform several simulations with the same parameters, but starting from different initial conditions [Kotelyanskii'04]. If the model is ergodic, results obtained using different initial conditions should be the same.

2.1.5. Inhomogeneous Systems

Monte Carlo simulations are useful for the study of systems which contain surfaces or interfaces. In such cases, properties become position-dependent. Consider the hypothetical system previously described: a lattice with half of its sites occupied by molecules grouped in the form of a cluster that is in turn surrounded by vacant sites. The equilibrium state is to be found departing from such initial state and according to the transition probabilities given by the Metropolis test in Equation (2.11). If the temperature has a very high value approaching infinity, the exponential term will tend to unity regardless of the energy difference involved in the transitions and all attempted motions will be allowed. It is not difficult to imagine that such situation will produce in the end a monophasic system, whose properties do not depend on the position in space. A more complicated situation arises if the temperature is lowered. Below a given threshold known as the critical temperature, the system is then constituted by two phases separated by an interface: one of them rich in molecules and equivalent to the liquid phase, and other rich in vacancies and equivalent to the vapor phase. Some intermixing between molecules and vacancies still exists. In fact, a perfect separation between both is to be found only at temperatures tending to zero.

In principle, it is possible to build a phase diagram for such systems by plotting a certain property such as density or energy density in both phases as function

of temperature. However, the calculation of thermodynamic properties in the vicinity of the critical point by means of Monte Carlo simulations is a demanding task [Landau'00]. In the case of a first order phase transition, the specific heat at the critical temperature tends to infinity, meaning very large fluctuations in properties such as energy and density. To illustrate this effect, consider a subsystem comprising a few lattice sites. The density there can be considerably bigger than the density in the total system due to huge fluctuations. This subsystem will then become highly correlated to other subsystems which must have a density smaller than the total density in order not to violate the constraint of constant amount of material in the system. This gives rise to large spatial correlations. Local density inhomogeneities in the system are the reason why experimental systems at the critical point scatter light, a phenomenon known as *critical opalescence* [Berry'80]. As a last remark, in spite of all complications related to critical phenomena, this work will be mainly focused on systems securely distant from the critical point.

2.1.6. Dynamic Properties

Often one is interested not only in obtaining a static description of a system but also details about its time evolution, i.e. its dynamic behavior. Transport coefficients such as the diffusion coefficient [Crank'85, Carslaw'86] describe how a system responds in the time domain to a given perturbation. If the perturbation is small, the response depends linearly on the perturbation and is related to the corresponding transport coefficient. The response of a system to a small perturbation should not depend on whether this is a result of some external force or a random thermal fluctuation [Kotelyanskii'04]. In this sense, transport coefficients can be obtained from systems at thermodynamical equilibrium by taking their fluctuations into account. For that, the so called *time correlation functions* have central importance. The time correlation function of two time dependent quantities A and B is defined as:

$$C_{AB}(t) = \langle A(0)B(t) \rangle , \tag{2.12}$$

where the brackets indicate equilibrium averages over an ensemble of states. When A and B are the same function, C_{AA} is called the *autocorrelation function* of A. The diffusion coefficient D, for instance, is related to the velocity autocorrelation function:

$$D = \frac{1}{3}\int_0^\infty dt \left\langle \mathrm{v}_i(0) \cdot \mathrm{v}_i(t) \right\rangle , \tag{2.13}$$

where $\mathbf{v}_i$ is the center of mass velocity of a single molecule labeled by index i. Now let the dynamics of the particles be considered in more detail. In classical statistical mechanics, the time evolution of many-body systems is governed by Newton's equation of motion:

$$m_i \frac{d}{dt}\left(\frac{d\mathbf{r}_i}{dt} \right) = \nabla_i U , \tag{2.14}$$

where m_i and $\mathbf{r}_i$ represent, respectively, the mass and coordinates of single particles and U the total potential energy in the system, which may comprise both external and intermolecular contributions. Trajectories through phase space are deterministic in contrast with the probabilistic trajectories generated in stochastic simulations, whose evolution in time is best described by Equation (2.08). A stochastic approach is well suited only to problems in which one is not aiming at a detailed atomistic description dealing with coordinates and momenta. In such problems, it is enough to consider a coarse-grained picture of the system, with only part of its degrees of freedom being explicitly pictured [Landau'00]. For the case of the diffusion coefficient expressed in Equation (2.13), an alternative expression derived by Einstein can be used [Kotelyanskii'04]. It disregards the velocities and considers just positions in space:

$$D = \lim_{t\to\infty} \frac{1}{6t} \left\langle \left| \mathbf{r}_i(t) - \mathbf{r}_i(0) \right|^2 \right\rangle . \tag{2.15}$$

As an illustration, consider the example of the interdiffusion in solid binary alloys. For the sake of simplicity, interactions between molecules will be considered the same regardless of their identity. In a real solid, molecules vibrate in their lattice sites and eventually hop to a neighboring vacant position. The time between molecular hoppings can be orders of magnitude higher than the time scale of vibrations. An explicit simulation of vibrations and hopping by means of the integration of Newton's equations would be computationally very demanding.

Furthermore, the essence of the interdiffusion problem stays in the hopping motions and this can be well described by a stochastic approach. The Metropolis test must take into account the activation energy necessary to move one molecule to a position where a defect or vacancy is present. Although this approach simplifies the problem, it has a disadvantage in the sense that this activation energy and consequently the jump rates which will determine the diffusion coefficient are given as input rather than output parameters [Landau'00]. Moreover, the notion of time in a Markov process does not contain specifications about the units of time [Landau'00].

Finally, aspects related to the dynamical behavior of the system should be kept in mind even when one is purely interested in static properties. The reason is that dynamics may influence the static properties obtained from simulations. Near to the critical point, for instance, spatial correlations are large and relaxation phenomena involve large length and time scales. This phenomenon, known as *critical slowing down*, turns the calculation of equilibrium properties near a critical point into a very demanding task [Landau'00]. Besides that, complications also arise when long time scales associated with metastability prevent the system from reaching its equilibrium configuration.

2.1.7. System Boundaries and Finite Size Effects

Monte Carlo simulations are performed with lattice systems with finite size, which naturally contain 'edges' or boundaries. The elimination of such edges is a crucial procedure if one wants to relate the properties obtained from simulations to those of real and almost infinitely large macroscopic systems. One way to accomplish this is to implement periodic boundaries in the system. Consider for simplicity a two-dimensional square lattice as depicted in Figure (2.01). If a particle attempts to move across one of its boundaries, it will appear in the opposite one, as if the system was bounded from all sides by replicas of its own. In spite of that, finite size effects can never be completely eliminated because the system is still characterized by a finite length L, which limits the maximum correlation length to $L/2$ [Landau'00]. Consequently, the properties obtained from simulations may differ from those of an infinitely large system even if periodic boundaries are implemented. Consider a two-phase system constituted by a suspended liquid film in equilibrium with its vapor. The interface of liquid films exhibits surface fluctuations known as capillary waves. In an infinitely large film, surface fluctuations have contribution of a broad spectrum of

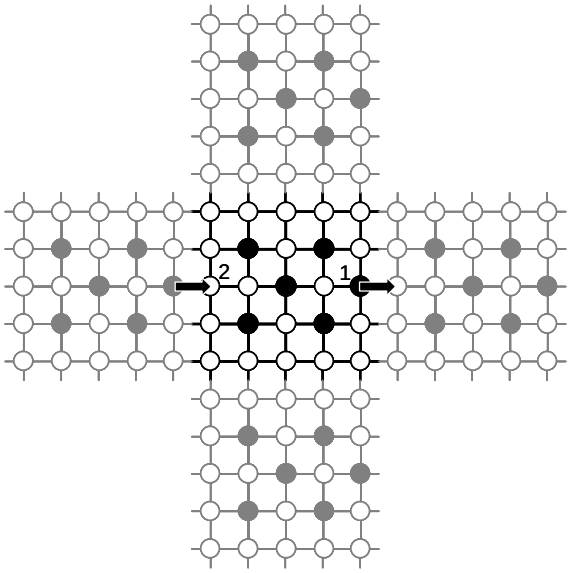

Figure 2.01 Two-dimensional square lattice (in black) surrounded by its replicas (in gray). Full circles represent molecules and open circles represent empty lattice sites. Under periodic boundary conditions, the molecule at position 1 crosses the boundaries of the original system and appears at position 2.

wavelengths. However, by confining the surface in a finite system, there is a restriction in the allowed values of wavelength so that the surface waves obey a continuity criterion (remember that the system is periodic). In this case, properties obtained by simulation may become closer to the experimental behavior if the system is made bigger, with the disadvantage that the time necessary for computations will increase. Finite size effects may become even more dramatic close to a critical point due to the large spatial correlations. Besides that, another aspect that must be taken into account when implementing periodic boundaries is the range of intermolecular interactions. In simulations involving long-range interactions, particles may interact with their periodic image, giving rise to nonrealistic results.

2.1.8. Errors and Limitations

Monte Carlo simulations depend very much on the performance of the computational resources available. Computer time and memory are key factors. There are also truncation and round-off errors related to the precision with which the computer executes numerical operations. In addition to that, systematic errors may rise from the process of generation of random numbers. An ideal generator must

provide uniformly distributed and uncorrelated random numbers, but there is no such perfect algorithm available [Landau'00].

Another source of error that deserves special attention is related to relaxation effects. Before starting the sampling of thermodynamical properties, enough time should be provided for the relaxation from the initial state to equilibrium. Unreliable values will be obtained if sampling starts before equilibrium is reached or if equilibrium cannot be reached at all due to non-ergodicity of the algorithm. The situation becomes more complicated as the system approaches a critical point because relaxation times increase dramatically.

Finally, it is necessary to point out that there is a standard deviation associated with the statistical sampling itself when a finite number of states is sampled, as expressed by Equation (2.06). The statistical sampling must collect series of states separated from each other by a certain time interval, so that they can be considered uncorrelated in time. If this is not done, the value of standard deviation will be underestimated. The reason is that the method of importance sampling leads to dynamic correlations between subsequently generated states. Therefore, for reliable statistics, it is essential to know the relaxation time associated with the thermodynamic quantity being considered.

2.2 Simulation of Polymer Chains

2.2.1. Fundamental Aspects of Polymer Physics

Polymers exist in a large variety of molecular architectures such as linear chains, rings, helices, stars and networks. Even the simplest example of a polymer chain may become very complex if the chemical structure is considered in all details. However, depending on the problem, the relevant physics may be satisfactorily captured by disregarding these details and picturing the polymer as a collection of elements connected to each other by fixed-length bonds. The configuration of the polymer corresponds to a random walk and structural parameters can be easily obtained by means of the appropriate statistics [Doi'86, Doi'96, Kotelyanskii'04]. The so called *end-to-end vector* joining one end of the chain to the other is a good indicator of the macromolecular size. If the polymer is made up of N bonds, being $\mathbf{r}_n$ the vector of the nth bond, the mean square end-to-end distance is given by:

$$\left\langle R^2 \right\rangle = \sum_{n=1}^{N}\sum_{m=1}^{N}\left\langle \mathbf{r}_n \cdot \mathbf{r}_m \right\rangle . \tag{2.16}$$

For chains following the statistics of a random walk, there is no correlation between different bond vectors. Hence, the summation over all terms in which $n \neq m$ equals zero and Equation (2.16) is reduced to:

$$\left\langle R^2 \right\rangle = \sum_{n=1}^{N}\left\langle \mathbf{r}_n^2 \right\rangle = Nb^2 , \tag{2.17}$$

where b represents the length of a coarse-grained segment. Equation (2.17) predicts that the size of the polymer is proportional to $N^{1/2}$ (or, using a quantity which is experimentally more accessible, to the square root of the molecular weight). In an ensemble of chains with the same structural parameters N and b, it can be shown in analogy to the problem of random walk that the distribution of end-to-end distances is Gaussian [Tanford'61]:

$$P(R) = \left(\frac{3}{2p\left\langle R^2 \right\rangle} \right)^{3/2} \mathrm{e}^{-\left(\frac{3}{2}\frac{R^2}{\left\langle R^2 \right\rangle} \right)}. \tag{2.18}$$

If an orientation correlation exists between subsequent segments, the equations above still hold but the parameter b must be substituted by an effective length b_{eff} which represents the length of the shortest statistically independent segment, the so called *Kuhn length*. Since the angles between real chemical bonds usually have fixed values, a statistically independent segment in a real polymer chain may comprise several single bonds. Another import structural quantity to describe polymer chains is the so called *radius of gyration*, which is defined as the average distance of the segments in the chain to its center of mass or alternatively as the average distance between two segments:

$$\left\langle R_g^2 \right\rangle = \frac{1}{N}\sum_{n=1}^{N}\left\langle \left(\mathbf{R}_n - \mathbf{R}_{\mathrm{CM}}\right)^2 \right\rangle = \frac{1}{2N^2}\sum_{n=1}^{N}\sum_{m=1}^{N}\left\langle \left(\mathbf{R}_n - \mathbf{R}_m\right)^2 \right\rangle, \tag{2.19}$$

where $\mathbf{R}_n$ is the position vector of the nth segment or of the chain center of mass in the case of $\mathbf{R}_{CM}$. Equation (2.19) can be further developed by recalling that the distance between two segments in a Gaussian chain is given by:

$$\left\langle \left(\mathbf{R}_n - \mathbf{R}_m\right)^2 \right\rangle = |n-m|b^2 . \tag{2.20}$$

By substituting Equation (2.20) in (2.19) and approximating the double summation by a double integral, the following relation is obtained:

$$\left\langle R_g^2 \right\rangle = \frac{1}{6} Nb^2 = \frac{1}{6}\left\langle R^2 \right\rangle . \tag{2.21}$$

In the considerations developed so far, long-range interactions such as van der Waals attraction between different segments and volume exclusion effects were not taken into account. Polymer chains pictured by such simplified model are called *ideal chains* and correspond to a random walk in which chain segments can intersect each other and occupy the same position in space. Such chains obviously do not respect the condition of volume exclusion. In this sense, the representation of a polymer chain as a self-avoiding random walk would be much closer to reality. By adding the restriction that no overlapping is permitted, the size distribution is shifted to larger values and the scaling laws derived for ideal chains are no longer valid. Numerical simulations of large chains under volume exclusion have shown for instance that $\left\langle R_g \right\rangle \propto N^{0.588}$ [Doi'96]. If a polymer chain is surrounded by a solvent, the situation becomes even more complex. The probability of each chain conformation will depend also on the sum of different van der Waals interactions, namely: 1) attractive forces between two nonbonded polymer segments; 2) attraction between a polymer segment and a solvent molecule; 3) attraction between two different solvent molecules. It is expected that the average conformation will depend on the affinity between polymer and solvent. A low degree of affinity generates chains which are shrunken and compact. By the other side, chains acquire a more extended conformation as the affinity increases. However, if affinity exists but the temperature is reduced, polymer chains will not have enough thermal energy to explore extended conformations and

the attraction forces between polymer segments will start to dominate and induce shrinkage of the chain. At a given temperature, called the Θ temperature, the tendency to shrink induced by van der Waals forces may balance the tendency to expand due to volume exclusion. In this case, the polymer behaves as an ideal chain and respects the correspondent scaling laws. The statistics of ideal chains holds not only for polymer solutions at the Θ temperature but also for polymer melts. The reason is that a polymer segment is unable to distinguish between segments from its own chain and those from other chains, since the overlap is essentially total in a melt. Hence, the chain has no reason to assume one configuration in preference to another driven by interactions with distant elements within the same molecule [Bueche'62].

If one is interested in the dynamics of polymer chains, the so called *Rouse model* provides an effective description for low molecular weight chains in a melt [Doi'86, Doi'96, Kotelyanskii'04]. This model represents a polymer chain as a set of beads connected by harmonic springs. These beads move as Brownian particles subject to random forces, to the harmonic potential related to the springs and to friction forces from the environment. The time dependent behavior of the position vectors of each of the *n*th chain segments is then given by the following master equation:

$$\frac{\partial}{\partial t}\mathbf{R}(n,t) = \frac{k}{z}\frac{\partial^2}{\partial n^2}\mathbf{R}(n,t) + \mathbf{g}(n,t), \tag{2.22}$$

where k and z represent respectively the spring and friction constants and $\mathbf{g}(n,t)$ is a distribution function accounting for the random fluctuations. For an ideal and linear polymer chain following Gaussian statistics, the Rouse model predicts that the longest relaxation time is proportional to N^2. This corresponds to the time needed for the chain center of mass to diffuse by a length commensurate to the radius of gyration. It is also approximately equal to the time needed for the end-to-end vector to loose memory of its initial orientation. As the molecular weight increases, entanglement constraints arise between different polymer chains, making relaxation slower than predicted by the Rouse model. The *reptation model* takes this into account by assuming that a chain undergoes Rouse-like motion inside a hypothetical tube whose diameter and shape are determined by the obstacles in the polymer network.

2.2.2. Monte Carlo Simulations of Polymer Chains on a Lattice

One of the simplest ways of simulating chain conformations is to build a random walk which is made up of constant length segments connecting nearest neighbor sites on a lattice. These sites and segments do not represent necessarily individual atoms and molecular bonds but are rather the building blocks for a coarse-grained model [Binder'04]. For long enough chains, the values of the end-to-end vector of different conformations follow a Gaussian distribution. The effect of volume exclusion is obviously not taken into account in a simple random walk. Therefore, more realistical models are based on self-avoiding random walks. In this case, the computer generates a large sample of random walks and rejects conformations in which the chain crosses itself. This procedure follows the principle that all conformations that obey the excluded volume condition must have equal *a priori* probability. The problem is that, as chains become larger, the probability of crossings between segments increases in such a way that the high number of rejections makes the simulation slow. A possible solution would be an algorithm that avoids choosing bond directions which will lead to these crossings. However, each conformation would need to be reweighted to fulfill the principle of equal *a priori* probabilities. The problem becomes even more complicated for multichain systems.

Methods using the concepts exposed so far are based on the generation of different conformations by means of chain growth. They are considered as static because they do not address how a given conformation evolves in time to generate other conformations. Another class of algorithms is dynamic in nature and allows random moves of parts of the polymer chain [Binder'04]. Subsequent configurations are generated from the previous one as in a stochastic Markov process. This is achieved by randomly selecting one of the possible rearrangements the chain may undergo and new lattice sites to which chain elements should be shifted. Figure (2.02) brings three examples of dynamic Monte Carlo algorithms for self-avoiding random walks. In the Verdier-Stockmayer algorithm, single sites may be moved obeying the restriction that no bond length changes. In the "slithering snake" method, a bond is removed from one end and then attached to the other end of the polymer in a randomly chosen orientation. In the pivot method, a large part of the chain is rotated about a single site of the chain. Clearly, the lattice must contain a minimum number of empty sites so that rearrangements can occur. Movements that violate the excluded

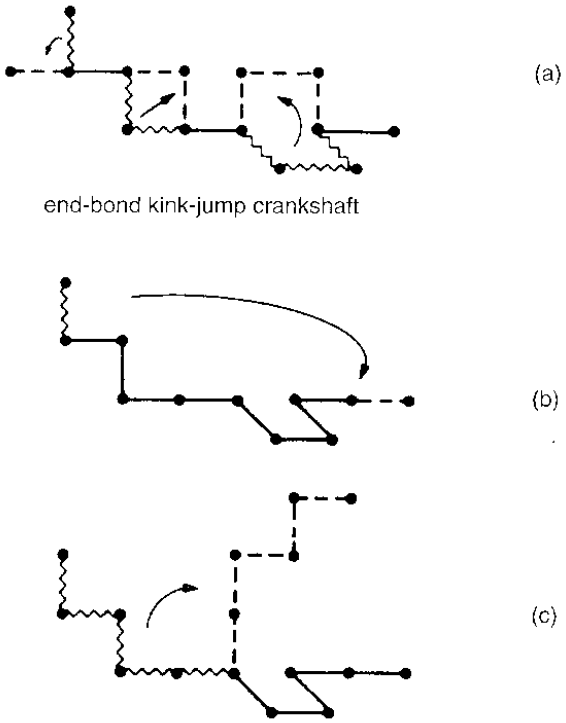

Figure 2.2 Examples of dynamic Monte Carlo algorithms for self-avoiding walks: bonds indicated as wavy lines are moved to new positions (broken lines), other bonds (full lines) are not moved. (a) Verdier-Stockmayer algorithm on the simple cubic lattice showing three types of motion: end-bond motion, kink-jump motion, crankshaft motion. (b) "Slithering snake"algorithm. (c) Pivot algorithm [Binder'04].

volume condition should be rejected and the actual configuration counted once more in the averagement. An ensemble of polymer chains may be simulated under athermal conditions, meaning that rearrangements have no constraints except for the chain connectivity and the volume exclusion. However, if the problem involves also an interaction energy depending on the chain configuration, a Metropolis test must be implemented as an additional condition for allowing or rejecting a given rearrangement. The equilibrium configuration is calculated by sampling a large number of states after the system has been given enough time to relax from its arbitrary initial state. In addition to the rigid bond models previously described, models allowing slight variations in the bond length have been proposed. One example is the bond fluctuation model [Landau'00, Binder'04]. In this approach, a monomer occupies a nearest neighbor plaquette and attempts to move randomly by an

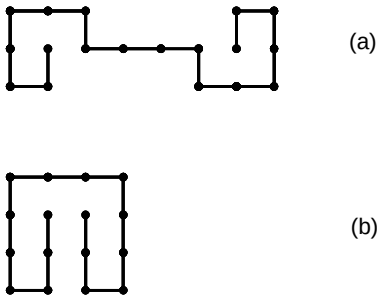

Figure 2.03 Examples of self-avoiding random walks on the square lattice that cannot move if (a) the "slithering snake" algorithm is used or (b) if a combination of the "slithering snake" and the Verdier-Stockmayer algorithm is used [Binder'04].

amount which does not stretch or compress the bonds to its neighbors too much. The excluded volume constraint is obeyed by not allowing overlap of monomer plaquettes.

Algorithms such as the Verdier-Stockmayer and the bond fluctuation are compatible with the Rouse and reptation models in the sense that they simulate local stochastic changes of the configuration of a chain. In spite of that, the Verdier-Stockmayer algorithm is not fully ergodic, a feature also observed in the "slithering snake". In these models, there are configurations which cannot relax at all, as shown in Figure (2.03). This also means that such configurations cannot be reached from other configurations and represent regions of the phase space completely left out from the sampling, leading to a small systematic error [Binder'04]. The pivot algorithm exhibits better ergodicity properties and is well suited to the calculation of static properties. However, relaxation phenomena in this model are fast and not representative of real dynamics. Usually, the time unit in polymer simulations is chosen to correspond to an average of one Monte Carlo step per monomer. In the pivot, however, not all steps reflect real, physical time development since a single rearrangement may involve a large number of elements [Binder'04]. Moreover, this model can be used only in simulations of low density polymer systems [Binder'04].

In fact, for all algorithms discussed here, the acceptance rate of all moves decreases strongly with increasing density of occupied lattice sites. Rearrangements become then very slow at high densities and impossible in a fully occupied lattice. An alternative and efficient model called the *cooperative motion algorithm* (CMA) [Pakula'04] has been proposed by Pakula for the simulation of dense polymer melts in

a fully occupied lattice. In the next section we proceed to a brief description of this method, which is the basis of the work presented here.

2.3 The Cooperative Motion Algorithm

The simulation methods previously described can operate only in systems with a relatively high fraction of lattice sites left free. They correspond to a picture of the liquid phase in which a molecule (or a molecular segment in the case of polymers) needs a free space in its neighborhood in order to make a translational step. However, a different microscopic mechanism has been proposed for the molecular motion in high density liquids such as polymer melts. According to this mechanism, on the short time scale, molecules oscillate around some quasi-fixed positions, being temporarily "caged" by neighbors. More extensive translational motions of molecules take place on a much longer time scale due to the breaking down of cages by cooperative processes [Pakula'04]. Trajectories of molecules consist, therefore, both of oscillatory components and of occasional longer range translational movements between subsequent quasi-fixed states, as illustrated in Figure (2.04). The cooperative motion

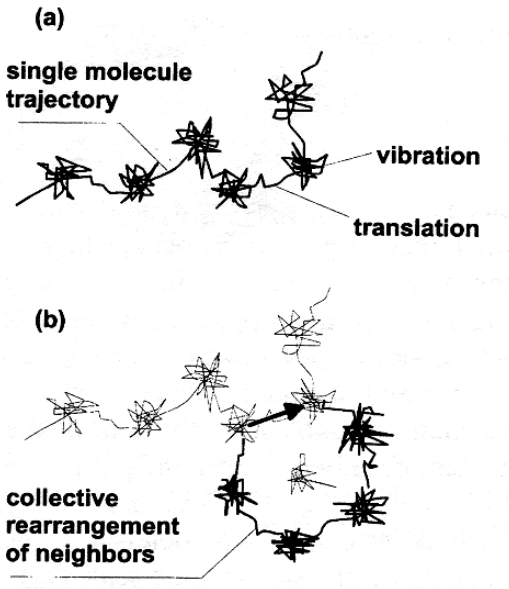

Figure 2.04 Molecular trajectories in a liquid. (a) Single molecule trajectory consisting of vibrations around quasi-fixed positions and occasional translation steps. (b) Cooperative translational motion of several molecules [Pakula'04].

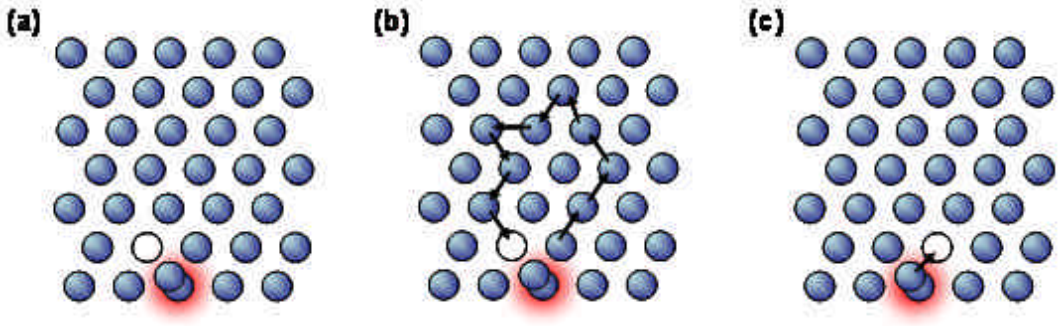

Figure 2.05 An example of a simple rearrangement loop performed by the CMA on a schematic two-dimensional lattice of nonbonded beads (in blue). (a) First, a temporary defect or vacancy is created at a randomly chosen position (empty circle), together with a hypothetical double occupancy (red area). (b) The defect exchanges position with randomly chosen neighbors along a random loop. (c) Finally, the defect is annihilated.

algorithm (CMA), differently from other methods described before, is able to simulate the cooperative rearrangements of polymer systems in fully occupied lattices [Pakula'04].

In the CMA, the positions of the molecules are regarded as coinciding with the lattice sites. Usually, a face-centered cubic (fcc) lattice is adopted. It is considered only as a coordination skeleton defining the presence of nearest neighbors but not precisely the distances between them [Pakula'04]. Although all sites are occupied, it is assumed that the system has some excess volume so that molecules have enough space to vibrate around their positions defined by lattice sites but can hardly move over larger distances because all neighboring sites are occupied. Vibrations are related to a short time scale and are not explicitly simulated. However, they are considered as the cause for the attempts performed by the simulation program to move a molecule to a random neighboring site. In a fully occupied lattice, these motions are possible only in a collective way [Pakula'04]. Performing rearrangements by means of collective motions keeps the system continuous and satisfies the excluded volume condition. This is achieved in the program by choosing a random position in the lattice and creating a temporary defect on it, as depicted in Figure (2.05). One of the nearest neighbors is randomly chosen and changes its position with the defect. The procedure is repeated in such a way that the defect performs a random walk or loop through the lattice exchanging positions of several elements. When the loop is closed, the defect is annihilated. It is also important to point out that no thermodynamic quantity is

calculated while the defect is still present in the lattice. The process of creating a defect and performing its random walk through a loop is repeated several times. Other possibilities such as non-reversal random walk and self-avoiding walk may be explored as well [Pakula'04]. In more complex systems representing polymers, only rearrangements that do not break bonds and do not change sequences of elements along individual chains are accepted. The most straightforward choice of an initial state is an ordered array of chains parallel to each other. When simulation starts, chains rearrange only by displacements involving conformational changes. As a result of the large number of such rearrangements, elements of the system move along random walk trajectories. Illustrated in Figure (2.06) there are two possibilities to move parts of a chain. In the first, the path of the defect crosses the chain contour and causes rotation of bonds. In the second, the defect enters the chain contour and leaves after a short walk along it. In this case, in each step of the motion of the defect, one and only one bond is attempted to be extended but this extension is immediately relaxed by motion of other elements along the chain until the defect finds the appropriate position to leave the chain contour [Pakula'04]. The CMA is a versatile method in the sense that chain fragments are allowed to move both along the chain contour or transversally to it. This probably improves the ergodicity properties.

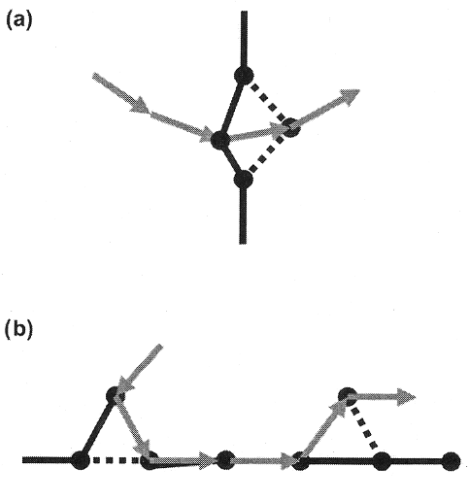

Figure 2.06 Types of rearrangements in a system of polymer chains: (a) the path of the defect (gray arrows) crosses the chain contour and causes rotation of bonds; (b) the defect enters the chain contour and leaves after a short walk along it. Dashed and full lines represent the chain conformation before and after rearrangement, respectively [Pakula'04].

Static properties obtained from the simulation of polymer melts using CMA are consistent. For melts of linear chains, the distribution of chain conformations is Gaussian and the characteristic scaling laws for end-to-end distance and radius of gyration are obeyed [Pakula'91, Gauger'93, Pakula'04]. By implementing interaction energies, heterogeneous systems can be simulated as well. In fact the model has been successfully applied in the study of microphase separation in diblock copolymers [Pakula'04]. In this case, two types of incompatible monomers (A and B) are considered. It is often assumed that the energy of mixing is given only by a repulsive interaction between monomers of different types. The interaction parameters e are given by $e_{AA} = e_{BB} = 0$ and $e_{AB} > 0$. The probability P of a given molecular motion is calculated considering only the energy E_{final} that the element will have in its new position summing up all the nearest neighbor interactions:

$$P = \mathrm{e}^{-E_{final}/kT}. \tag{2.23}$$

By means of a simple analysis in analogy to the one developed for the Metropolis test in Section (2.1.3), it is possible to show that this method respects the principle of detailed balance of energy.

Dynamical properties have been studied as well by means of time correlations similar to those exposed in Section (2.1.6). As in other Monte Carlo methods, the time step in CMA usually corresponds to the number of attempts necessary to perform cooperative rearrangements resulting on average in one attempt per system element. Results show that the dynamic behavior of simulated chains corresponds well to the experimental behavior. In simulations, the diffusion constants for long chains reach the well known scaling dependence $D \propto N^{-2}$ and the chain relaxation times t reach the scaling law $t \propto N^{w}$, with $w > 3$, as observed in chain length dependencies of melt viscosities for long chains [Pakula'04]. More detailed analysis of the static and dynamic behavior of CMA has already been presented [Pakula'00a, Pakula'04], but problems related to the dynamics and the mechanism of motion of polymer chains still remain not completely understood.

The CMA is efficient and easy to implement. In practical terms, one needs two computer programs: one to generate an initial configuration of the system being studied and a second for the relaxation of such initial configuration to the equilibrium

condition. As soon as equilibrium is reached, the same program is used for calculating thermodynamic averages. In the present work, *Pascal* was adopted as the programming language, although it is not the only alternative. Programs following the method of CMA are very compact regarding memory requirements and can be performed in a common personal computer. Most of the simulations performed here could be accomplished within less than 24 hours of computation time each. For a more detailed description of the algorithm, we refer the reader to a previous publication of Pakula [Pakula'04].

3

Implementing Geometrical Confinement in Simulations

3.1 Confined Systems

Physical, chemical and biological processes taking place in confined geometries are widespread in nature. For instance, electron microscopic evidence suggests that the fluid phase of the cytoplasm is largely distributed in pores, interstices and channels between fibrous structures [Minton'92]. In materials science, examples of chemical nanoreactors are lipid vesicles, porous silica, carbon nanotubes and lamellar materials. Advances in the field of nanotechnology motivate the understanding of basic aspects of physics and chemistry under confinement and in low dimensions.

With the appropriate choice of system size and boundary conditions, it is possible to simulate confined systems with several geometries and dimensionalities. Consider a three-dimensional system in the shape of a cube and constituted by a fcc lattice. By implementing periodic boundary condition in all directions, processes simulated in this system will be equivalent to real processes happening in the bulk, provided that finite size effects such as those discussed in Section (2.1.7) are negligible. If two parallel faces of the cubic system are chosen and the boundaries made non-periodic, the system corresponds to a thin film or a lamella that is bounded by a pair of parallel hard walls in one direction, but is infinite in all other orthogonal directions. In this case, the thickness is expressed by means of the lattice unit length, which is related to molecular sizes and intermolecular distances. Due to

computational limitations, the system size cannot exceed the range of nanometers. If two pairs of boundaries are left non-periodic, then the system corresponds to an infinitely long nanotube or pore. All faces of the cube can be made non-periodic to account for confinement in all directions. For this situation, however, it would be much more interesting to have spherical-shaped systems. They correspond to geometrical confinement as it is achieved experimentally by performing reactions inside vesicles or emulsified droplets. The geometry of the simulated system can be also chosen to correspond to the more complex case of a droplet sitting on a surface. However, if systems are implemented this way, their boundaries are hard and have a fixed shape, different from the experimental reality where the interfaces of a droplet are soft, mobile and able to rearrange depending on the processes happening inside. For this reason, part of this work was dedicated to develop a reliable algorithm to simulate the liquid-vapor equilibrium in a droplet with soft boundaries. Nanometer-sized droplets generated this way have molecular resolution, and the droplet shape can change as function of interaction parameters, temperature, chemical composition and surface inhomogeneities. The next section is dedicated to the application of the CMA in the simulation of liquid droplets sitting at solid surfaces [Cordeiro'05]. We shall demonstrate that the simulated droplets reproduce satisfactorily the behavior of real droplets. Although the size of simulated droplets is on the order of nanometers, results can be extended to micrometer-sized droplets. Later, the same method will be applied to investigate polymerization reactions taking place inside small droplets (see Chapter 4) and also the phenomenon of microwell and ringlike deposit formation when a droplet evaporates on the surface of a soluble substrate, especially the case of thin polymer films (see Chapter 6).

3.2 Simulation of Small Liquid Droplets at Surfaces

For the simulation of droplets at surfaces using the CMA [Cordeiro'05], elements on the lattice are regarded as having three types of identity. They are labeled to represent either solvent particles (SO), substrate particles (SU), or vacuum (VA). Although elements can exchange place with each other, their identity is conserved. The repulsive energy of interaction between two neighboring beads is considered as zero if they have the same identity and as a finite and positive number if they have

different identity. Before each movement, the probability of acceptance of a bead in the next position is calculated according to the Boltzmann factor in Equation (2.23). The energy of interaction E_i of the moving bead with neighbors in the next position is given by:

$$E_i = n_{ij} e_{ij} + n_{ik} e_{ik}, \tag{3.01}$$

where e represents the interaction energy between two beads and n the number of interactions. The different subscripts indicate that only interactions between beads with different identity contribute to the total energy. Both E_i and kT are considered in arbitrary units. After an appropriate relaxation time, the final system can be regarded as being in equilibrium at a chosen temperature that is given in units of kT. The consequence of all these assumptions is that during the system equilibration, beads of the same identity tend to aggregate since the intermixing of phases costs energy. As will be shown, solvent beads tend to aggregate in a spherical-shaped phase to minimize their contact with vacuum, i.e., they form a droplet. Simulations of droplets on surfaces, free standing droplets and liquid films on surfaces were performed. Although our main interest was in droplets on surfaces, the other situations were important to show that the surface tension of the solvent in equilibrium with its vapor is the same in all the cases, as one would expect in reality. In the simulations of droplets on surfaces, the initial system configuration was a cubic droplet of pure solvent placed upon a layer of substrate material and surrounded by vacuum. The simulation then started and proceeded until the cubic droplet had relaxed to a droplet with the shape of a spherical cap. During the relaxation of the cubic droplet, the motion of substrate beads was forbidden to avoid their intermixing with solvent or vacuum. However, substrate beads on the surface could still interact with solvent or vacuum and the energies of interaction determined the substrate wettability. Periodic boundary conditions were applied only in the directions parallel to the substrate surface. A similar initial configuration was used in the simulations of free standing droplets with the difference that the substrate was absent and all the boundaries were periodic. In the case of liquid films on a substrate, the initial system configuration was a layer of pure solvent between substrate and vacuum. As the simulation started, solvent and vacuum started to intermix. Simulations were carried out for systems with

TABLE 3.01: Average Quantities Obtained from Simulations (Error in the Last Digit)[a]

kT	system feature[b]	size[c]	solvent amount	r_l	r_v	x_l	x_v	R_e	D
2.0	drop on surface	9.6×10^4	1.35×10^4	0.998	0.0017	0.014	0.020	29.0	3.37
2.8	drop on surface	9.6×10^4	1.35×10^4	0.990	0.0117	0.1192	0.0365	29.4	4.23
3.0	drop on surface	9.6×10^4	1.35×10^4	0.9856	0.0163	0.168	0.1896	29.07	3.47
3.0	drop on surface	2.5×10^5	1.35×10^4	0.9857	0.01619	0.166	0.188	26.2	3.75
3.0	free drop	2.5×10^5	1.35×10^4	0.9864	0.0184	0.157	0.213	15.8	3.18
3.0	free drop	2.5×10^5	7.2×10^3	0.9876	0.0187	0.142	0.217	12	2.44
3.0	film	2.5×10^5	7.5×10^4	0.9845	0.0156	0.1811	0.182	—	2.78
3.5	drop on surface	2.5×10^5	1.35×10^4	0.9712	0.0333	0.324	0.3767	23.5	6.01
4.0	drop on surface	9.6×10^4	1.35×10^4	0.945	0.0589	0.593	0.635	29.74	6.71
4.0	free drop	6.25×10^4	1.35×10^4	0.947	0.0634	0.572	0.678	16	6.22
4.0	film	9.6×10^4	4.8×10^4	0.9432	0.0568	0.618	0.617	—	3.99
4.3	drop on surface	9.6×10^4	1.35×10^4	0.922	0.0805	0.781	0.8367	30.97	7.5
5.0	film	9.6×10^4	4.8×10^4	0.841	0.157	1.442	1.42	—	7.34

[a] Listed parameters are density (r) and energy density (x) for the liquid (l) and vapor (v) phases, as well as droplet equimolar radius (R_e) and interface thickness (D). See details in the text.

[b] In all cases, the interaction energies SO–VA, SO–SU and SU–VA were 1, 0.5 and 1, respectively.

[c] The system size is regarded as the sum of solvent and vacuum elements. Substrate elements are not counted because their motion is forbidden.

different sizes, as shown in Table (3.01). The total number of beads in each system was on the order of 10^5. It is observed that the system size and the proportion between its components do not influence the thermodynamic properties of the droplets, as one would expect for real droplets. However, the appropriate choice of system size plays still a crucial role [Thompson'84]. If the system volume is very large compared with the initial amount of liquid, the solvent will evaporate at temperatures considerably lower than the critical temperature, and no droplet will be formed. In such a system, the solvent and vacuum beads are completely intermixed. Analogously, if the initial amount of solvent is too high, the liquid phase can spread until it reaches the periodic boundaries. In this case, a solvent film will be formed instead of a droplet.

As the simulation starts, each movement attempt is considered as a Monte Carlo step, regardless of the identity of the moving bead or whether the attempted motion is successful or not. A unit of time is assumed to correspond to a number of attempts equal to the number of elements in the system. During one unit of time, the system performs on average one motion attempt per element. To evaluate the time

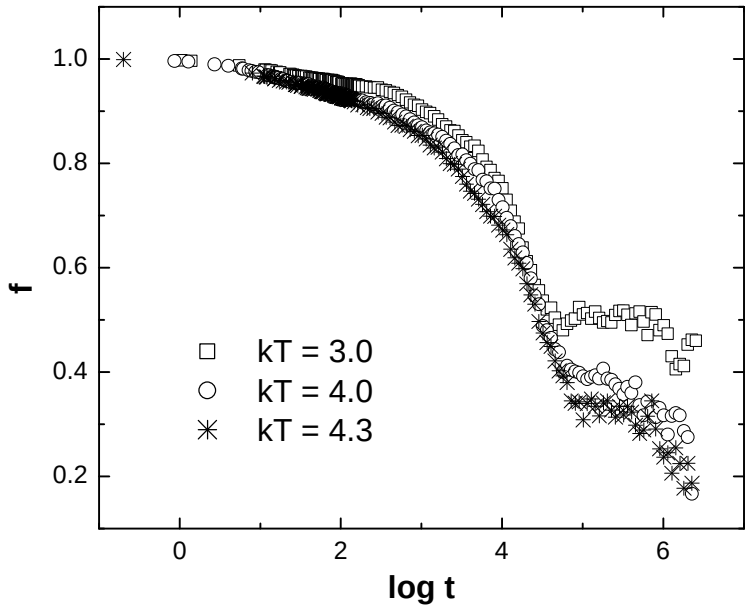

Figure 3.01 Shape correlation function for droplets on a surface at several temperatures. The interaction energies SO–VA, SO–SU and SU–VA were 1, 0.5 and 1, respectively.

necessary to drive the systems to the equilibrium condition, we defined a so called "shape correlation function" *f* given by:

$$f = \frac{1}{N_s}\sum_i a_i(0)\cdot a_i(t), \tag{3.02}$$

where N_s is the total number of solvent beads and $a_i(t)$ defines the occupation of each lattice site *i* at a time *t*. If the lattice site is occupied by a solvent bead, $a_i(t) = 1$, otherwise $a_i(t) = 0$. The shape correlation function measures which fraction of the sites that accommodated a solvent at $t = 0$ also accommodates a solvent at a time *t*. Figure (3.01) shows the typical behavior of *f* as function of simulation time. As the droplet relaxes from a cube to its equilibrium shape, *f* decreases from 1 to a finite value. The intermixing between solvent and vacuum also contributes to the decrease of *f*. In times on the order of 10^5, the correlation function reaches a plateau and the system can be considered to be fully relaxed. In all simulations, the systems were allowed to relax for a period at least 10 times longer than the time needed to reach the plateau. If droplets relax for very long times, they can also move in relation to their initial position. Because of that, a further decrease in *f* after the plateau can be

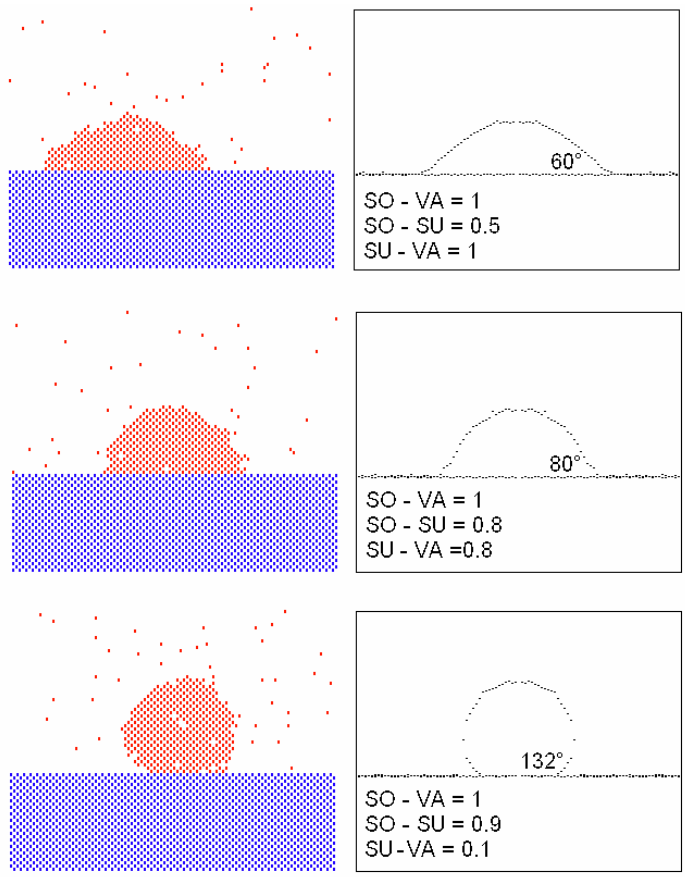

Figure 3.02 Different droplet shapes generated by varying the interaction energies between beads. Left pictures are snapshots of the system. Blue and red dots are substrate and solvent, respectively. Vacuum beads were not represented for simplicity. Right boxes are 360° radial averages of the corresponding snapshots. Points near the center of symmetry should be disregarded due to the small number of beads sampled in this region. The contact angles were obtained by fitting the shapes as spherical caps.

observed in some cases. Droplets were allowed to relax under various conditions. The influence of parameters such as temperature and interaction between elements was systematically studied. After the relaxation, sampling started for the thermodynamic averages every ~10^6 Monte Carlo steps. Average quantities such as the energy density (x) in the liquid and vapor phases were calculated. We also calculated the occupancy of each lattice site, i.e. the fraction of time it is occupied by a solvent bead. This allowed determination of the average shape of the droplets, their radius of curvature and their density profile across the interface. Generally, the time required to obtain smooth density profiles was equivalent to about 10 relaxation times. All simulations

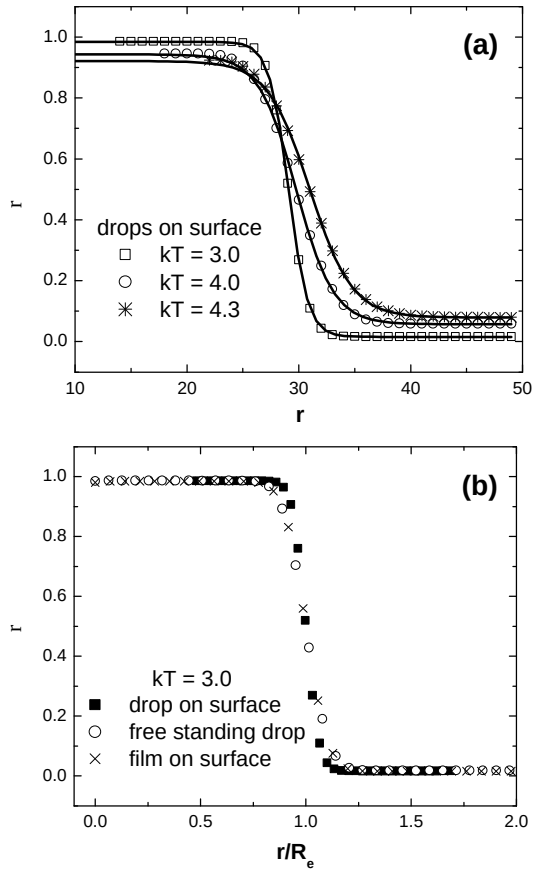

Figure 3.03 (a) Density as function of distance from the center of curvature for droplets on surface at different temperatures (full lines represent the tanh fitting). (b) Density as function of distance (normalized to the equimolar dividing surface), showing the behavior of drops on surface, free drops and films on surface.

were performed in common PCs. Due to the high efficiency of the method, big systems (~10^5 elements) could be simulated within hours.

The validity of the model can be tested by analyzing how the droplet shape depends on the interaction energies between beads. As stated earlier, solvent beads tend to form an aggregated phase to minimize their contact area with vacuum. If there is no substrate, the droplet will have the shape of a sphere. However, if a substrate is present, three kinds of repulsive interactions should be considered, namely SO–VA, SO–SU, and SU–VA. Figure (3.02) shows snapshots of droplets with different shapes. The SO–VA interaction was the same in all cases, but the other two were varied. If the repulsive interaction SO–SU is less than SU–VA, the solvent wets the substrate and the contact angle of the resulting droplet is lower than 90°. The opposite happens

if SO–SU is considered higher than SU–VA. In this case, the solvent hardly wets the substrate and the contact angle is higher than 90°. These features are in qualitative agreement with experiments. Another way to validate the model is to compare the thermodynamic properties of simulated droplets with those of real droplets. For that, quantities such as the densities of the liquid and vapor coexisting phases were calculated. Density was defined as fraction of solvent beads in a given region of the lattice. Figure (3.03) shows typical density profiles recorded for simulated droplets. The density (r) varies as function of the distance (r) from the center of curvature of the droplets. It is initially constant and corresponds to the liquid phase density (r_l). At a given distance, the density decreases to a lower plateau that corresponds to the density of the vapor (r_v). The transition between liquid and vapor is smooth and the density profile can be fitted by a tanh function [Thompson'84, Rowlinson'84]:

$$r(r) = \tfrac{1}{2}(r_l + r_v) - \tfrac{1}{2}(r_l - r_v)\tanh(2(r - R_e)/D), \qquad (3.03)$$

where r is the distance from the droplet center of curvature, R_e is the radius of the equimolar dividing surface and D is a parameter related to the interface thickness. The parameters related to the fitting procedure are listed in Table (3.01).

It is well known that, when bulk liquids are in equilibrium with their vapor, the following empirical relations hold for the density of the coexisting phases [Guggenheim'45, Guggenheim'85]:

$$\frac{r_v}{r_c} = 1 + \frac{3}{4}\left(1 - \frac{T}{T_c}\right) - \frac{7}{4}\left(1 - \frac{T}{T_c}\right)^{\frac{1}{3}}, \qquad (3.04)$$

$$\frac{r_l}{r_c} = 1 + \frac{3}{4}\left(1 - \frac{T}{T_c}\right) + \frac{7}{4}\left(1 - \frac{T}{T_c}\right)^{\frac{1}{3}}, \qquad (3.05)$$

$$\frac{r_l - r_v}{r_c} = \frac{7}{2}\left(1 - \frac{T}{T_c}\right)^{\frac{1}{3}}, \qquad (3.06)$$

$$\frac{r_l + r_v}{2r_c} = 1 + \frac{3}{4}\left(1 - \frac{T}{T_c}\right), \tag{3.07}$$

where r_c represents the density at the critical point. According to Equations (3.04) and (3.05), the density of the vapor increases as temperature increases, while the opposite happens with the density of the liquid. When the critical temperature is reached, the density of liquid and vapor are equal and the system becomes monophasic, i.e. the boundary between liquid and vapor disappears. To test whether simulations reproduce this effect or not, droplets were simulated at various temperatures and the densities of the coexisting phases were determined. Although temperature was varied, the interactions SO–VA, SO–SU, and SU–VA had fixed values of 1, 0.5 and 1, respectively. The liquid-vapor coexistence diagram constructed with the simulated densities is shown in Figure (3.04). Droplets generated at temperatures lower than 2.8 are not considered here because they are not spherically shaped. They exhibit flat surfaces like a crystal, and the system can be regarded as being a solid in equilibrium with vapor. Thus, the temperature of ~ 2.8 represents the triple point. Above this temperature, the densities of the coexisting phases follow qualitatively the behavior previously described. The results do not depend on system size. Moreover, droplets on surface, free standing droplets and liquid films on surface follow the same tendency. This is in accordance with experiment, since the density is an intrinsic property of the liquid, does not matter if it is a droplet or a film.

Figure (3.04) shows that, by considering r_c = 0.5, it is possible to fit the part of the coexistence curve corresponding to vapor with $kT_c = 5.33 \pm 0.06$. The fitting is not a very strict way for determining the critical temperature but suffices for a semi-quantitative analysis. The density of the liquid calculated by substituting these parameters in Equation (3.05), nevertheless, does not agree with the values of r_l obtained from simulations. Such disagreement is due to the fact that the simulation does not account for the thermal expansion of the liquid phase. This problem can be solved by correcting the liquid phase densities. According to the Eyring-Cremer model of liquids [Luck'91], the volume corresponding to thermal vibrations of molecules in the liquid increases as function of temperature, causing its density to decrease. In addition to that, "holes" or vacancies appear inside the liquid structure at

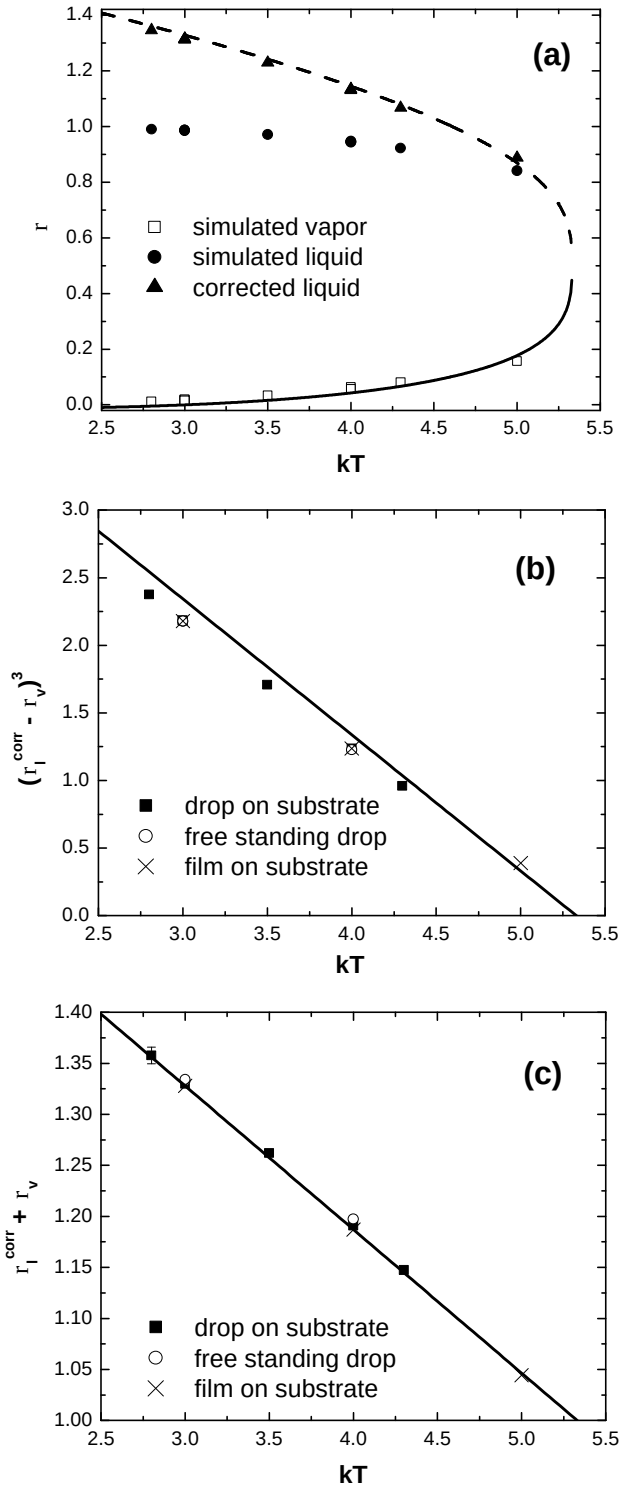

Figure 3.04 (a) Liquid-vapor coexistence diagram obtained from simulations. Simulated liquid densities (?) are corrected for thermal expansion (?) as described in the text. Full line represents the fitting of vapor density according to Equation (3.04), with the parameters r_c = 0.5 and kT_c = 5.33 ± 0.03. Dashed line is the empirical curve for liquid density constructed by substituting these parameters on Equation (3.05). (b,c) Comparison between simulated systems and empirical laws. Full lines were built by substituting the parameters above on Equations (3.06) and (3.07) in parts b and c, respectively. When not indicated, error bars are smaller than the size of the points.

temperatures closer to the critical point. Thus, the density of the liquid can be expressed as:

$$r_l = (r_l^0 - aT) - r_{holes}\,, \tag{3.08}$$

where r_l^0 is the liquid density at 0 K, a is its coefficient of thermal expansion and r_{holes} is the density (in this case molar fraction) of holes in the liquid. The term in brackets is related to the thermal expansion of the liquid and is not reproduced by simulation methods based on a rigid lattice structure of hard spheres, but it can be considered in the lattice models by means of additional assumptions [Pakula'00b]. In fact, the simulation method in the version described here accounts only for the second term r_{holes}, since some elements representing vacuum manage to penetrate the liquid phase and create vacancies. Therefore, the term in brackets is the key for the correction of the liquid phase densities obtained from simulation. Since the Eyring-Cremer model assumes that the concentration of holes in the liquid is equal to the concentration of molecules in the vapor phase, Equation (3.08) can be rewritten as:

$$r_l + r_v = (r_l^0 - aT)\,. \tag{3.09}$$

Through the use of Equation (3.07) to calculate the density of the liquid at 0 K, one finds that $r_l^0 = 7r_c/2$. Using this identity and substituting Equation (3.09) in (3.07), the coefficient of thermal expansion of the liquid can be expressed as:

$$a = \frac{3}{4T_c}\,. \tag{3.10}$$

We will choose the critical point as a reference and all other points will be corrected in relation to it. In this case, the expression for the corrected liquid density is given by:

$$r_l^{corr} = r_l - a(T - T_c)\,, \tag{3.11}$$

which finally becomes:

$$r_l^{corr} = r_l + \frac{3}{4}\left(1 - \frac{T}{T_c}\right). \qquad (3.12)$$

In fact, Figure (3.04) shows that a fairly good agreement is observed between Equation (3.05) and the simulated data after such correction. Through the use of the corrected values of the density of the liquid, a good agreement between data from simulation and Equations (3.06) and (3.07) is also observed in Figure (3.04).

The difference between the densities of coexisting phases can be converted to the surface tension of the droplets. According to literature [Guggenheim'45, Guggenheim'85], the temperature dependence of the surface tension of bulk liquids is given by the empirical equation:

$$\gamma = \gamma_0 (1 - T/T_c)^a , \qquad (3.13)$$

where γ is the surface tension, γ_0 is the surface tension at zero temperature and a is a constant close to $11/9$ for simple liquids. For instance, a value of 1.302 ± 0.006 for a was reported for liquid Xenon [Zollweg'71]. The ratio γ/γ_0 can be determined by the combination of Equations (3.06) and (3.13) and considering $a = 11/9$, and its temperature dependence is shown in Figure (3.05). In this work, the parameter γ/γ_0 was determined indirectly by means of the densities. Direct determination of the surface tension by means of arguments involving free energy of the system would be more complicated. In this case, one should count both enthalpic and entropic contributions.

The results shown here demonstrate that, in spite of the simplicity of the model, the behavior of simulated droplets agrees quite well with experimental behavior of bulk liquids. However, a brief digression is necessary at this point. In principle, one should not compare properties of small droplets with those of bulk liquids. The vapor pressure and consequently the vapor density are higher in the case of small droplets if compared to bulk liquids, and this is known as the Kelvin-Laplace effect. Furthermore, as droplets become even smaller, the surface tension is no longer constant, but varies as function of the radius of curvature [Guggenheim'85]. Nevertheless, there are two reasons why one can disregard these effects and consider

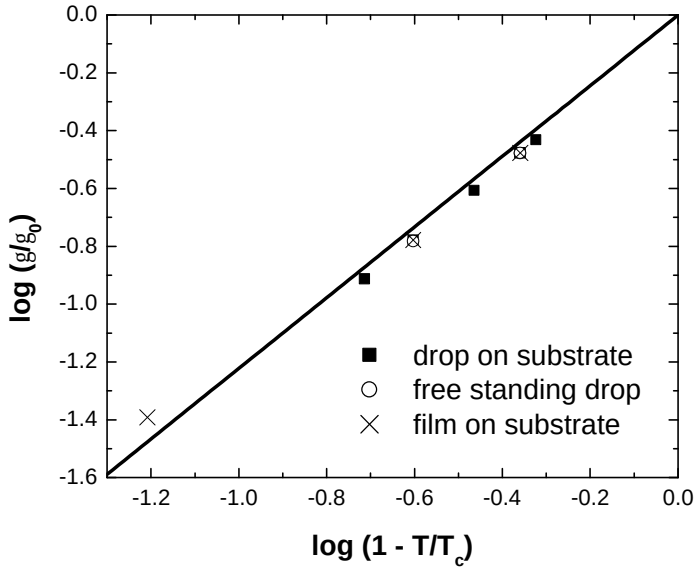

Figure 3.05 Temperature dependence of ?/?$_0$ for simulated droplets. The straight line is the behavior expected from Equation (3.13).

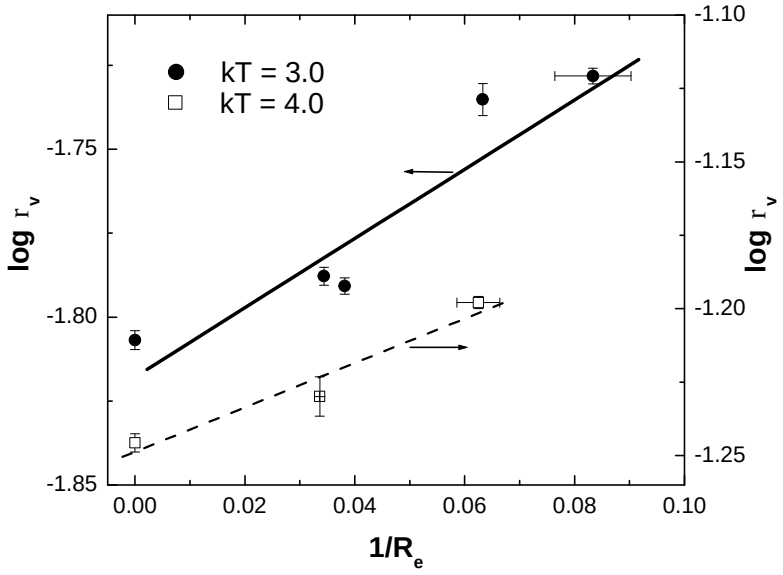

Figure 3.06 Variation of the vapor density as function of droplet equimolar radius. Straight lines represent the fittings based in the Kelvin-Laplace equation.

the droplets behaving as bulk liquids. First, simulated droplets are big enough so that the surface tension does not vary with droplet radius. Molecular dynamics studies [Thompson'84] have shown that the surface tension reaches its bulk value when the number of elements in the liquid phase is higher than 2000. In our work, the number

of elements in the liquid phase was about 10 000. Although the interface thickness of simulated droplets is not infinitely narrow if compared to the radius of curvature, as Table (3.01) and Figure (3.03) show, the equimolar Gibbs dividing surface is a reasonable approximation for the boundary between two phases. Obviously, such approximation is not unambiguous. The second point to be discussed is the influence of the Kelvin-Laplace effect on the vapor pressure. If the vapor in equilibrium with the liquid phase is regarded as an ideal gas, this effect can be expressed as:

$$P = P^{\infty} e^{2g\overline{V}/rRT}, \tag{3.14}$$

where P is the pressure of vapor in equilibrium with a droplet of radius r, P^{∞} is the vapor pressure of bulk liquid, $\overline{V}$ is the molar volume of the liquid and R the ideal gas constant. For ideal gases, the pressure is directly proportional to the density. Figure (3.06) shows that the effect really takes place on simulated droplets, but the variation of the vapor density with droplet radius is very small. In fact, it will not influence significantly the value of $r_l - r_v$. This explains why droplets with different radius provide almost the same value of $r_l - r_v$. This result is important because it demonstrates that, although simulated droplets are in the scale of nanometers, the results can be extended to bigger droplets with micrometer/millimeter size, where the Kelvin-Laplace effect is still insignificant.

As a concluding remark, the results exposed in this section show that droplets on surfaces can be realistically simulated with the cooperative motion algorithm. As mentioned before, the droplets simulated in this chapter will be used as nanoreactors for polymerization reactions in Chapter 4. Droplets will be used in Chapter 6 as well to clarify the mechanism of surface pattern formation when a droplet evaporates at a soluble surface.

4

Polymerization in Nanoreactors

4.1 Introduction to the Modeling of Equilibrium Step-Growth Polymerization in Confined Geometries

Confinement may have a significant impact on the kinetics and thermodynamics of chemical reactions. Due to space restrictions, molecules can only react with a finite number of neighbors in their proximity [Provata'93]. Moreover, interactions between molecules and reactor walls may play a major role in small systems [Lísal'06]. The reaction dynamics may also change if diffusion is hindered or slowed down as consequence of confinement. Provata *et al.* showed numerically and analytically that the equilibrium constant of a given trimolecular chemical reaction in one and two dimensions may differ considerably from the bulk value [Provata'93]. Minton *et al.* calculated the effect of confinement upon isomerization, association and binding equilibra inside model enclosures using a geometrical approach [Minton'92]. Molecules were pictured as simplified model particles, for instance spheres, rods and disks. The more complex situation of a polymer coil was treated later in the thermodynamic approach of Schmitt *et al.* for the case of dilute solutions of "living polymers", i.e. chains which can grow and break reversibly (some real examples are liquid sulfur, poly(α-methylstyrene), polymer-like micelles and protein filaments) [Schmitt'93]. The results indicate that, if such chains are confined between two solid walls, the average equilibrium chain length is shifted to smaller values. Confinement decreases the conformational entropy of polymer chains and penalizes the formation

of longer chains. The effect becomes more dramatic as the gap size approaches the average value of the chain radius of gyration. Similar trends were observed in molecular simulations by Rouault *et al.* for a denser system of living polymer chains [Rouault'97, Wittmer'98, Landau'00, Milchev'02,]. Other simulations performed by Tribet *et al.* for the case of radical polymerization show that the rate of chain propagation is decreased by confinement [Tribet'94]. However, chain rearrangements, diffusion and interchain volume exclusion interactions were not considered in this model.

4.2 Methodology

The aim of this chapter is to investigate the impact of geometrical confinement on an equilibrium step-growth polymerization reaction.

In the present work, we performed in-lattice Monte Carlo simulations of equilibrium step-growth (or living) polymerization under confinement. Computations were performed according to a variation of the CMA. The model works with highly dense systems of particles under volume exclusion conditions. Chain rearrangements and diffusion respect chain connectivity and are implemented independently from reactions of bond forming and breaking. It is difficult to find a model that regards all those details together. The impact of purely geometrical constraints in the rate and equilibrium state of the polymerization was investigated. Confinement in one, two and three dimensions was respectively represented by lamellar pores, tubes (also called square parallelopiped pores [Minton'92]) and droplets. The results show that both the polymerization rate and the equilibrium chain length decrease as confinement increases, which is in agreement with previous findings [Rouault'97]. To explain the results, we propose an analytical lattice theory which is far simpler than previous approaches. According to this model, encounters between molecules and walls become more frequent at expense of intermolecular encounters as confinement increases. This causes polymerization to slow down while bond breaking is not affected. As consequence, the equilibrium state will have smaller chains as compared to the case of unconstrained polymerization. The model rationalizes the effect as a function of the area/volume ratio of the systems independently of other geometrical features of confinement.

Experimental evidence of the simulation results is still rare for polymerization. However, our findings are in qualitative agreement with a report of Thomas *et al.* on the reversible formation of pyrene excimers inside silica nanopores [Thomas'03].

4.3 Implementation Details

To simulate a system in which molecular rearrangements and chemical reactions occur simultaneously, a variation of the CMA method described in Section (2.3) was used. As before, the algorithm performs cooperative rearrangements of molecular elements along randomly traced loops in space. Now, however, after a given number of motion attempts has been performed and the loop closed, the program makes an equal number of reaction attempts. Chemical reactions are simulated by selecting randomly an element in the lattice and one of its coordination sites. If such site is an element of the reactor wall, the reaction attempt is unsuccessful. If it does not pertain to the wall, the reaction probability is calculated at a given temperature kT by the Boltzmann factor:

$$P = f\,\mathrm{e}^{-\Delta H^{*}/kT}, \tag{4.01}$$

where ΔH^{*} is the activation energy for bond forming in case there is previously no bond between the elements or the activation energy for bond breaking if a bond already exists. The activation energy of bond formation was considered as $\Delta H_{1}^{*} = 15$ and the activation energy of bond breaking as $\Delta H_{-1}^{*} = 33$. The temperature kT was varied from 2 to 9 (all parameters in the same arbitrary unit). The values of activation energies and temperatures were empirically adjusted in order to optimize simulations. The rate of bond formation needed to be low enough so that the kinetics could be appropriately followed in time, but also high enough so that reactions could reach equilibrium within reasonable computation time. The difference between the activation energies of bond formation and bond breaking determines the conversion and the average molecular weight at equilibrium. Reactions simulated here had high conversion at equilibrium and, by varying the temperature between 2 and 9, a range of chain lengths varying over one order of magnitude could be accessed.

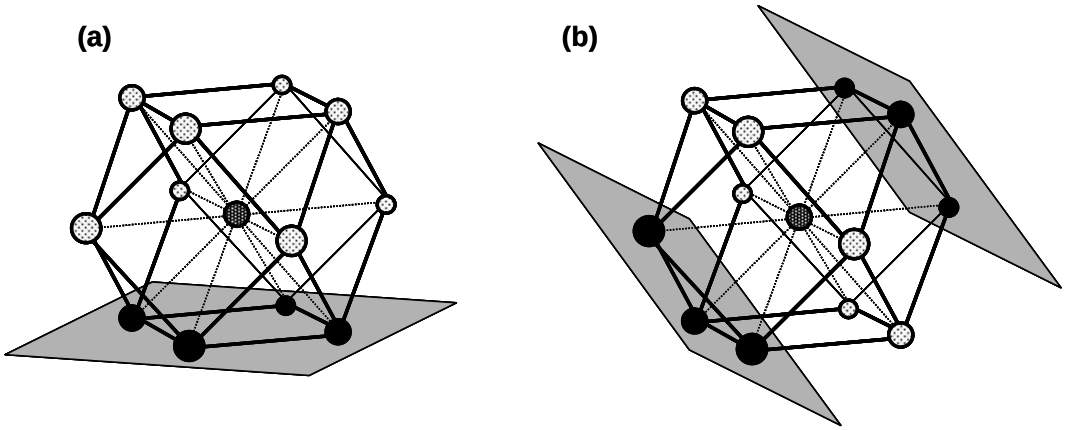

Figure 4.01 The coordination cell of (a) the face centered cubic lattice (fcc) and (b) the triangular or hexagonal two-dimensional lattice. In both cases, the element in the center (dark grey) is located one layer below a wall, here represented as a grey surface. Black spheres represent elements that pertain to the wall and therefore do not react. In the case of a fcc lattice, for instance, reaction attempts in only 8 of the 12 coordination directions have chance to be successful.

During simulations, a bond is formed or broken if P is higher than a random number between 0 and 1 generated by the computer. Monomers are considered to have two reacting functional groups and cannot bind to more than two other elements. Chains formed this way do not have branches. The formation of chain rings is also forbidden by the program. It is assumed that the rotation of a single monomer with two free functional groups occurs in a much shorter time scale compared with the reaction time scale. Therefore, the parameter f is set as 4 if the reaction involves two single monomers. This corresponds to the 4 possible ways of combining their 4 functional groups in pairs. Analogously, f is set as 2 for reactions between a monomer and a chain end or as 1 for reactions involving two chain ends or bond breaking. Simulations started with all reacting molecules in the state of monomers. After bonds are formed, the collective motions of molecular elements must respect chain connectivity. This means that only an explicit reaction is able to break a chain. Chain rearrangements were regarded as athermal and no interactions besides volume exclusion were implemented during simulations in the bulk, lamellar pores or tubes. Bulk polymerization was simulated in a cubic box with periodic boundary condition in all directions. It had dimensions of 60 monomer elements in each direction, totalizing approximately 10^5 elements. Confinement was implemented by putting two rigid walls perpendicular to a given direction. Systems with smaller distance between

walls were investigated but always keeping the total volume practically constant. As shown in Figure (4.01), a fcc lattice with 12 nearest neighbors was used as the coordination skeleton in the simulations. However, for the extreme case of polymerization in a monolayer, a triangular or hexagonal lattice type was used so that chain mobility would not be compromised by a reduced number of nearest neighbors. Tubes were simulated by adding four walls and keeping the boundaries periodic in only one direction. The conversion of functional groups was recorded as function of time, keeping the same time definition as in Section (2.3). After equilibrium has been reached, quantities such as chain length distribution were sampled for the calculation of thermodynamic averages.

Simulations of droplets followed a similar scheme but now a multiphase system was implemented. Elements were regarded as having three types of identity. They were labeled to represent either monomer particles (MO), substrate particles (SU), or vacuum (VA). Monomer liquid droplets sitting at solid surfaces were generated following the method described in Section (3.2) [Cordeiro'05]. The initial system configuration was a cubic droplet of pure monomer placed upon a layer of substrate material and surrounded by vacuum. The simulation then started and proceeded until the cubic droplet had relaxed to a droplet with the shape of a spherical cap. At this stage, no chemical reaction was performed by the program. Polymerization was allowed to start only after monomer droplets have reached their equilibrium shape. The interaction parameters of monomers were assumed not to change as they form bonds with other elements. These simulations provide an example of confinement in three dimensions and are closely related to experimental systems. Furthermore, the interface between droplets and vapor is mobile and, as will be shown, it gives rise to a more complex behavior in comparison to confinement between hard walls.

4.4 Simulation Results and Analytical Theory for Lamellae, Tubes and Droplets

The influence of confinement on the average number of elements that chains have at equilibrium is depicted in Figure (4.02). It brings results for several temperatures, geometries and degrees of confinement. Confinement is defined as the ratio between the number of elements that constitute the inert surface walls divided by

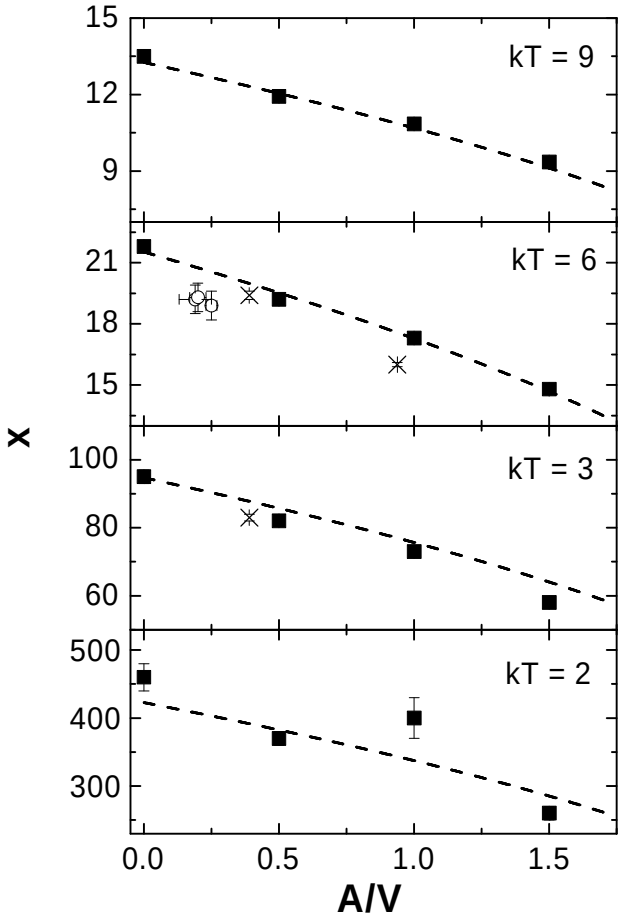

Figure 4.02 Average number of elements in the polymer chains (*x*) at the equilibrium condition as function of the confinement parameter *A*/*V*, which is related to the area/volume ratio of different systems. The value 0 represents the bulk (fcc lattice), 1 represents a monomer bilayer (fcc lattice) and 1.5 a monolayer (hexagonal lattice). Results are presented for several temperatures. Simulation data were obtained for confinement between two hard walls, i.e. in lamellar pores (■), inside parallelopiped tubes (x) and inside droplets (o). Dashed lines represent the predictions of the corrected version of the analytical lattice model derived in the text.

the total number of reactive elements in the system (in this case, excluding the inert walls). For the sake of simplicity, it will be named here as an area/volume ratio. It equals 0 for bulk systems and 1 for the case of a lamellar pore whose thickness is equivalent to a monomer bilayer. Figure (4.02) shows that, as confinement increases, the average chain length at equilibrium decreases and that even systems with different geometries follow a common dependence on the area/volume ratio. In the following we derive an analytical model based on probability theory in order to rationalize the trends observed in the simulations.

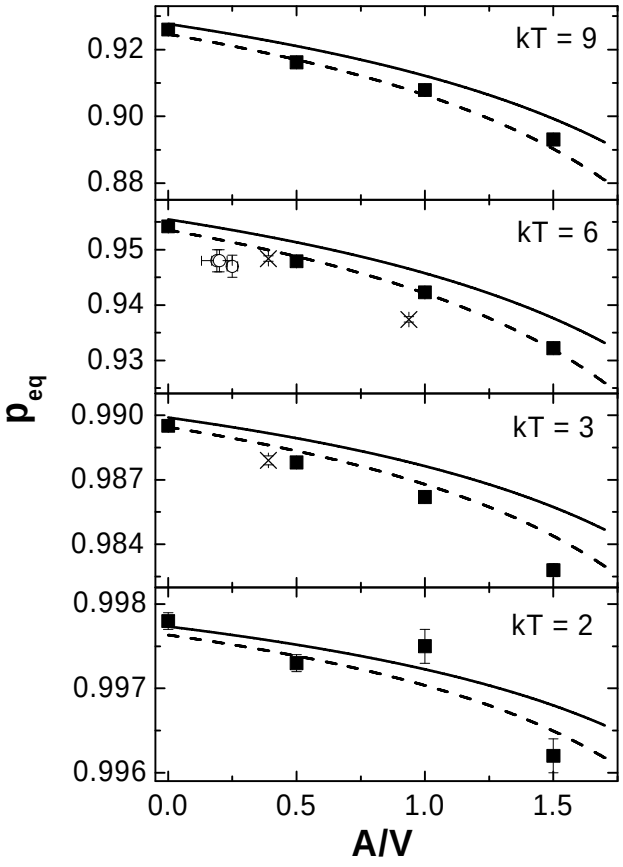

Figure 4.03 Conversion at the equilibrium condition as function of confinement for several temperatures. Simulation data were obtained for confinement between two hard walls, i.e. in lamellar pores (■), inside parallelepipedal tubes (x) and inside droplets (o). Full lines represent the predictions of the analytical lattice model derived in the text without consideration of change in reactivity of the functional group as the reaction proceeds. Dashed lines incorporate such correction.

First, the reversible step-growth polymerization can be understood in a simpler way as the following elementary reaction:

$$\mathbf{N} + \mathbf{N} \underset{k_{-1}}{\overset{k_1}{\rightleftharpoons}} \mathbf{B_2} \qquad (4.02)$$

where N represents a nonbonded functional group, B_2 a bond and k_1 and k_{-1} the rate constants of the reaction in both directions. Details about chain connectivity and diffusion, although considered in the simulations, were neglected at this first stage of the analytical model. The reaction rate can be expressed based on the mass action law:

$$\frac{dp}{dt} = 4k_1 C_0 (1-p)^2 - k_{-1} p \,, \tag{4.03}$$

where C_0 represents the concentration of monomers (half of the concentration of functional groups) in a system entirely constituted only by monomers. The parameter p stays for the conversion, i.e., the fraction of functional groups which have been converted to bonds at a given time t. The effect of confinement upon conversion in equilibrium is shown in Figure (4.03). Higher conversions mean longer average chain lengths because p is related to the average number of elements in a chain (x) by:

$$\langle x \rangle = (1-p)^{-1} \,. \tag{4.04}$$

The exact solution of Equation (4.03) leads to:

$$\ln(r_+ / r_-) = (16 C_0 K + 1)^{0.5} k_{-1} t \,, \tag{4.05}$$

where:

$$r_\pm = 1 - \frac{8 C_0 K p}{8 C_0 K + 1 \pm (16 C_0 K + 1)^{0.5}} \,, \tag{4.06}$$

being K the equilibrium constant of the reaction in Equation (4.02). The constant K may be alternatively expressed as the ratio between k_1 and k_{-1}. Now, it is necessary to draw a connection between the previous phenomenological equations and the probabilistic nature of simulations. For this, let us consider a system composed only by free monomers. Before any reaction has taken place, the initial reaction rate in such simulation is then given by the reaction probability of the first sampled element:

$$\left(\frac{d[\mathrm{B}_2]}{dt} \right)_{t=0} = 4 \, \mathrm{e}^{-\Delta H_1^* / kT} \,, \tag{4.07}$$

and k_1 follows as:

$$k_1 = \frac{1}{4C_0^2}\left(\frac{d[\mathrm{B}_2]}{dt}\right)_{t=0} = \mathrm{e}^{-\Delta H_1^* / kT}, \tag{4.08}$$

As a convention, the concentration C_0 will be considered as 1 in terms of arbitrary units. Equation (4.08) accounts only for polymerization in the bulk. Considering the specific case of a fcc lattice, Figure (4.01) shows that, if walls are present, elements close to these boundaries have no longer 12 nearest neighbors but only 8. This means that reaction attempts in 4 directions will always be unsuccessful since they lead to encounters with the inert wall. In the analytical model developed here, this change in reaction frequency is incorporated in Equation (4.08) by writing the rate constant under confinement (k_1') as $k_1' = a\ k_1$. The parameter a considers the fact that elements directly close to the wall have a different contribution to the value of reaction rate if compared to elements far from the wall. This parameter is given by:

$$a = \left(\frac{A}{V}\cdot\frac{8}{12}\right) + \left(\frac{V-A}{V}\cdot\frac{12}{12}\right) = 1 - \frac{A}{3V}, \tag{4.09}$$

where A is the number of elements that constitute the inert surface walls and V is the total number of reactive elements in the system (excluding the walls). The influence of the area/volume ratio is explicitly addressed by Equation (4.09). The same treatment can be easily extended to any other kind of lattice. The expression above clearly depends on the lattice type considered but the area/volume dependence should hold for all cases.

Although the rate constant k_1' is assumed not to vary during polymerization, this is not a very realistic assumption since chain entanglements and the formation of blocking loops tend to decrease the functional group reactivity as chains grow. To take this into account and describe more precisely the reaction dynamics and the equilibrium state at high conversions, the polymerization rate constant can be calculated based on a hypothetical system initially composed only by dimers instead of monomers. This means that one coordination site is already occupied by a bond and is not available for a bond forming reaction. A corrected rate constant k_1'' which

describes systems at high conversions is then written as $k_1'' = b\ k_1$, being the confinement parameter b given by:

$$b = \frac{11}{12} - \frac{A}{3V}. \tag{4.10}$$

The treatment above can be easily extended to the two-dimensional hexagonal lattice so that the results obtained from such system can be compared with the same equations used for the fcc lattice. In the case of the hexagonal lattice, it is clear by analyzing Figure (4.01) that b should have the value of $\frac{5}{12}$. In order to use the same equations as for the fcc three-dimensional lattice, we assign to the hexagonal two-dimensional lattice an equivalent value of the area/volume ratio, $(A/V)_{eq}$, so that:

$$\frac{11}{12} - \frac{1}{3}\left(\frac{A}{V}\right)_{eq} = \frac{5}{12}. \tag{4.11}$$

And from this we have that $(A/V)_{eq} = 1.5$ for the hexagonal lattice.

So far, only the bond forming reaction has been discussed. Following the same logic for bond breaking, it is possible to demonstrate that:

$$k_{-1} = \frac{1}{6} e^{-\Delta H^*_{-1}/kT}. \tag{4.12}$$

The parameter $\frac{1}{6}$ reflects the fact that, in a hypothetical system totally converted to polymer, each element has 2 bonds and bond breaking can occur only in 2 of the total 12 coordination sites. This rate constant is independent of confinement and does not change as polymerization proceeds. The kinetic rate constants are related to the conversion at equilibrium by:

$$\frac{k_1''}{k_{-1}} = K = \frac{p_{eq}}{4(1-p_{eq})^2}. \tag{4.13}$$

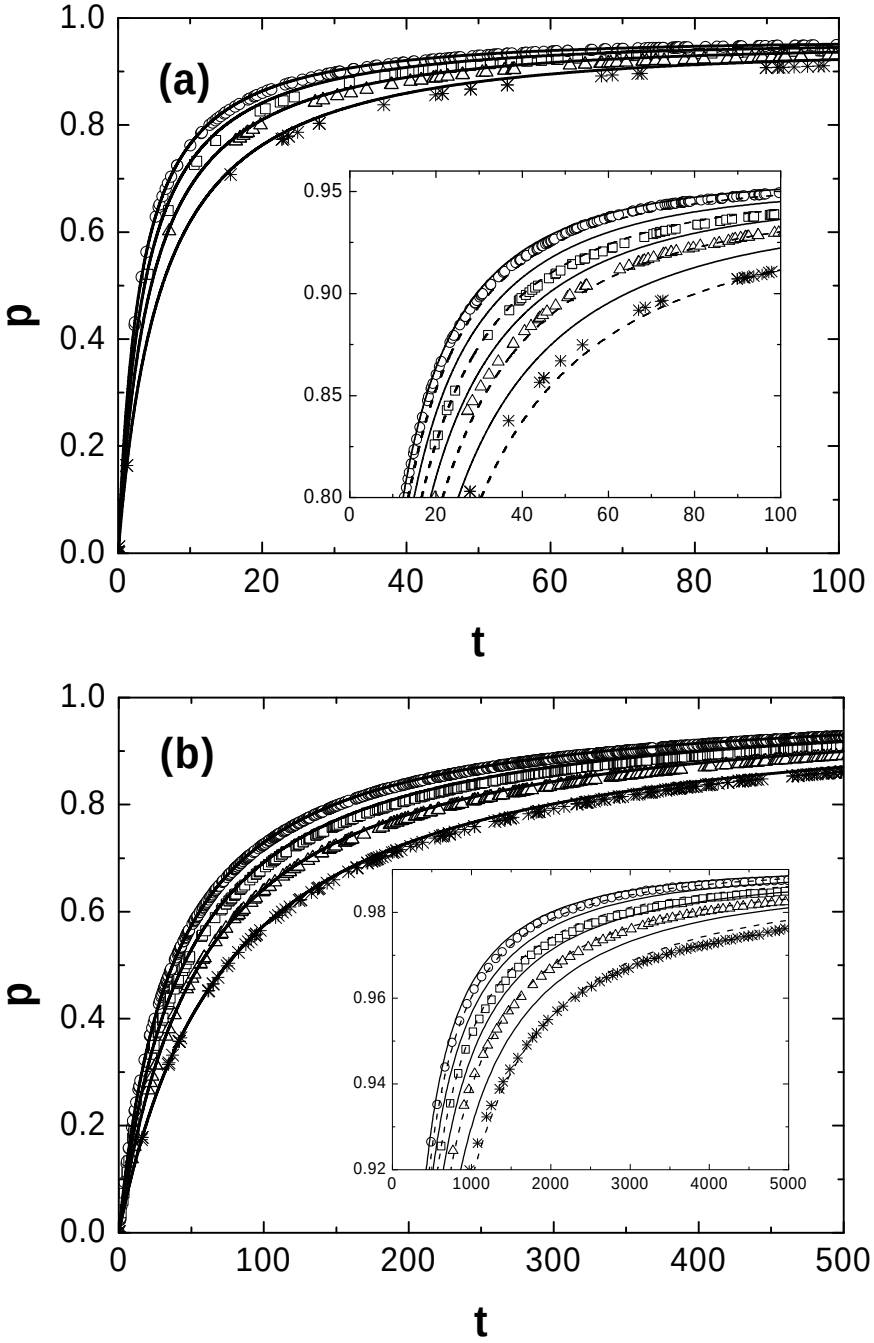

Figure 4.04 Variation of conversion as function of time for (a) kT = 6 and (b) kT = 3. In both cases, simulation results are presented for systems in which the parameter A/V equals 0 (o), 0.5 (□), 1 (△) and 1.5 (*). Insets show more closely the region corresponding to higher conversions. Full lines represent the analytical theory without correction for the decrease in reactivity of the functional group. They are in good agreement with simulation results at initial times. Dashed lines represent the corrected version of the analytical model. They agree with simulations as the reaction approaches equilibrium at high conversions.

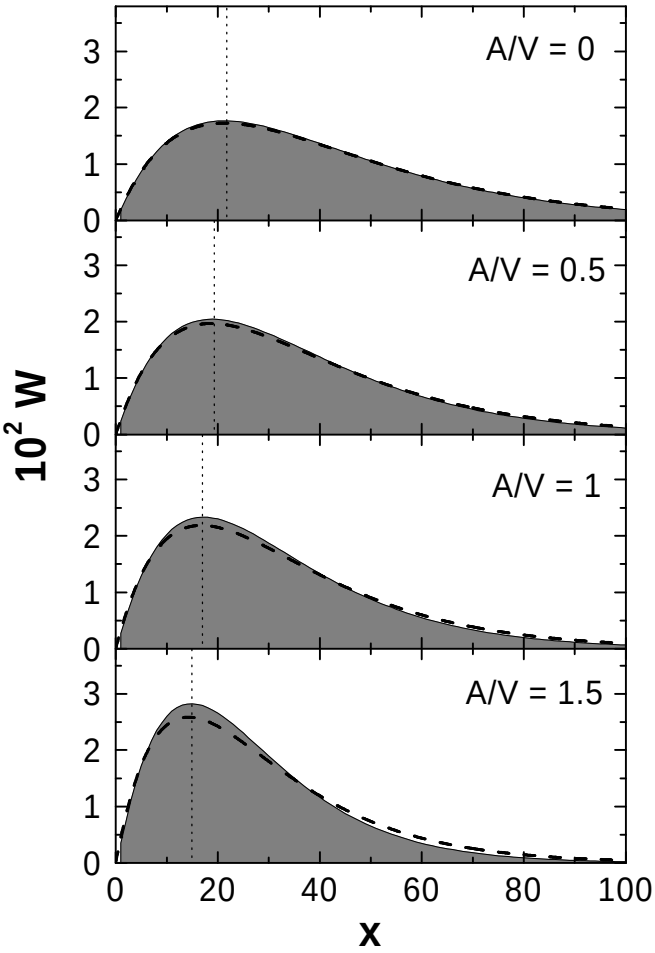

Figure 4.05 **"**Molecular weight" distribution of systems at equilibrium at kT = 6 and under different degrees of confinement. Grey area represent distributions obtained from simulations and dashed lines the predictions from to Equation (4.14). Dotted lines indicate the average value of "molecular weight", here understood as the average number of elements in the chains.

If the activation energies and temperature adopted as simulation parameters are substituted in the analytical expressions for k_1" and k_{-1}, a very good agreement between simulations and the analytical lattice model is observed, as depicted in Figures (4.02) and (4.03). The agreement is worse at lower temperatures because the dynamics of bond forming and breaking becomes slower and this enhances the influence of additional phenomena such as diffusion and formation of blocking loops. Consistence is also observed for the variation of conversion as function of time, as shown in Figure (4.04). Under confinement, the reaction needs more time to reach equilibrium. The agreement at high conversions is better using the polymerization rate constant corrected for change in reactivity. All results presented here show that, to a

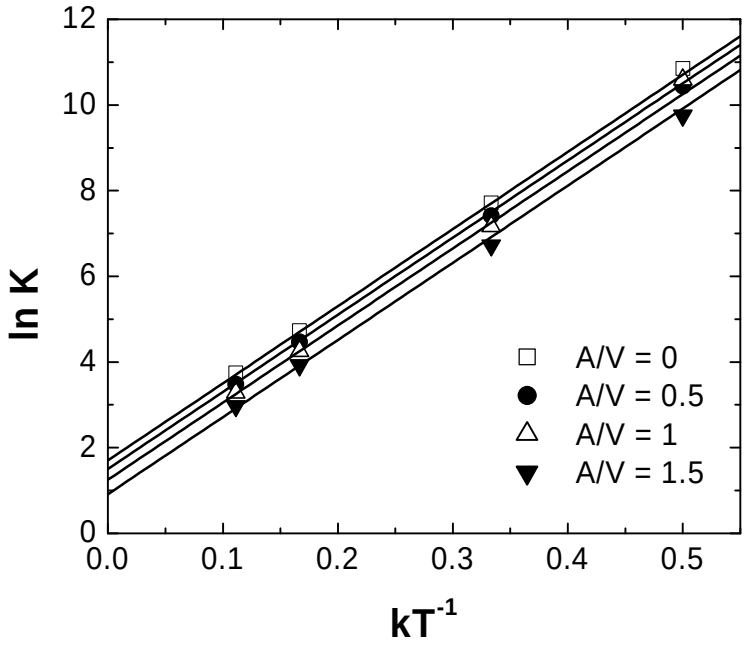

Figure 4.06 Temperature dependence of the equilibrium constant for systems under various degrees of confinement. Symbols represent simulation results and full lines the predictions according to Equations (4.15), (4.16) and (4.17).

good approximation, all geometries fall in the same tendency, showing that the area/volume ratio is the major aspect influencing the final average length of the chains. The shape of the chain length distribution at equilibrium is influenced by confinement as well. Figure (4.05) compares the distribution obtained from simulations with the analytical form of the most probable distribution [Tanford'61]:

$$W_x = xp^{x-1}(1-p)^2\,, \tag{4.14}$$

where W_x stays for the "weight fraction" of a given x-mer in the system. The conversion at equilibrium obtained from simulations is substituted in Equation (4.14) as the parameter p. It is observed that, as confinement increases, the length distributions from simulations slightly deviate from Equation (4.14) and are shifted to lower values.

The analytical lattice model can be also extended to the determination of thermodynamical parameters of the reaction. The enthalpy involved in the generation

of one bond is given by means of the activation energies implemented in the simulations as:

$$\Delta H = \Delta H_1^* - \Delta H_{-1}^* = -18\,. \tag{4.15}$$

A simple probabilistic analysis leads to an analogous expression for the reaction entropy:

$$\Delta S = k \ln(6b)\,. \tag{4.16}$$

Both values are related to the constant of equilibrium by [Castellan'83]:

$$\ln K = \frac{\Delta S}{k} - \frac{\Delta H}{kT}\,. \tag{4.17}$$

Figure (4.06) brings a comparison between the temperature dependence of K as obtained from simulations and from Equations (4.15), (4.16) and (4.17). Again, a good agreement is found. The reaction entropy (i.e., the value of ln$K$ at an infinitely high temperature) is shown to decrease as the area/volume ratio increases. This is consistent with the view that confinement decreases the number of possible conformations of a chain and therefore penalizes its growth.

The influence of entropy is clearly observed in the simulations of polymerization in a monomer droplet, where the interface between droplet and air is mobile. Figure (4.07) shows that, for the systems labeled as drop 1 and drop 2, the contact angle after polymerization is higher in comparison with the initial droplet constituted only by free monomers. This reflects the tendency of such systems to decrease their own area/volume ratio and compensate the conformation restrictions imposed over the chains by confinement [Zhao'93]. The system labeled as drop 3, however, does not obey the tendency above. Additional effects such as the balance of surface tensions between different phases in the contact line may play a more important role than confinement in this case. Moreover, as polymerization proceeds, monomer elements in vapor coalesce as small droplets changing the vapor

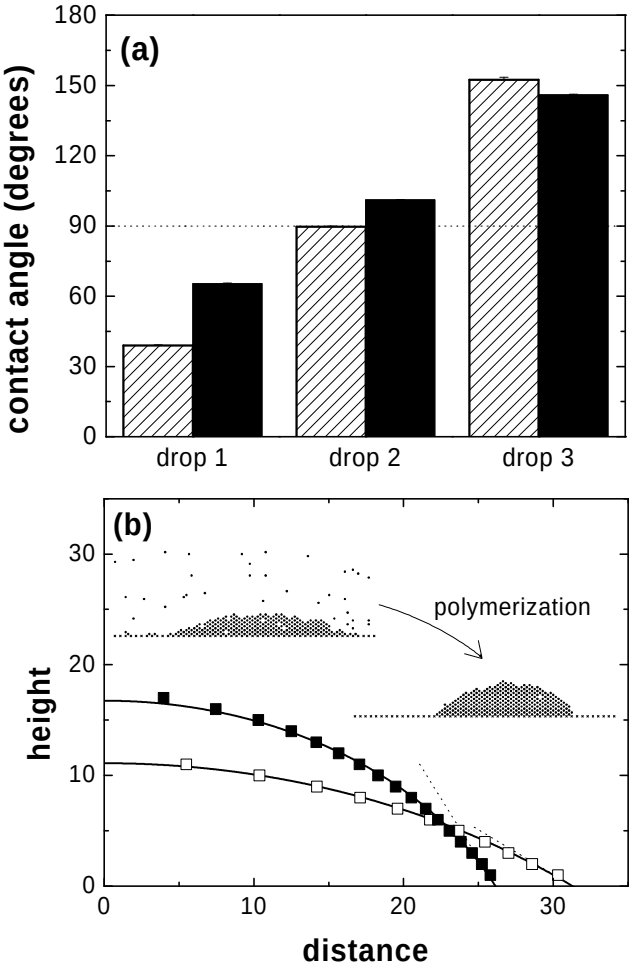

Figure 4.07 (a) Droplet contact angles before polymerization starts (shaded rectangles) and after equilibrium has been reached (black rectangles) for three droplets with different shapes, i.e. different interaction parameters (see Section (3.2)). (b) Detailed view of the evolution of the shape of drop 1 before (□) and after (■) polymerization. Distances are expressed in terms of the lattice unit length. Full lines represent a spherical cap fitting and dashed lines represent the contact angles. Pictures in the inset are snapshots from simulations.

composition. This introduces more variables in the systems and makes the analysis more complex.

4.5 Final Considerations

The cooperative motion algorithm was applied in the simulation of an equilibrium step-growth polymerization in the bulk and under confinement. As confinement increases, polymerization is slowed down and the average chain length at

equilibrium decreases. To a good approximation, the effect is a function of the area/volume ratio of the nanoreactors, independent of other geometrical features. A simple probabilistic analytical model was derived to rationalize the results. According to this model, encounters between molecules and the reactor walls become more frequent at the expense of intermolecular encounters as confinement increases. This causes the polymerization rate to decrease. Differently, bond breaking does not depend on encounters and its rate does not change. As a consequence, the conversion is smaller and the formation of longer chains is penalized under confinement. Although the results derived here depend on the type of lattice considered, the dependence of the average chain length at equilibrium on the area/volume ratio should hold regardless of the coordination number. We predict that experiments will follow a similar trend based on the average coordination number in the liquid, provided that additional effects such as van der Waals interactions with the walls can be neglected. The implementation of energy interactions between molecules and the walls as well as the study of polymers with more complex topology (for instance polymer brushes, dendrimers and stars) are possible extensions of this work. Further refinements may be needed in the model to account for changes in density happening when fluids are confined in small pores. This could influence significantly the results. The effect of confinement over more complex reactions such as chemical oscillations is also in the scope of the model proposed here.

Finally, we hope the ideas developed here can contribute to stimulate further experimental investigations about chemical reactions under confinement. Direct quantitative evidence of the impact of geometrical confinement on polymerization reactions is still rare in literature. We are not aware of experimental studies relating confinement to the average molecular weight obtained at equilibrium. However, our results are in qualitative agreement with experiments of pyrene dimerization in silica pores [Thomas'03]. In these experiments, it was observed that the conversion from monomer to dimer at equilibrium decreased as the pore size decreased. Confinement leads to a lower probability of association of two monomers, a trend that is also observed in our simulations of polymerization.

5

Polymer Chain Orientation in Confined Geometries

5.1 Scientific Background

Thin polymer films show many perspectives for optoelectronic device applications such as optical waveguides for integrated optics [Tien'77], nonlinear optical switching [Bahtiar'04], polymer light emitting diodes (LEDs) [Friend'99] and plastic lasers [McGehee'00]. The performance of these devices depends strongly on chain packing morphology and molecular orientations within the layers [McGehee'00]. It is well known that thin polymer films may be highly anisotropic [Prest'79, Prest'80, Russel'83, Boese'92, Lin'93, Lin'94, Ree'94, Coburn'94, Li'97, Li'99, Lee'03, McBranch'95, Tammer'02, Koynov'04, Koynov'06]. Typically, they show a preferred orientation of polymer chains parallel to the substrate plane. This alignment causes birefringence of the films, i.e., in-plane and out-of-plane refractive indices may be significantly different. The amount of birefringence of the films depends on many parameters, for example molecular weight and stiffness of the polymers, film thickness, film preparation conditions (casting and annealing temperatures, solution flow conditions etc.) [Prest'80, Frank'96, Law'00, Losurdo'03, Koynov'06]. Of particular interest are the so-called conjugated polymers, which possess highly stiff chains and large π-electron delocalization along the polymer backbone. Examples are poly-arylene-phenylenes [Losurdo'03] and derivatives of poly-para-phenylene-vinylene (PPV) such as poly-2-methoxy-5-(2'-ethylhexyloxy)-1,4-phenylenevinylene (MEH-PPV) [McBranch'95, Tammer'02, Koynov'04,

Koynov'06]. Conjugated polymers are suitable for application in optoelectronics. However, systematic experimental and theoretical studies of the influence of their molecular parameters (e.g. chain stiffness, molecular weight, chain defects etc.) are rare [Hu'00, Koynov'04, Koynov'06]. Optimization of the performance of optoelectronic devices clearly needs improved knowledge of the chain packing morphology and orientation of chain segments. It is known, for example, that the intensity of light emitted by polymer LEDs is strongly connected to chain orientation in the film [Losurdo'03]. Moreover, it was recently recognized that the optical constants and the morphology of thin films of the model conjugated polymer MEH-PPV depend significantly on its molecular weight [Koynov'04, Koynov'06]. Any optical application of polymer films requires the control of refractive index and birefringence which is desired to be either large or small depending on the kind of application. Consequently, the control of the morphology of thin polymer films is an important but currently unsolved problem.

5.2 Methodology

The aim of this chapter is an improved basic understanding of the structure-property relations, in particular the influence of the polymer structure (rigidity of the polymer backbone and molecular weight) on the orientation distribution and birefringence of thin polymer films. To accomplish this, we have chosen an approach combining computer simulations and experiments. The first part of this study is concerned with the simulation of polymer chains in thin films. The objective is to get information about the orientation phenomena on a molecular scale. The CMA method is well suited for the modeling of the arrangement of polymer chains at the substrate interface. In fact, the method has been successfully applied in the simulation of thin films of polymer melts between rigid substrate layers [Pakula'91, Gauger'93, Pakula'00a, Pakula'04]. Simulations are intended to address the effect of geometrical confinement on the equilibrium configuration of polymer chains confined between non-interacting rigid walls. It is important to point out, however, that such a simplified picture of a polymer film is not expected to agree with experimental results in all cases. Film preparation involves complex processes such as the drying of a polymer solution. Consideration of additional phenomena related to the dynamics of

solution drying, aggregate formation in solution, appearance of crystalline domains in the film and non-equilibrium effects may be crucial for describing the experimental reality. Although these effects are outside the scope of the modeling work performed here, our simulation results are still able to provide valuable insights. Their comparison with the experimental behavior allows the identification of experimental situations in which the reasons for orientation lie to a good approximation in the geometrical confinement. In fact, as will be shown later, this is the case for thin films of low molecular weight polystyrene. Analogously, large divergences between experiments and simulations indicate that additional effects not considered in the model may play a major role in reality. For this reason, this work is also based on a systematic analysis of literature database in order to identify in which extend the simulations are able to reproduce the experimental reality for various materials. It turned out, for instance, that the chain orientation in films of MEH-PPV and polyfluorene (see Figure (5.01) for the chemical structures) could not be satisfactorily described by simulations, meaning that chain orientation could not be reduced to a simple confinement effect. The verification of such disagreement between experiments and simulations became clear after these materials were selected and we performed our own experiments in order to measure the orientation of polymer chains in thin films [Koynov'06]. The experimental techniques were based on the measurement of optical properties. The anisotropy of the refractive index is used as an indication of the degree of orientation, as will be described later. The experimental results in the present work are compared with simulations and, in a final stage, the limitations of the CMA are discussed and suggestions for possible extensions of this work are presented.

5.3 Simulation of Orientation of Polymer Chains Confined Between Rigid Walls

5.3.1. Implementation Details

The CMA method was applied in the simulation of polymer chains as described in Section (2.3). At the present stage, attention was focused on the simulation of dense and homogeneous systems constituted by an ensemble of polymer chains confined between two rigid parallel walls. Periodic boundaries were implemented parallel to such walls in order to mimic a thin polymer film with infinite

PMDA-PDA (rigid polyimide)
poly(*p*-phenylene pyromellitimide)

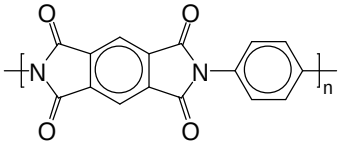

polystyrene

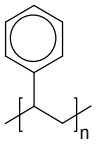

BPDA-PDA (semirigid polyimide)
poly(*p*-phenylene biphenyltetracarboximide)

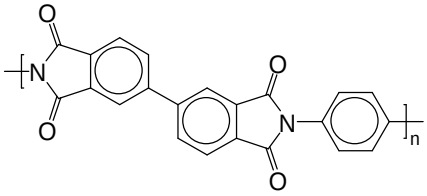

MEH-PPV
poly[2-methoxy-5-(2'-ethylhexyloxy)-1,4-phenylenevinylene]

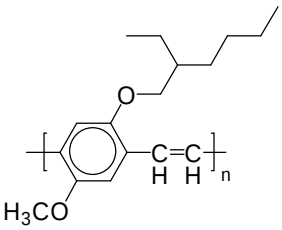

PMDA-ODA (semiflexible polyimide)
poly(4,4'-oxydiphenylene pyromellitimide)

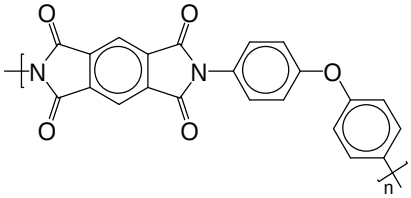

polyfluorene
poly[9,9-di-(2-ethylhexyl)-fluorenyl-2,7-diyl]

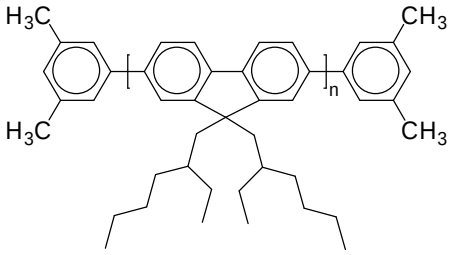

BTDA-ODA (flexible polyimide)
poly(4,4'-oxydiphenylene benzophenonetetracarboximide)

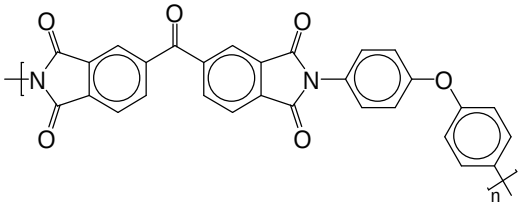

Figure 5.01 Chemical structures of different polymers.

lateral dimensions but finite thickness. Thickness was varied between 19 and 99, expressed in lattice unit lengths (see Figure (4.01) for a representation of the fcc lattice). In order to minimize finite size effects related to periodic boundaries, lateral dimensions had a value of 49, which is bigger than the characteristic dimensions of simulated chains. The number of elements in the chains, which is equivalent to the molecular weight, was varied between 20 and 200. Simulations of monodisperse chains started from an arbitrarily chosen initial configuration in which all chains were ordered and perfectly oriented perpendicular to the walls (even if chains were longer than the film thickness and needed to be folded many times). Differently from Chapter 4, chemical reactions were not allowed to occur, meaning that the length of each individual chain was conserved and no chain growth nor breaking was allowed to occur. Collective motion of chain elements was performed iteratively so that chains could change from the initial state to the equilibrium condition. Since systems were constituted by only one component, i.e., the polymer, the calculation of the probability of given rearrangements by means of Equation (2.23) was not implemented in the program. Rather than that, for the case of fully flexible chains, motions were considered as athermal and chain connectivity was the only condition determining whether a rearrangement occurred or not. To simulate chains that are a little more rigid, movements leading to bond angles smaller than 120° were penalized by fixing their probabilities as 5 % once they were attempted. It is important to point out that, although chains generated this way will be called “rigid”, they are still considerably far away from the picture of a rigid rod commonly referred in experiments. Increasing even more the penalization for small angles would generate chains which are closer to this picture, but would also represent much higher and eventually non-practicable time and computational costs.

The orientation of the coarse-grained bonds and the end-to-end vector of polymer chains was quantified by means of the orientation correlation function f [Russel’83, Kumar’88, Kumar’90, Pakula’91, Gauger’93, Doruker’02]:

$$f = \frac{1}{2}\left(3\left\langle \cos^2 q \right\rangle - 1\right), \tag{5.01}$$

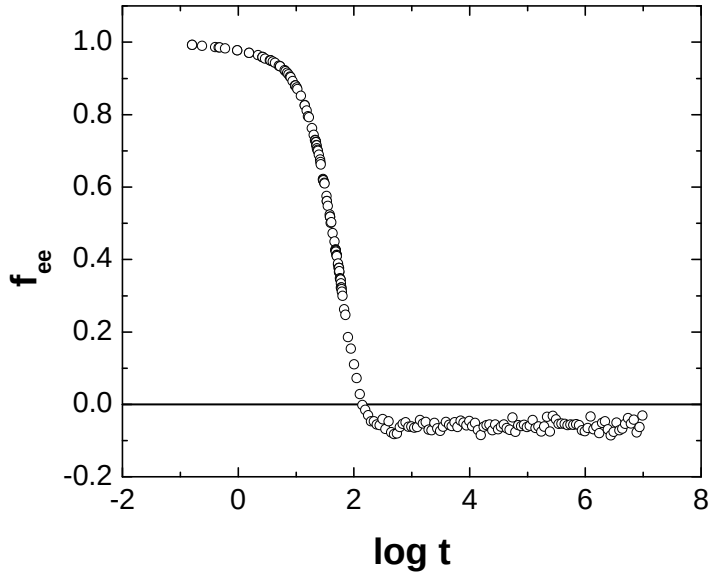

Figure 5.02 Relaxation of the end-to-end vector orientation from the initial state to equilibrium for fully flexible chains having 20 elements each. The film thickness corresponds to 19 lattice unit lengths. The definition of the time *t* in simulations follows the discussion in Section (2.3).

where q is the angle a given vector keeps in relation to the reference vector normal to the film surface. With this definition of f it is possible to distinguish three representative cases:

1) $\langle \cos^2 q \rangle = 1 \Rightarrow f = 1$: all vectors oriented perpendicular to the surface;

2) $\langle \cos^2 q \rangle = 1/3 \Rightarrow f = 0$: vectors randomly oriented;

3) $\langle \cos^2 q \rangle = 0 \Rightarrow f = -0.5$: all vectors oriented parallel to the surface.

The definition of an orientation function allows one to follow in time the relaxation of the end-to-end vector of polymer chains from the initial state to equilibrium, as illustrated in Figure (5.02). Initially, all chains are perfectly oriented perpendicular to the surface and f equals 1. As relaxation proceeds, f decreases until reaching a plateau. Averaging the points in this plateau gives the value of orientation at equilibrium. Note that this value is not zero as expected for randomly oriented chains, but slightly negative. The reason is that the walls induce a preferential orientation of the end-to-

TABLE 5.01: Simulation Parameters and Calculated Values of Kuhn Length

film thickness[a]	elements per chain	Kuhn length[a,b]	
		fully flexible	slightly rigid
19	20	1.75 ± 0.04	4.63 ± 0.09
	50	1.75 ± 0.06	5.4 ± 0.2
	100	1.69 ± 0.09	5.5 ± 0.3
49	20	1.79 ± 0.02	4.76 ± 0.06
	50	1.84 ± 0.04	5.7 ± 0.1
	100	1.84 ± 0.06	6.1 ± 0.2
99	20	1.80 ± 0.02	4.81 ± 0.04
	100	1.89 ± 0.04	6.4 ± 0.2
	200	1.89 ± 0.06	6.8 ± 0.1

[a] Expressed in lattice unit lengths.

[b] Error estimated by standard deviation.

end vector in the direction parallel to the surface. For systems comprising walls and chains, this is considered as a *self-induced orientation*.

Not only the orientation function but also the average squared end-to-end distance and the Kuhn length were calculated at equilibrium. Other characteristic quantities such as the radius of gyration or the distribution of end-to-end distances are not presented here but we refer the reader to previous publications which demonstrate the validity of the method and where the simulation of static properties of polymer chains was addressed in more detail [Pakula'91, Gauger'93]. In fact, it was shown that the CMA reproduces the basic scaling laws and size distributions associated with Gaussian statistics for dense polymer melts [Gauger'93].

5.3.2. Simulation Results

Table (5.01) lists the values of film thickness and number of elements per chain adopted as parameters in the simulated systems. It also depicts the Kuhn length calculated for simulated polymer chains. Since flexible polymer chains in the size range explored in this work were previously shown to reproduce to a good approximation Gaussian statistics [Gauger'93], Equation (2.17) was used to determine the Kuhn length from the average square end-to-end distance $\langle R^2 \rangle$, which is a value easily obtained from simulations. Representing the Kuhn length as b_{eff} and being R_{max} the chain contour length, which is equal to Nb_{eff} (see Section (2.2.1) for a brief review of structural properties of polymer chains), the following relation is obtained:

$$b_{eff} = \frac{\langle R^2 \rangle}{R_{\max}}. \qquad (5.02)$$

Table (5.01) shows that, for fully flexible chains, the Kuhn length is approximately $\sqrt{2}$, the length of a coarse-grained bond. The method of implementing rigidity in simulations is observed to be consistent. The penalization for smaller angles is reflected in the higher value of Kuhn length in comparison to fully flexible chains. This means that, in slightly rigid chains, subsequent single bonds are correlated and a statistically independent segment comprises approximately 3 to 5 single bonds. A general trend is observed especially in the case of slightly rigid chains: their Kuhn length increases as the "molecular weight" (number of elements per chain) increases or as the thickness increases. This may result both from the confinement effect and also from deviations of shorter rigid chains from the assumed Gaussian behavior due to the small number of independent segments.

To quantify the chain alignment in different systems, the average orientation function of the end-to-end vector f_{ee} was calculated. Figure (5.03) shows how the orientation depends on "molecular weight" and film thickness. Keeping a constant thickness, the chains become more oriented parallel to the surface of the film as the "molecular weight" increases. A preferential orientation parallel to the surface is denoted by the negative value of f_{ee}. Analogously, chains also become more oriented if the "molecular weight" is kept constant and the thickness decreased. The tendency is similar for fully flexible and slightly rigid chains. The only difference is that rigidity enhances the effect. It is tempting to explain the simulation results as a size effect. If this is true, an analogy between the dependence on "molecular weight" and the dependence on thickness must be found. In order to investigate this issue, we collected all the values of f_{ee} and plotted them in Figure (5.04) as a function of the ratio between the end-to-end distance and the film thickness. By doing this, it is observed that all simulation results fall in a master curve (a formal derivation of the straight line and its slope is given in Section (5.3.3)). This shows that, in the range of thicknesses, molecular weights and rigitities simulated here, chain orientation is merely a geometrical effect induced by the ratio between the dimensions of the chains

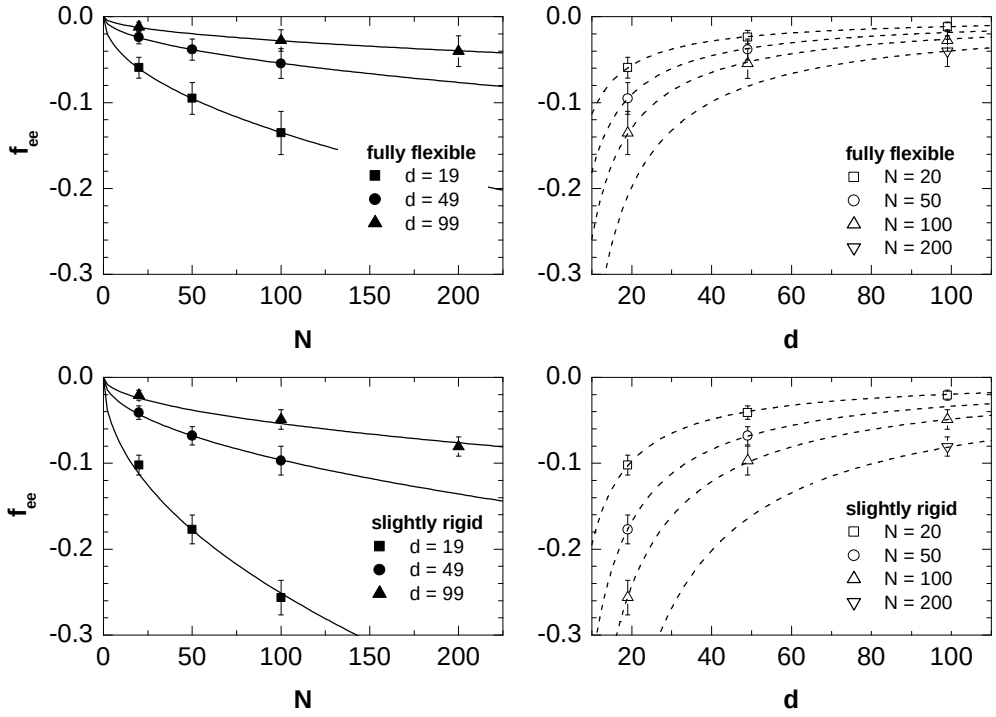

Figure 5.03 Orientation function of the end-to-end vectors as function of the number of elements per chain *N* and the film thickness *d* for fully flexible and slightly rigid chains. Simulation results (symbols) are compared to the predictions of Equation (5.04) (dashed lines) and Equation (5.05) (solid lines). Errors were estimated from standard deviation.

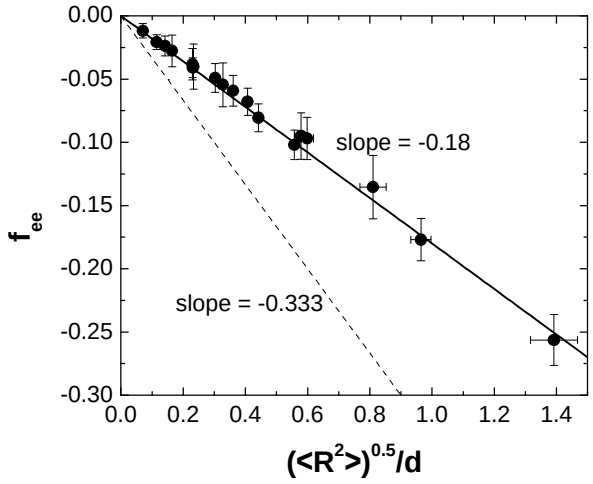

Figure 5.04 Orientation of the end-to-end vectors as function of the ratio between end-to-end distance and film thickness for all simulated systems. Simulation results (symbols) show a common behavior and are compared to the analytical model developed here (see Equation (5.09)) for two situations: when the density of centers of mass is assumed to be constant throughout the film (dashed) and when it is approximated as a step function following Equation (5.10) (solid).

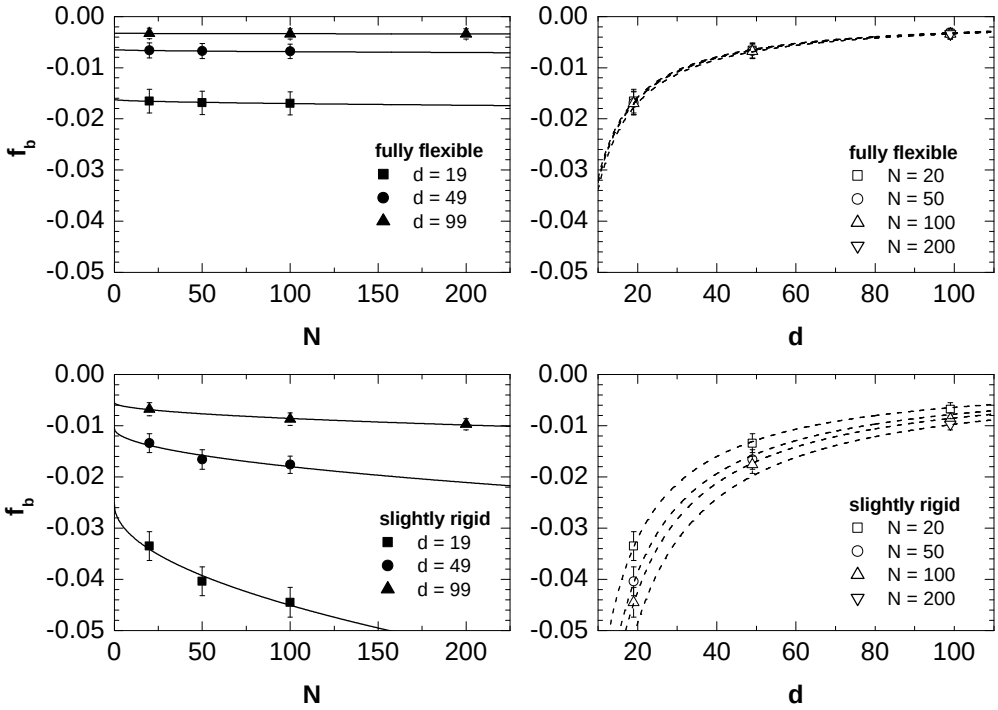

Figure 5.05 Orientation function of the coarse-grained bonds as function of the number of elements per chain *N* and the film thickness *d* for fully flexible and slightly rigid chains. Simulation results (symbols) are compared to the predictions of Equation (5.04) (dashed lines) and Equation (5.06) (solid lines). Errors were estimated from standard deviation.

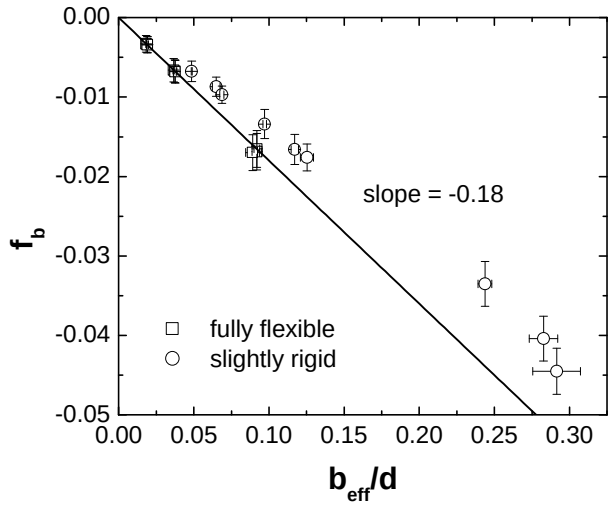

Figure 5.06 Orientation of the coarse-grained bonds as function of the ratio between Kuhn length and film thickness for all simulated systems. Simulation results (symbols) show a common behavior in analogy to Figure (5.04). Solid line represents a linear dependence with slope -0.18.

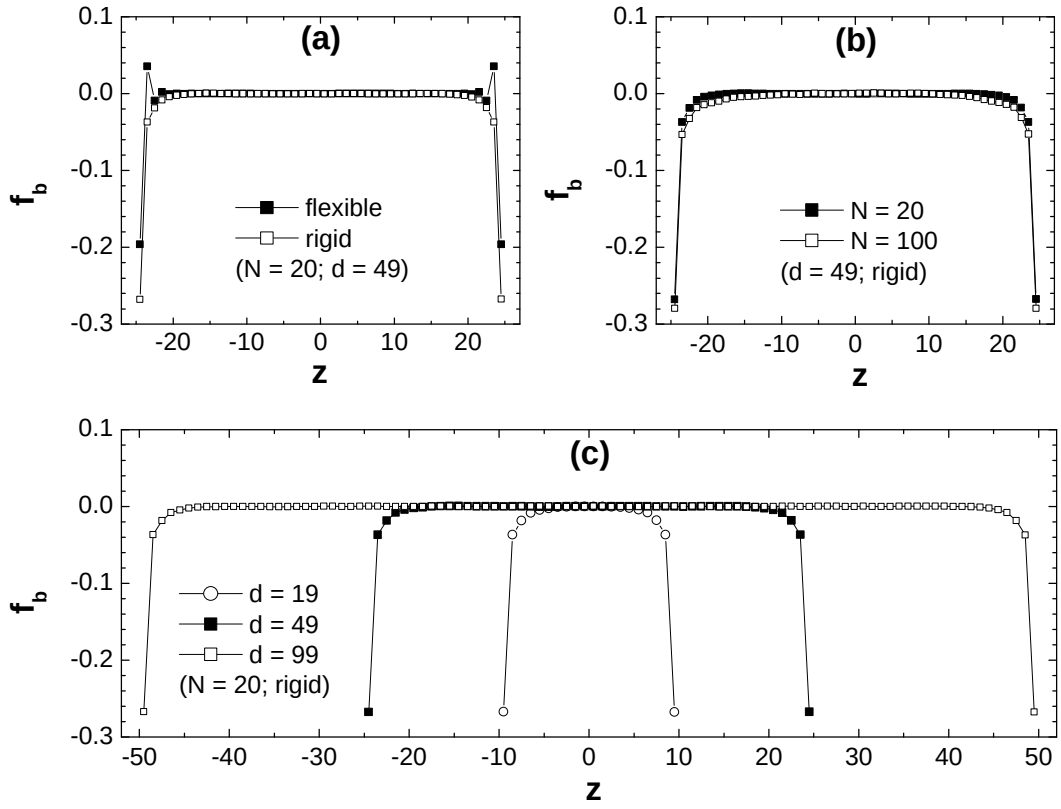

Figure 5.07 Orientation profiles of coarse-grained bonds in the direction perpendicular to the walls, showing the influence of parameters such as (a) rigidity, (b) number of elements in each chain or "molecular weight" and (c) film thickness.

and the space they have available. It may be considered as the main result of the simulations performed here. The question whether the tendency is followed or not by experiments will be discussed later.

The influence of "molecular weight" and thickness over the orientation of coarse-grained bonds f_b was also investigated. Figure (5.05) reveals for f_b the same qualitative tendencies as previously observed for f_{ee}. In analogy to the orientation of the end-to-end vector, the orientation of single bonds may be generalized as depending linearly on the ratio between the Kuhn length and the film thickness, as shown in Figure (5.06). Furthermore, a straight line with the same slope as in Figure (5.04) falls very close to the simulation results for fully flexible chains in Figure (5.06), giving one more indication of the generality of the size effect. In the case of rigid chains, the simulation results slightly deviate from the straight line. Possibly a better agreement would be obtained if the orientation of Kuhn segments was plotted instead of the orientation of individual coarse-grained bonds.

So far, the orientation has been shown as the average over the whole film. Additional information is obtained by dividing the film in layers parallel to the surface and plotting the value of average single bond orientation in these layers as function of distance to the walls. Figure (5.07) shows that the orientation is strong near to the walls but becomes random a few molecular layers away. Varying the thickness does not change the orientation profile close to the surface but merely increases the thickness of the region in the middle of the film where bonds are randomly oriented. Similar trends have been already observed in previous reports [Kumar'88, Kumar'90, Baschnagel'95, Vacatello'02, Picu'03] and demonstrate the existence of a so-called *skin effect*. This means that simulated polymer films may be interpreted as being constituted by a randomly oriented polymer matrix, covered by a skin of oriented polymer close to the boundaries.

5.3.3. Analytical Model

The proposition that chain orientation in the systems simulated here is solely determined by the ratio between the end-to-end vector and the film thickness will now be explored with more mathematical rigor. First, let us consider the thickness dependence of the orientation function. It was shown in Figure (5.07) that single bonds are oriented only in layers close to the walls, forming a skin of oriented bonds. Such skin effect is also observed by plotting the orientation of the end-to-end vectors as function of the distance between the wall and the centers of mass of the chains [Pakula'91], with the difference that the characteristic thickness of the skin is bigger because the end-to-end vector is also bigger than single bonds. For films thicker than the characteristic size of these skin layers, the average orientation function of a given vector throughout the whole volume of the film may be expressed as function of the film thickness d by means of a weighted average:

$$f = \frac{f^{or} d^{or} + f^{ra} d^{ra}}{d}. \qquad (5.03)$$

Here, f^{or} represents the average vector orientation inside the ordered skin and d^{or} the thickness of such skin. The parameters f^{ra} and d^{ra} are analogous quantities in the internal region where vectors are randomly oriented. If the molecular weight is kept constant, the orientation profile close to the walls does not vary with thickness. This

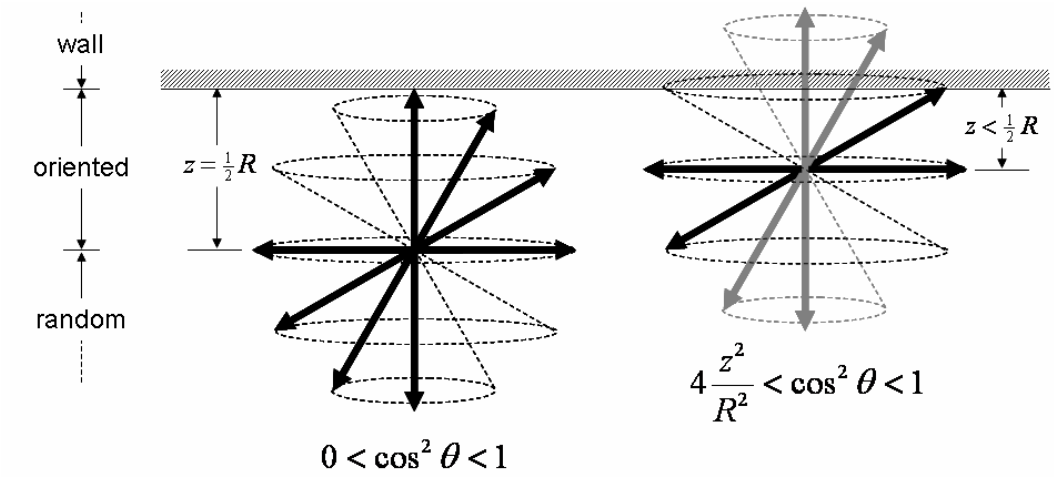

Figure 5.08 Scheme of the possible orientation that the end-to-end vector (black arrows) can assume depending on its distance from the wall (shaded area). Grey arrows denote forbidden conformations due to volume exclusion between polymer chains and the wall. Dashed lines indicate the degeneracy of each angle in the three-dimensional space.

means that the average orientation in the skin and consequently the term $f^{or}d^{or}$ may be assumed to be constant. Moreover, the term $f^{ra}d^{ra}$ vanishes because the orientation function for random systems equals zero. Considering these arguments, Equation (5.03) leads to:

$$f \propto d^{-1}. \tag{5.04}$$

Indeed, Figures (5.03) to (5.06) show that this expression describes satisfactorily well the thickness dependence of orientation in the range of molecular weights and chain rigidities investigated in simulations. It is important to point out, however, that Equation (5.04) is not an universal function. It describes a regime in which $d > d^{or}$, i.e., a regime in which the layers of oriented chains located at both surfaces of the film do not overlap with each other. It may fail, for instance, to describe systems with very small thickness or high molecular weight.

Equation (5.03) may be also worked out to explain the dependence of the end-to-end vector orientation on the number of elements in the chains. First, it is necessary to recall that, in the case of the end-to-end vector, orientation comes out from a size exclusion effect, as represented in Figure (5.08). If the film thickness does not change, the term $f^{or}d^{-1}$ in Equation (5.03) is kept constant. However, d^{or} may be assumed to

roughly correspond to the length of the end-to-end vector, which is proportional to $N^{0.5}$ for Gaussian chains (see Section (2.2.1)). This leads to:

$$f_{ee} \propto \sqrt{N} \,. \tag{5.05}$$

In the range of N investigated here, Equation (5.05) describes well the molecular weight dependence of the end-to-end vector orientation, as evidenced in Figure (5.03).

In the case of coarse-grained bonds, however, a different behavior is observed. Figure (5.05) shows that the orientation of coarse grained bonds practically does not change as function of molecular weight for the fully flexible chains. This possibly happens because the increase of molecular weight does not change the bond length. Furthermore, the length of these bonds is almost equal to the Kuhn length, meaning that they are statistically independent from each other. Hence, the orientation should depend to a good approximation only on the ratio between the bond length and the thickness, i.e. it is independent of molecular weight. Molecular weight dependence of the bond orientation is observed only for the cases where rigidity is implemented, i.e. when an orientation correlation exists between different single bonds. We found empirically that the dependence of bond orientation on molecular weight in Figure (5.05) is better described by an equation of the form:

$$f_b = a_1 \sqrt{N} + a_2 \,, \tag{5.06}$$

where a_1 and a_2 are fitting parameters (a_1 tending to zero for the case of fully flexible chains). This is again not an universal function, i.e. its validity is restricted to an intermediate range of molecular weights. It may fail at very high molecular weights, as well as at low molecular weights, where the chain contour length is comparable to the Kuhn length.

Equations (5.04), (5.05) and (5.06) will be later applied to verify in which extend the picture of a film being constituted by an internal layer of randomly oriented chains and covered by oriented skins agrees with experimental reality. For now, let us return to Figure (5.04) and investigate in more detail the dependence of the end-to-end vector orientation on the ratio between the end-to-end distance and the film thickness. Figure (5.08) brings a scheme of possible orientations that the end-to-

end vector may assume depending on its distance from the wall. To a first approximation, it can be assumed that different vectors do not to interfere with each other, only with the wall. Hence, if the center of the vector is at a distance longer than $\frac{1}{2}R$ from the wall, all orientations are possible and the average orientation of vectors at this layer will be random. At smaller distances, some orientations are forbidden, namely those that correspond to smaller angles in relation to the reference vector normal to the surface. This means that the skin of oriented chains starts at the surface and extends itself until the distance of $\frac{1}{2}R$. The factor $f^{or}d^{or}$ in Equation (5.03) is then given by the summation of the orientation function across all layers that compose the oriented skin. In the continuum limit, assuming that R does not depend on the distance from the wall [Pakula'91], we propose that:

$$f_{ee}^{or}d^{or} = 2\int_0^{R/2}\left(\frac{3}{2}\left\langle\cos^2 q\right\rangle_z - \frac{1}{2}\right)r'(z)dz, \qquad (5.07)$$

where $r'(z)$ represents the normalized density of vector centers as function of z, the distance to the wall. In a first moment, r' will be assumed to be equal to 1 and not to vary with z. The average angle in each layer is given by:

$$\left\langle\cos^2 q\right\rangle_z = \frac{\int_{q_{\min}}^{p/2}\sin q\cos^2 q\ dq}{\int_{q_{\min}}^{p/2}\sin q\ dq} = \frac{4}{3}\frac{z^2}{R^2}, \qquad (5.08)$$

where q_{min} is the minimum angle allowed by the confinement effect (in relation to the vector normal to the surface). The weighting factor sin q accounts for the degeneracy of each angle in the three-dimensional space. Substituting Equation (5.07) in (5.03), we find that:

$$f_{ee} = a\frac{R}{d}, \qquad (5.09)$$

where a is a constant equal to $-\frac{1}{3}$. Figure (5.04) shows that this expression does not provide a good description of the simulation results. The reason lies in the assumption

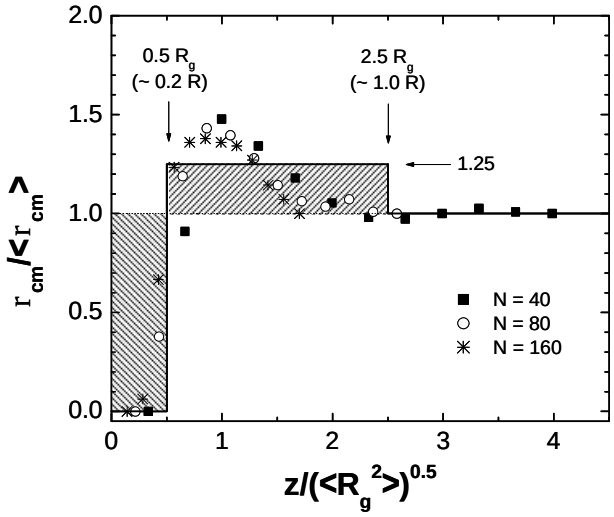

Figure 5.09 Density of centers of mass of polymer chains as function of their distance from the wall (normalized to the radius of gyration). Symbols are simulation results extracted from a previous work of Pakula [Pakula'91]. Solid line represents the step function given by Equation (5.10). The shaded rectangles have the same area so that the average normalized density throughout the film equals 1.

that the density of vector centers is independent from the distance to the wall. To illustrate this, Figure (5.09) summarizes results of a previous work [Pakula'91] with the same method and systems similar to those presented here. In this work, it was shown that the centers of mass of polymer chains are almost completely depleted from the first layers close to the walls. Then, the center of mass density increases, reaches a maximum and then decreases to its average value away from the wall. Taking the density of centers of mass as equivalent to the density of vector centers and approximating its behavior as a step function, we have that:

$$\begin{aligned} r'(z) \approx r_{CM}(z)/\langle r_{CM} \rangle &= 0, && z < \tfrac{1}{5}R \\ &= 1.25, && \tfrac{1}{5}R \le z < R\,. \\ &= 1, && z \ge R \end{aligned} \qquad (5.10)$$

Note that Equation (5.10) respects the necessary condition that the integration of $r'(z)$ over the entire thickness equals 1. Taking into account the density variation, the parameter a in Equation (5.09) assumes the new value of approximately –0.18 and provides a much better agreement with simulation results, as observed in Figure

(5.04). The choice of the appropriate step function in Figure (5.09) is not unique and we estimate an error of approximately 10 % associated with a. The analytical model developed here seems to be very general since the slope $a = -0.18$ is also close to the data points related to the dependence of single bond orientation on the ratio between Kuhn length and film thickness, as shown in Figure (5.06).

5.4 Comparison with Experimental Data from the Literature

In the earliest investigations about chain orientation in polymer films, Prest *et al.* observed that the refractive index of thin polystyrene films produced by solvent-casting may show different values depending if light is polarized parallel or perpendicular to the surface of the film [Prest'79]. As discussed by the authors, the anisotropy of refractive indices, alternatively called birefringence, is an indirect way of addressing the orientation of polymer chains. The structural formula of polystyrene is given in Figure (5.01). The most important contribution to the refractive index of polystyrene chains comes from the phenyl rings lying practically perpendicular to the polymer backbone. These phenyl rings have an intrinsic anisotropy in the sense that the polarizability parallel to the plane of the ring is higher than perpendicular to it. When polymer chains are preferably aligned parallel to the film surface, phenyl rings are mostly oriented perpendicular to it, causing the refractive index of in-plane polarized light to be lower than that of the out-of-plane polarized light. The birefringence is given by the difference between both refractive indices n:

$$\Delta n = n_{\mathrm{TE}} - n_{\mathrm{TM}}\,, \tag{5.11}$$

where n_{TE} is the in-plane refractive index, i.e., the refractive index of light whose electric vector is polarized parallel to the film surface. Analogously, n_{TM} is the out-of-plane refractive index, i.e., the refractive index of light whose magnetic vector is polarized parallel to the film surface. The stronger the chain orientation parallel to the surface, the higher the absolute value of birefringence. Figure (5.10) summarizes the main findings of the earliest works [Prest'80]. It shows that the absolute value of birefringence (or equivalently chain orientation) increases with decreasing thickness

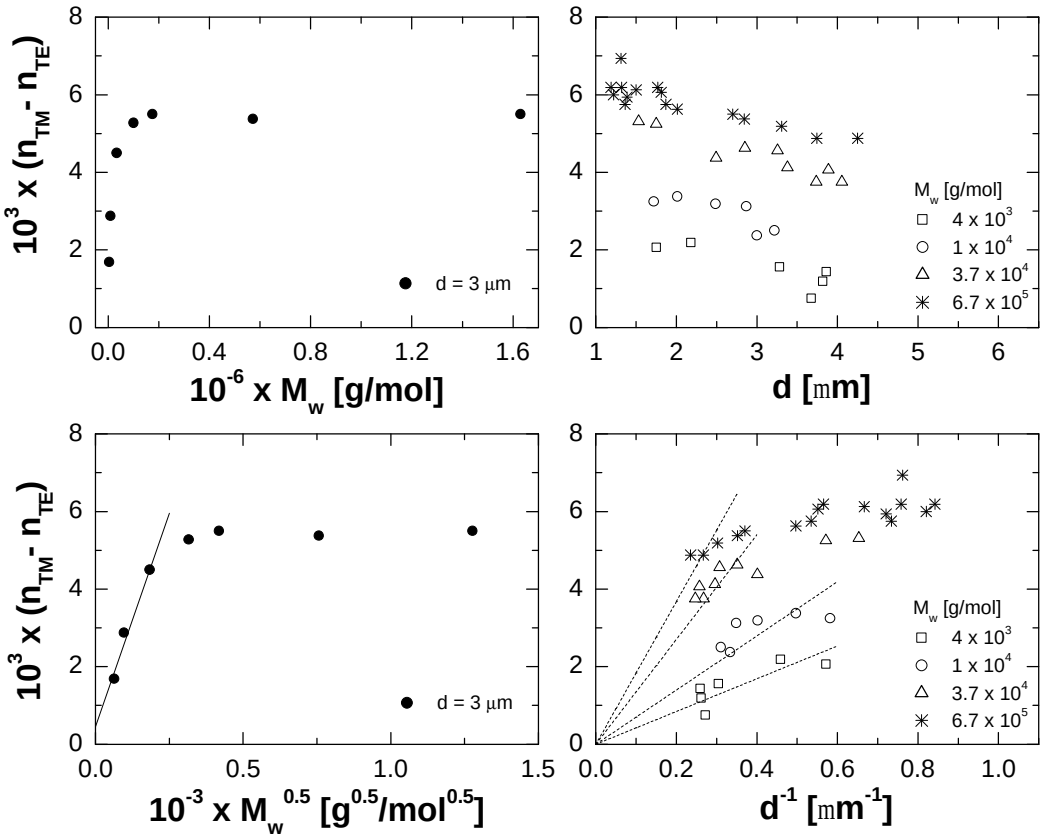

Figure 5.10 Birefringence of solvent-cast polystyrene films as function of the weight average molecular weight and the film thickness. Upper plots bring experimental results as extracted from Prest *et al.* [Prest'80]. Lower plots are the same data worked out to compare experimental results with simulation predictions about the linear dependence of orientation on the square root of molecular weight (solid lines) and the inverse of thickness (dashed lines). Note that the weight average molecular weight was used as a parameter because the values of number average molecular weight were not available.

or increasing molecular weight. For the materials with lowest molecular weight, the thickness dependence agrees with the predictions from Equation (5.04). For low molecular weight polystyrene, the molecular weight dependence also seems to follow Equation (5.06). Birefringence is correlated with the orientation of single segments (each one comprising a phenyl ring in the case of polystyrene). In respect to the molecular weight dependence of segmental orientation, it seems that the simulation results that are qualitatively closer to the experimental behavior of polystyrene are those related to slightly rigid chains. At a first moment, it may appear as a paradox because polystyrene is known as a flexible polymer. However, it is necessary to recall that rigidity is not a categorical definition. Rigidity may be implemented in

simulations but simulated chains may be still far from what is called a rigid chain in experiments. The Kuhn length of polystyrene chains is on the order of 2 nm and comprises a few single monomers [Eisenberg'90]. Similarly, chains that were called as "slightly rigid" in simulations have a Kuhn length comprising approximately 3 or 4 single bonds. In view of these arguments, it is not strange that polystyrene apparently follows the behavior predicted by simulations in which a slight rigidity was implemented.

It is also possible to observe indications of a skin effect in experiments, without entering in details about the extent of orientation in these skin layers as compared to simulations. In Figure (5.10), the existence of a skin effect is mainly corroborated by the linear dependence of birefringence on d^{-1} for low molecular weight polystyrene. For higher molecular weight polystyrene, the absence of such behavior may be explained by the overlap of the oriented skins in the film-air and film-substrate interfaces, meaning that the regime in which $d > d^{or}$ is no longer obeyed.

Considering the previous arguments, simulations are apparently in non-rigorous qualitative agreement with experiments. However, additional effects observed by Prest *et al.* suggest that experiments are far more complicated than simulations and that the simple picture of an orientation induced by simple geometrical confinement is oversimplified. For instance, the process of drying of a polymer solution may lead to the formation of a solid film in which chains are frozen in a non-equilibrium conformation. In fact, if high molecular weight polystyrene films are prepared at higher temperatures close to the glass transition temperature, they are less birefringent as compared to films produced at room temperature [Prest'80].

Regarding the influence of polymer rigidity on chain orientation, the most systematic experimental investigations were done with polyimides [Russel'83, Boese'92, Lin'93, Lin'94, Ree'94, Coburn'94, Li'97, Li'99, Lee'03]. In contrast to polystyrene, the refractive index of polyimides is mainly determined by the polarizability along the backbone, therefore films with chains preferably oriented parallel to the surface exhibit an in-plane refractive index bigger than the out-of-plane. Figure (5.11) shows the variation of birefringence as function of thickness for several polyimides differing in their chain rigidity (see also Figure (5.01) for the chemical structures). In the investigated thickness range, the birefringence of the most flexible polyimide continuously decreases as thickness increases. However, for rigid polyimides, the birefringence does not vary up to a given characteristic thickness, and

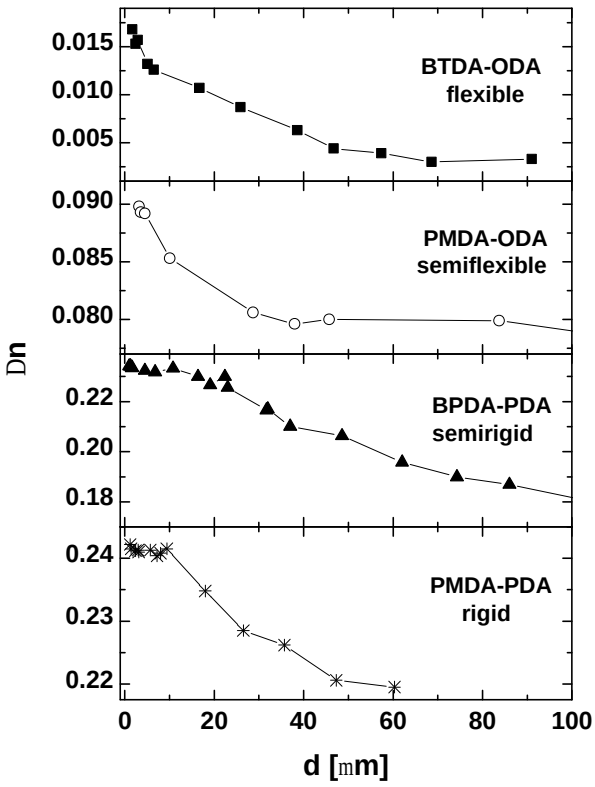

Figure 5.11 Birefringence as function of film thickness for several polyimides differing in their chain rigidity (see Figure (5.01) for the chemical structures). Experimental results were extracted from the work of Ree *et al.* [Ree'94].

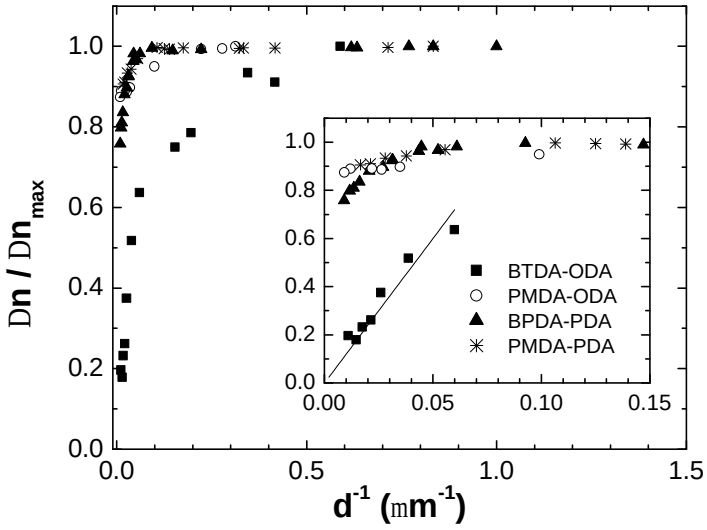

Figure 5.12 Birefringence as function of the inverse of film thickness for several polyimides (see Figure (5.01)). Experimental results were extracted from the work of Ree *et al.* [Ree'94]. The inset shows that, at larger thicknesses, only the most flexible polyimide follows the prediction of Equation (5.04).

only then starts to decrease. In fact, applying the same treatment as for polystyrene, Figure (5.12) suggests the existence of a skin effect for the flexible polyimide. The fact that the birefringence of rigid polyimides does not follow the dependence on d^{-1} suggests that the skin layers cover the entire thickness of the film, i.e. the regime in which $d > d^{or}$ was probably not accessed experimentally. A high degree of orientation remains even at distances from the surface which are far bigger than usual chain dimensions, in contrast to the behavior predicted by simulations. Evidence for the existence of skin layers reaching several micrometers has been provided by several authors [Lin'93, Lin'94, Ree'94, Coburn'94, Diao'05]. However, it is not straightforward to determine what is the major reason for chain orientation because the process of film preparation is complex and involves not only spin-coating of a precursor but also thermal treatment steps to convert it to a polyimide. It was observed that spin-coated films of the precursor polyamic acid have much lower birefringence and dichroic ratio in comparison with the same films after imidization. One possible reason is that polyamic acid films produced from solutions with *N*-methyl-2-pyrrolidone as solvent are still wet after spin-coating, meaning that possible orientation effects induced by the fast receding of the evaporating surface during spin-coating can relax to the equilibrium value [Ree'94, Hasegawa'96]. In this sense, the thermal treatment leading to imidization of the precursor seems to be crucial for the orientation effect. In addition to that, it was pointed out that stresses probably arise from the mismatch in the coefficient of thermal expansion of the substrate and the film [Coburn'94]. If they expand by different amounts, the film is stretched and this is known to induce polymer chain orientation [Hasegawa'96]. In fact, the hypothesis of an orientation induced by mechanical stress is supported by the observation that free-standing films of polyimides have a lower birefringence as compared with films attached to a substrate [Coburn'94, Hasegawa'96]. Nevertheless, Hasegawa *et al.* concluded that these stresses alone would not suffice to induce the strong orientation effects observed. They proposed a mechanism for the spontaneous in-plane orientation during thermal imidization in which liquid-crystal-like and highly oriented regions are formed in the polyimide films during cure. Simultaneously, the apparent stretching that results from the mismatch of the coefficients of thermal expansion promotes further orientation. This mechanism is closely associated with the cooperative effect according to which neighboring chains enhance the orientation of each other during the thermal treatment. The influence of interchain interactions

leading to the formation of liquid-crystalline domains was tested by means of comparative experiments involving polyimide chains with bulkier side groups [Hasegawa'96]. A theoretical approach to the analogous problem of formation of semi-crystalline order in networks of semirigid chains in the swollen state has been given by Yang *et al.* [Yang'95].

In view of the importance that rigidity and interchain interactions seem to assume in determining chain orientation, we decided to perform our own experiments with π-conjugated polymers. The next section is dedicated to the presentation of the experimental results and their discussion. We have chosen materials that can be easily and directly deposited on a substrate without an intensive thermal treatment as was the case for polyimides.

5.5 Own Experiments with Conjugated Polymers

5.5.1. Materials and Experimental Methods

The π-conjugated polymers MEH-PPV and polyfluorene (see Figure (5.01) for the chemical structures) were selected for the experimental investigations about chain orientation in thin films. The refractive index of these materials is strongly related to the polarizability of the delocalized electron cloud along the backbone. Moreover, they are extreme examples of rigidity and interchain interactions.

Thin films were prepared by spin-coating from freshly prepared and filtered (0.5 or 1 μm syringe filters) toluene solutions at ambient atmosphere under a laminar flow hood to minimize dust particles. Films were prepared at the surface of freshly cleaned fused silica substrates with typical size of 25 × 35 × 1 mm. Both the concentration by weight (1 – 7 %) and spinning speed (500 – 9000 rpm at quick acceleration) were varied to control the film thickness [Bornside'89, Spangler'90, Schmidt'01, Schubert'97, Bahtiar'04]. The films were placed subsequently in a vacuum oven at elevated temperatures ($T \approx 50\ ^0$C) for at least 6 hours to remove residual solvent. The thickness d and the average surface roughness of the films were measured with a Tencor Model P10 profilometer. In order to increase the precision, we have measured the film thickness for each film at several points (typically 8) in the region where the optical experiments were performed and used the average value of

these measurements. We have used films with thickness $d \approx 30 - 100$ nm for spectroscopic studies and thicker films (400 – 10 000 nm) for optical waveguides. To prepare the thickest films we applied the alternative technique of solvent casting or doctor blading using the Erichsen model Coatmaster 509/MC-1 film drawing system. It worked in the following way: the film preparation frame was filled with a highly concentrated polymer solution and pulled along the surface of a fused silica substrate. Films prepared this way, however, showed some thickness variations. Therefore, their thickness was locally evaluated only by the prism coupling method described below.

The spectra of n_{TE} of the films were obtained by reflectometry at nearly perpendicular incidence. Transmission and reflection spectra of thin polymer films ($d \approx 30 - 100$ nm) on fused silica substrates were measured with a spectrophotometer (Perkin Elmer Model Lambda 900). The values of n_{TE} of the films were then calculated from these spectra at different wavelengths [Fitrilawati'02, Bahtiar'04, Koynov'06]. The refractive indices of MEH-PPV and polyfluorene waveguides (with thickness in the range of 400 nm – 10 μm) for both TE and TM polarization were determined by prism coupling [Bahtiar'04, Koynov'06]. This technique consists in placing the bottom of a prism with high refractive index on the surface of a film. A monochromatic laser beam traveling inside the prism reaches the bottom and suffers total internal reflection. Between the prism and the film there is a small air gap whose thickness can be controlled by pressing the prism on the film surface, in such a way that the evanescent field of the laser bridges the gap and tunnels energy into the film. Waveguide modes are excited in the film only at discrete incident angles which are characterized by minima in the intensity of reflected light. From these angles it is possible to calculate the refractive index of the film [Tien'70, Prest'79]. In the present investigations, the following lasers were used: HeNe (633 nm) and ps-Nd:YAG (1064 nm). We were able to excite both TE_0 and TE_1 (respectively TM_0 and TM_1) at the appropriate laser wavelength and used these two modes to calculate the refractive index and film thickness simultaneously. The obtained values of film thicknesses were in good agreement with those measured with step-profiler.

5.5.2. Experimental Results

Figure (5.13) shows n_{TE} and n_{TM} as a function of the weight average molecular weight M_w for MEH-PPV and polyfluorene. In the case of MEH-PPV, the same

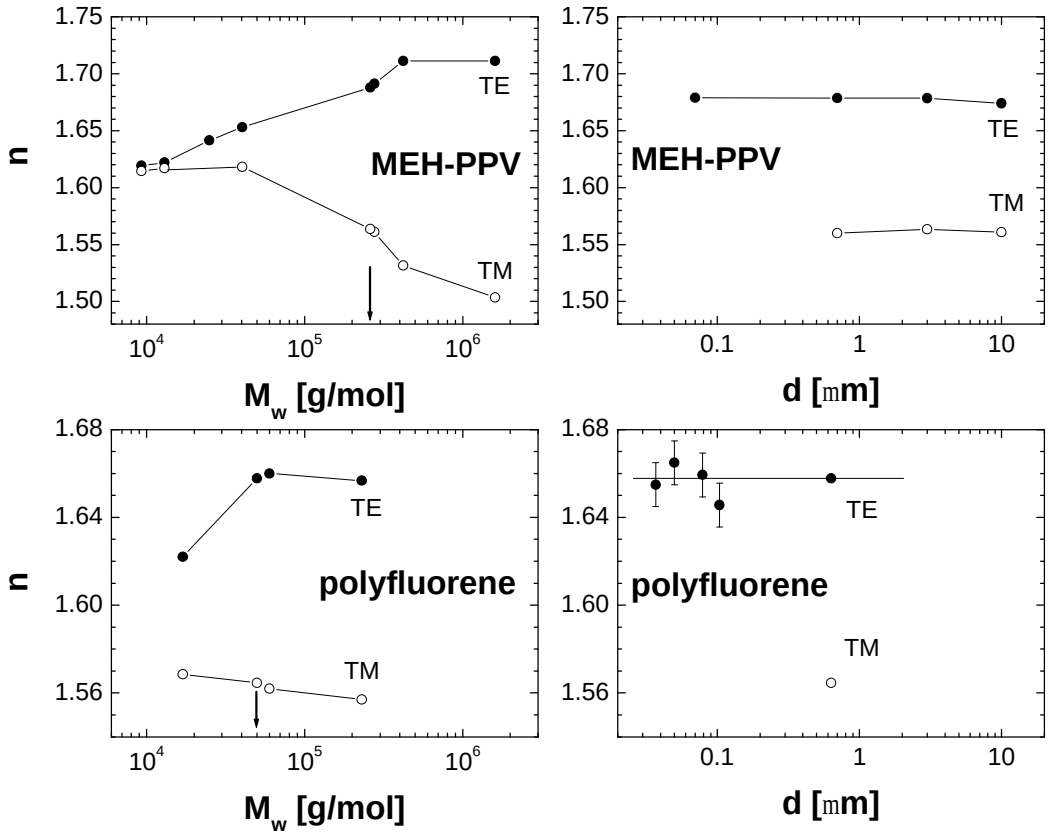

Figure 5.13 Molecular weight and thickness dependence of the refractive indices of thin films of MEH-PPV and polyfluorene (see Figure (5.01) for the chemical structures). Measurements at transverse electric (TE) and transverse magnetic (TM) polarizations are shown at a wavelength of 1064 nm for MEH-PPV and 633 nm for polyfluorene. The arrows in the graphs of molecular weight dependence indicate the molecular weight that was used in the investigations of thickness dependence. Films were prepared by spin-coating, with exception of MEH-PPV films with thickness of 3 and 10 μm, which were produced by doctor-blading.

behavior was observed for wavelengths of 1064 and 633 nm, although only the first case is presented here. At the highest molecular weights, the birefringence is very large and nearly independent of M_w. The values of n_{TE} and n_{TM} in this region are in good agreement with those reported recently for MEH-PPV [Tammer'02]. With the decrease of the molecular weight the birefringence is significantly reduced and at $M_w < 1.5 \times 10^4$ g/mol we observe for MEH-PPV a nearly complete loss of birefringence with a remaining $\Delta n < 0.005$ [Bahtiar'04, Koynov'04, Koynov'06]. The results displayed in Figure (5.13) show good reproducibility and a nearly continuous dependence of the birefringence on the molecular weight. This reflects the tendency

of chain orientation to increase as the molecular weight increases and agrees qualitatively with the behavior predicted by simulations. Taking into account that the values of n_{TE} and n_{TM} were measured in films with typical thicknesses $d \approx 400 - 800$ nm, it may look tempting to explain the increase of the in-plane orientation with M_w by confinement effects. To proceed with this analysis, it is necessary to estimate the average contour length of polymer chains, which is given by the length of the repeat unit multiplied by the average number of units as derived from the number average molecular weight M_n. Indeed, the MEH-PPV samples with lowest molecular weight have a contour length of about 10 – 20 nm, i.e. much smaller than d, while the contour length of samples with the highest M_w is larger than 250 nm, i.e. comparable to the film thickness. In order to explore this possibility of chain confinement effects, we studied the thickness dependence of the birefringence of a high molecular weight MEH-PPV **(**$M_w = 2.65 \times 10^5$ g/mol and $M_n = 8.71 \times 10^4$ g/mol**)**. The films were prepared by means of spin-coating (70 nm < d < 1 μm) and doctor-blading (d = 3 μm and 10 μm). Figure (5.13) shows n_{TE} and n_{TM} as a function of the film thickness. We like to elucidate the following points. First of all, we had to use the transmission-reflection spectroscopy to study the thinnest films (d < 100 nm) as they were too thin to support waveguide modes. We were able to measure only n_{TE} of these films because our reflectometry method does not yield n_{TM}. All other films were studied with waveguide prism coupling. Figure (5.13) shows that the MEH-PPV films made by spin-coating and doctor-blading have similar refractive indices. Therefore, their morphology must be similar. This observation indicates that the preferred alignment of the MEH-PPV chains should be related to the intrinsic properties of this material and to substrate-polymer interactions, and not to the particular film preparation method, at least for this particular range of film thicknesses and molecular weights. Furthermore, the birefringence does not decrease significantly with the increase of d up to a film thickness of 10 μm. This observation shows that chain confinement effects at reduced film thicknesses alone are not appropriate to explain the increased alignment of the high molecular weight MEH-PPV samples for the following reason: the average contour length derived from M_n is only approximately 250 nm and significantly smaller than the thickness range of 3 – 10 μm where we still observe nearly the same Δn as for ultrathin films [Koynov'06]. The same analysis can be extended to polyfluonene due to the similar behavior as compared to MEH-PPV.

It is also interesting to compare our results on the thickness dependence of Δn with reports of other groups. As we discussed in previous sections, earlier studies have shown that the birefringence of thin polymer films may depend on the film thickness, as for example in the case of polystyrene [Prest'80] or polythiophene [Zhokhavets'04]. Other polymers, however, as for instance polyimides, do not show a thickness dependence of Δn for films with thicknesses starting from 1 μm and up to a critical thickness in the order of several micrometers. The observed absence of a significant thickness dependence of Δn up to d = 10 μm in the high molecular weight MEH-PPV films is similar to the reported behavior of polyimides [Ree'94]. Therefore, we expect that a similar mechanism (i.e. the liquid crystalline behavior of the MEH-PPV chains due to their limited chain flexibility) is causing the alignment of the chain segments parallel to the layer plane as observed in thin films of several other polymers with significant chain rigidity [Boese'92, Hasegawa'96, Losurdo'03].

From the application point of view it is important to emphasize that the appropriate choice of the molecular weight of MEH-PPV and polyfluorene enables fine tuning of the refractive index of thin films and optical waveguides. Our results are useful for the selection procedure of the most appropriate type of polymer for specific applications in optoelectronics, for example: OLEDs should perform better with high M_w polymers because the enhanced in-plane alignment may facilitate the intermolecular charge transport and the light emission perpendicular to the layer plane [Friend'99].

5.6 Limitations of the Model and Final Considerations

The simulations of polymer chains confined between rigid walls show that the chain orientation is determined by a geometrical effect, i.e., chains have a preferential orientation parallel to the film due to size restrictions. Simulations agree qualitatively with the experimental behavior of low molecular weight polystyrene in the sense that in both cases the orientation increases with increasing molecular weight and decreasing thickness. Moreover, simulations provide a picture of the polymer film in which the chains are oriented only in the layers closer to the surface, whereas chains in the interior of the film remain essentially randomly oriented. This may be

understood as a skin effect, which is characterized by the linear dependence of a given property related to chain orientation on the inverse of thickness. The occurrence of a skin effect seems to be the case in experiments with low molecular weight polystyrene since a dependence of birefringence on d^{-1} is observed.

However, it still does not prove that simulations strictly agree with the experimental behavior of polystyrene in a quantitative level. In fact, the observation that birefringence decreases if films are produced at higher temperatures suggests that the dynamics of solution evaporation and film preparation have a significant impact in addition to the size effect considered in our simulations [Prest'80]. Evidence has been provided in the literature for the importance of non-equilibrium effects related to the evaporation dynamics on the orientation of macromolecules. Morii *et al.* found that an evaporating DNA solution becomes more concentrated at the air-liquid interface in comparison to the interior. This was attributed to the high evaporation rate and fast receding of the interface, which is much faster than the translational diffusion of DNA molecules [Morii'04]. Increase of polymer concentration near a fast evaporating surface has been experimentally observed for a variety of cases [Pauchard'03, Schabel'03] and also theoretically predicted by analytical models [de Gennes'02] and molecular dynamics simulations [Tsige'04]. The concentration gradient may even lead to the formation of a glassy crust at the surface and it is possible that its movement downwards induces further orientation of chains in the solution below. The simulation of chain orientation induced by a fast interface movement is not easy using common Monte Carlo methods. The reason is that the translation of polymer chains in simulations traditionally proceeds in a diffusion-like fashion, and the time scale of such process is comparable to the time needed for orientational relaxation. We do not rule out the possibility to overcome the problem by implementing additional assumptions, but the crucial point would be then to prove their validity.

There are, however, several other possible improvements for the model developed here. First, it would be interesting to investigate the orientation phenomenon in a polydisperse ensemble of chains. Similar simulations were reported for a mixture of chains with two different lengths and it was concluded that the orientation of shorter chains increases because of the presence of longer ones [Doruker'02]. For a more detailed investigation, we suggest that molecular weight distributions similar to those found in experiments could be generated by the method of in-situ polymerization as described in Chapter 4. Another interesting improvement

would be to implement interactions between polymer segments and the walls, or even to compare the influence of rigid and soft walls.

The limitations of the model as it was developed here become clear by comparing simulations with the behavior of π-conjugated polymers like MEH-PPV and polyfluorene. A simple scaling analysis shows that even a qualitative agreement between simulations and experiments does not exist. In simulations, the orientation induced close to the walls decays as function of the distance and approaches the random limit at a distance comparable to the average end-to-end length of the polymer chains. However, in experiments with π-conjugated polymers, the apparent absence of thickness dependence of birefringence suggests that chains are highly and uniformly oriented across the whole film, at least in the thickness range investigated. This may be understood as the skin layers of oriented chains occupying the entire volume of the films, even at thicknesses that are supposed to be orders of magnitude higher than typical polymer chain dimensions. The huge orientational correlation between chains in the case of MEH-PPV, polyfluorene and rigid polyimides indicates the importance of interchain interactions, which are known to be very strong in these materials. It is even suggested that films of rigid polyimides exhibit liquid-crystalline domains with nematic order [Hasegawa'96]. In such cases it is more appropriate to focus on the orientation of chain aggregates instead of single chains. Aggregates are also known to be present in films of MEH-PPV [Koynov'06] and even in solutions of this material. High molecular weight MEH-PPVs may even exhibit nematic-like texture [Chen'02, Chen'04, Koynov'06]. In order to better describe the experimental reality, it would be necessary to implement strong interactions between chains in the simulations. It is however a difficult task in view of the small chain mobility and increasing computational costs associated with that.

6

Patterning of Polymer Film Surfaces by Droplet Deposition

6.1 Experimental Background

Surface micro and nanostructuring is a field of interest both to basic research and industrial applications. The most appealing surface patterning techniques are those which are experimentally simple and enable the control of pattern shape. It was recently shown that it is possible to create microwells by bringing solvent drops at the surface of a soluble polymer substrate [Sequeira'03, Gonuguntla'04, Bonaccurso'05, Sequeira'06]. The process is analogous to the formation of ringlike deposits when, for example, a coffee drop evaporates and leaves a ring shaped stain of solid particles on the substrate [Parisse'96, Deegan'97, Parisse'97, Deegan'00, Ozawa'05]. The difference is that, in the first case, the solid left by the droplet was not initially dissolved in it, but is gradually dissolved from the substrate as the droplet evaporates. The effect is very general, i.e. it can be observed for a large variety of substances. As the droplet evaporates, the substrate material is removed from the center and deposited on the border of the droplet contact area. This process generates a microwell surrounded by a ringlike deposit, as shown in Figure (6.01). The microwell can be used for example as a chemical microreactor or as a mask for the molding of microlenses [Sequeira'03, Bonaccurso'05, Sequeira'06]. Microwells produced by inkjet printing have been also applied in the generation of the so called *via-hole interconnections* in organic thin film transistors [Kawase'01].

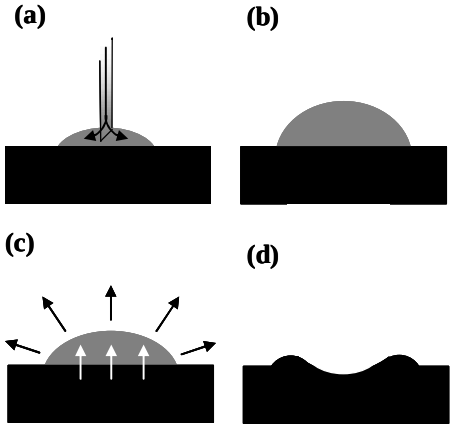

Figure 6.01 Different stages of microwell and ringlike deposit formation. (a) Solvent is placed on a soluble surface with a syringe. (b) A droplet is formed. (c) Substrate is slowly dissolved (white arrows) while the droplet evaporates (black arrows). (d) A microstructure is left on the surface.

A phenomenological model to explain the formation of ringlike deposits is already available in the literature [Deegan'97, Deegan'00, Sequeira'03, Sequeira'06]. In this model, the contact area between droplet and substrate is considered to be pinned. As the liquid evaporates, an outward liquid flux is considered as necessary to compensate the amount of liquid that evaporated from the border, as represented in Figure (6.02). This flux is responsible for the transportation of dissolved material to the border, where it is concentrated and finally precipitates. Although the model accounts very well for microwell and ringlike deposit formation, it cannot clarify the role of molecular interactions involved in this process. Furthermore, it is still not clear if the pinning of the contact area is really a requirement for the ring formation or if it is instead a consequence of the ring formation. These questions are also very difficult to be clarified experimentally.

6.2 Methodology

The aim of this chapter is to investigate microwell and ringlike deposit formation with a molecular approach. For that, we performed molecular simulations based on the CMA method described in Section (2.3). In this algorithm, intermolecular interactions are adjustable parameters. Liquid droplets on surfaces and in equilibrium with a vapor phase were generated according to the procedure exposed

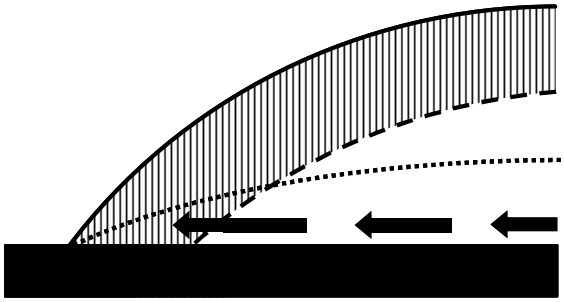

Figure 6.02 Evaporation dynamics of non-pinned (– – –) and pinned (• • •) droplets. Full line represents the initial shape of the droplet and the shaded area is the amount of solvent that evaporated. The arrows indicate the compensating liquid flux that keeps the contact line fixed when the droplet is pinned.

in Chapter 3, where it was demonstrated that droplets simulated with the CMA behave realistically. In a first moment, to simulate the general case of pattern formation, we considered the substrate as being constituted by simple molecules represented by single lattice sites. Later, we incorporated the method of simulating polymer chains in thin films adopted in Chapter 5 and considered explicitly a more complicated case: the one of a substrate constituted by monomers connected together and forming chains. We also explored the influence of chain orientation on the final pattern shape.

It turns out from our model that an appropriate choice of the interaction parameters is crucial for pattern formation [Cordeiro'05]. It is important to point out that simulated droplets are on the range of nanometers, a size scale still unexplored by experiments of microwell and ringlike deposit formation. Simulations may be compared with the experimental behavior only in the character of an approximation. Moreover, although the analysis developed here focuses mainly on the effect of molecular interactions, we do not rule out the importance of previously proposed models based on hydrodynamics [Deegan'97, Deegan'00, Kawase'01, Sequeira'03, Sequeira'06]. The present work is rather intended to clarify the role of additional variables, namely the intermolecular interactions, which may also contribute to the complexity of the phenomenon in question. This point is here discussed also in view of experimental observations that apparently contradict the predictions of the well established hydrodynamic model of Deegan *et al.* [Deegan'97, Deegan'00].

6.3 Molecular Modeling of Evaporating Droplets at Soluble Surfaces

6.3.1. Generation of Droplets at Surfaces and Simulation of Evaporation

Liquid droplets sitting at solid surfaces and in equilibrium with vapor were simulated using the CMA method, as described in Chapter 3. First results of these investigations have been published recently [Cordeiro'05]. In the model presented here, an ensemble of beads is created on a fcc three-dimensional lattice that serves as a coordination skeleton. Each lattice site is occupied by a single bead representing for instance a molecular element or a molecular aggregate. The program simulates the collective motion of beads along closed random loops. As done in Chapter 3, beads on the lattice are regarded as having three types of identity. They are labeled to represent either solvent particles (SO), substrate particles (SU), or vacuum (VA). Although different elements can exchange place with each other, their identity is conserved. Still following Chapter 3, the repulsive energy of interaction between two neighboring elements is considered as zero if they have the same identity and as a finite and positive number if they have different identity. Before each movement, the probability of acceptance of a bead in the next position is calculated according to Equations (2.23) and (3.01).

The initial system configuration was a cubic droplet of pure solvent placed upon a layer of substrate material and surrounded by vacuum. The simulation then started and proceeded until the cubic droplet had relaxed to a droplet with the shape of a spherical cap. During the relaxation of the cubic droplet, motion of substrate elements was forbidden to avoid their intermixing with solvent or vacuum. However, substrate elements on the surface could still interact with solvent or vacuum and the energies of interaction determined the substrate wettability. Periodic boundary conditions were applied only in the directions parallel to the substrate surface.

After the droplet had relaxed, the simulation of the evaporation process started. Droplet evaporation was accomplished by removal of vapor. If a solvent element mixes with vacuum and all its neighbors are vacuum beads, then the program automatically transforms it into a vacuum bead. At this stage, substrate elements were allowed to move and to mix with the solvent to account for substrate solubility. One condition was that the intermixing between substrate and vacuum beads was forbidden. This was made for two reasons. First, to account for the strong intermolecular bonds that should exist in solid structures and prevent the appearance

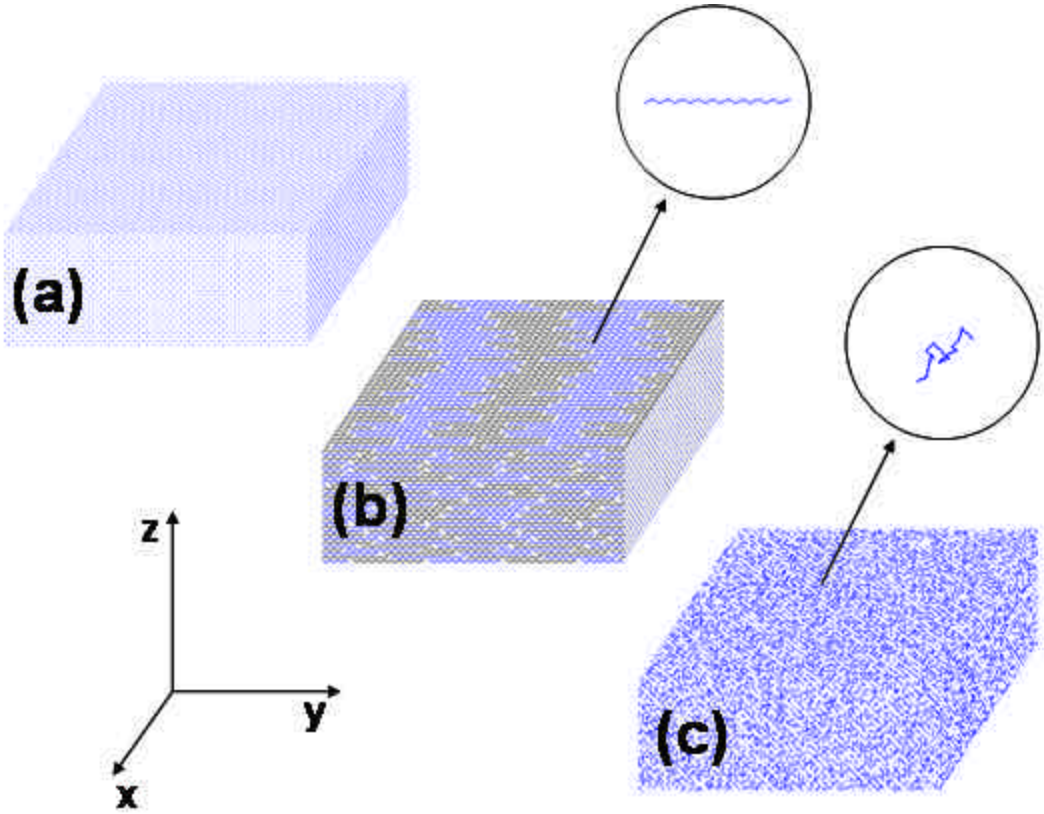

Figure 6.03 Three dimensional view of different substrates, in whose (*x*,*y*) surface droplets were placed for the generation of patterns. (a) General case of a substrate constituted by simple molecules represented by blue dots. (b) Substrate constituted by polymer chains with uniaxial orientation parallel to the surface (chains were pictured in the colors black and blue to make the nematic-like ordering more apparent). The position of the centers of mass was randomly determined for different simulations. (c) Substrate constituted by polymer chains (blue) which were allowed to relax to their equilibrium orientation before swelling started. Circles bring pictures of single polymer chains in an enlarged scale.

of “vacuum holes” inside them. The second reason is that the incorporation of vacuum within the solid structure would change the nature of the substrate. This would add a new variable to the problem if one wants to compare these experiments with those not involving substrate swelling.

In the following sections we discuss different cases based on the simulation method described here. In the first case, the more general one, the substrate was regarded as being constituted by simple molecular elements represented by single lattice sites, as shown in Figure (6.03). Although no motion should occur inside the solid structure, substrate elements were allowed to exchange their position with other

substrate beads even in the solid phase. This assumption was made to simplify the algorithm and is not unrealistic, since the identity of the elements does not change when they exchange place with each other. In the second case, molecular elements in the substrate were connected together forming polymer chains. To account for the solid character of the polymer film, only chain elements surrounded by at least one solvent particle were allowed to move and to rearrange. Two kinds of chain configuration were investigated. First, chains were placed on the substrate with perfect uniaxial orientation parallel to the surface. The positions of the centers of mass were randomly chosen so that chains were ordered in a nematic-like fashion, as shown in Figure (6.03). This was used as the initial substrate configuration as the evaporation of the droplet started, together with substrate swelling. An ensemble of chains with such configuration is far away from the equilibrium configuration. Chains exhibit an induced orientation that is equivalent to the chain orientation in experiments in which a polymer film is stretched or extruded, causing its chains to align parallel to the direction of the applied force. In a second investigation, the nematic order was allowed to relax so that swelling started on a substrate in which chains were previously allowed to reach their equilibrium configuration (see Figure (6.03)). Of course, there is still a residual orientation resulting from confinement, as shown in Chapter 5, where the self-induced orientation in thin polymer films was studied.

6.3.2. General Case of Pattern Formation

It turns out from the simulations that the choice of the interaction energies is crucial for microwell and ring formation. The best condition at $kT = 3.0$ (see Chapter 3) was to consider the interactions SO−VA, SO−SU, and SU−VA as 1, 0.8 and 0.8 respectively [Cordeiro'05]. Using these parameters, droplets were produced by means of relaxation of a cubic droplet. At this stage, substrate swelling was forbidden. The droplet formed this way was used in two kinds of simulations. In the first, the substrate movement was kept forbidden but evaporation proceeded. In the second, substrate beads were allowed to move during evaporation and a pattern in the surface was formed.

The formation of the ringlike deposit can be qualitatively deduced from the interaction values. Since the SO−SU interaction is relatively large, it is expected that the substrate will dissolve very slowly. Once they have been swollen, substrate beads

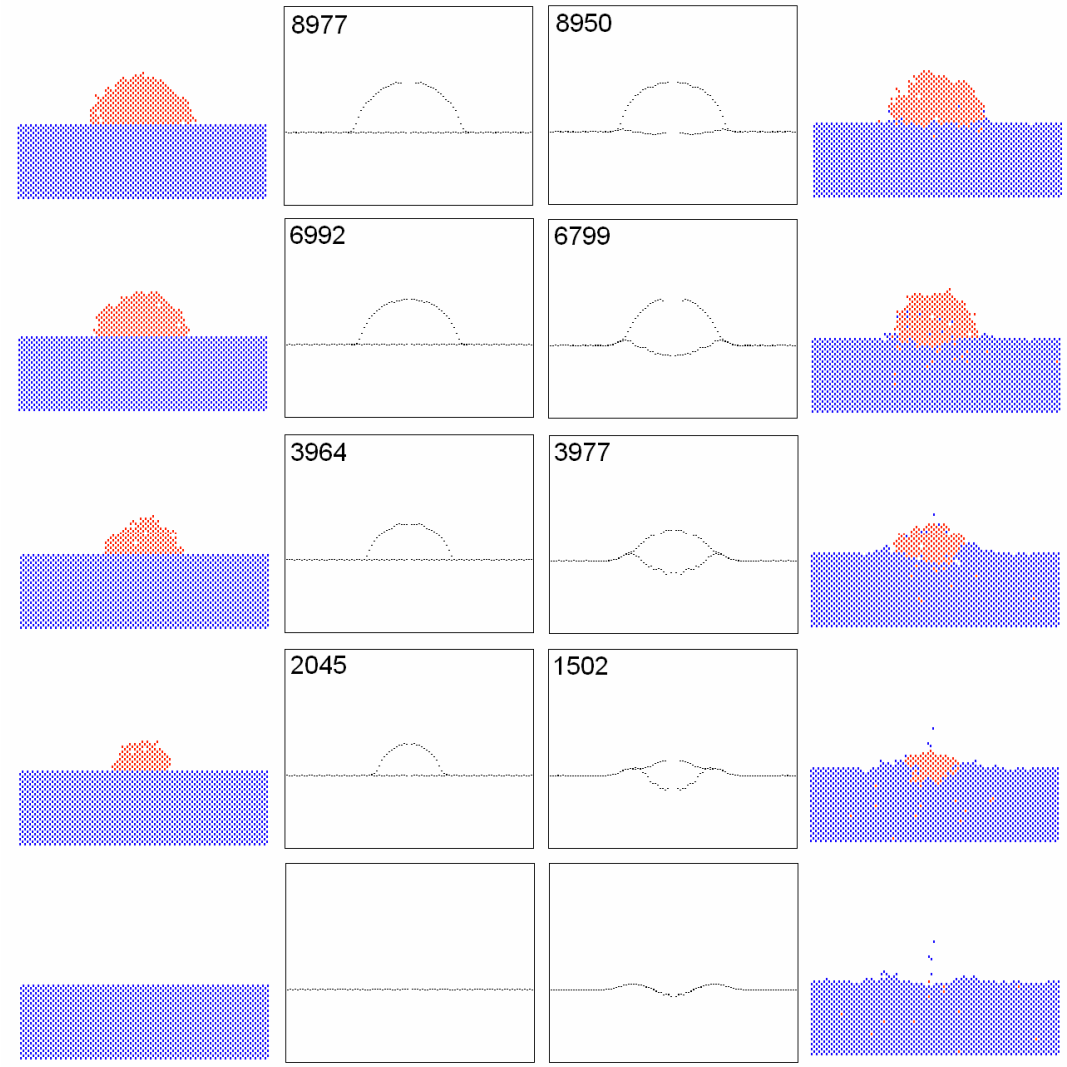

Figure 6.04 Snapshots of evaporating droplets in nonsoluble (left) and soluble (right) substrates. The white boxes show the radial averages of the snapshots (the droplet center of mass was considered the center of symmetry). The number in the top of each box is the number of solvent beads remaining within the droplet.

will migrate to the boundary between solvent and vacuum. This happens because the repulsive interaction between a swollen substrate and vacuum is lower than the SO–VA interaction. The shape of the substrate surface would not change if solvent was not present because exchanges between substrate and vacuum are forbidden due to the solid structure. A solvent is necessary to swell this solid and a structured surface is generated to minimize the energy of the system.

Figure (6.04) compares snapshots of the simulated system in the case of simple evaporation and substrate swelling together with evaporation [Cordeiro'05]. In

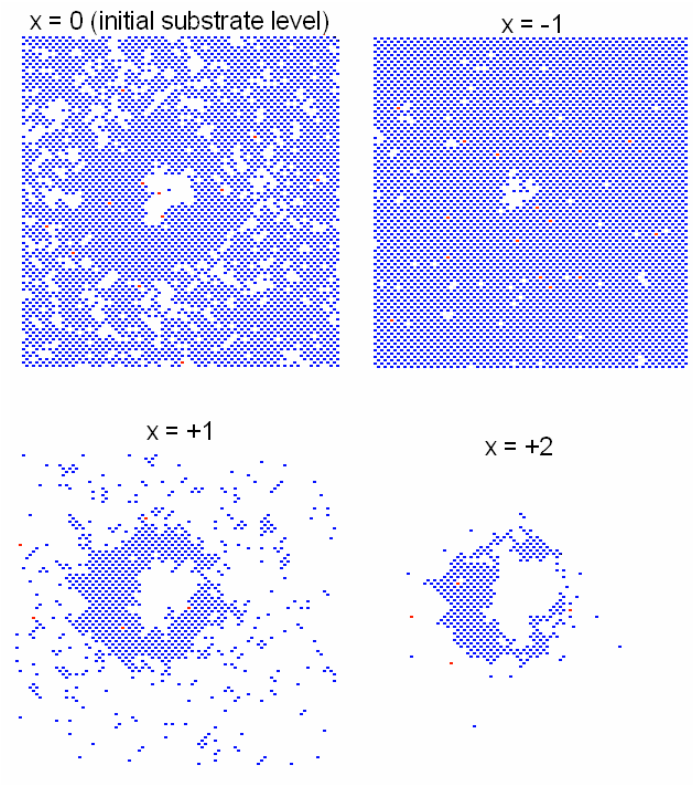

Figure 6.05 Snapshots of planes parallel to the surface of the substrate at several heights (*x*) showing a well surrounded by a ringlike deposit in the end of the evaporation process. Blue dots represent substrate particles.

the latter situation, the substrate is slowly dissolved by the solvent, and at the same time some solvent beads penetrate the solid structure of the substrate. The swollen substrate migrates to the border of the droplet, where it forms a deposit. The result of this process is the formation of a well surrounded by a ring at the surface, as shown in Figure (6.05). At the end of the simulation, it can be seen that some substrate beads remain suspended in the vacuum forming a kind of “substrate gas” (see Figure (6.04)). Clearly, this is not realistic. This effect occurs because, for the sake of algorithmical simplicity, substrate beads are not allowed to exchange place with vacuum. Thus, as the solvent evaporates, some dissolved substrate beads are left away in vacuum, where they remain immobile. However, the quantity of substrate gas corresponds only to 20 % of the volume required to fill the hole and therefore does not disprove our results [Cordeiro’05]. One could eliminate this effect by adding gravity in the model or by implementing connectivity between substrate elements, as will be shown in the next section.

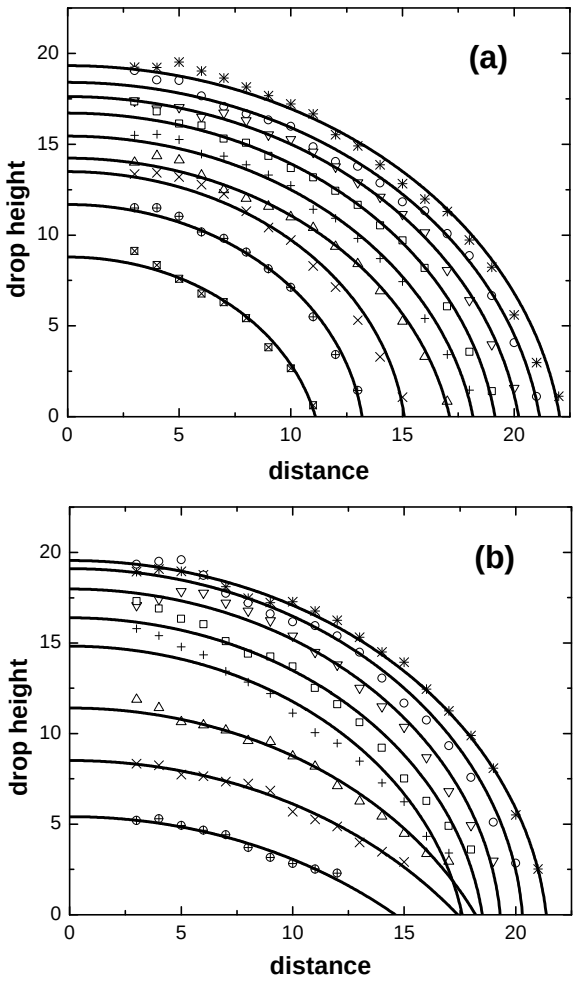

Figure 6.06 Average droplet shape for evaporating droplets on (a) nonsoluble and (b) soluble substrates. Full lines are mathematical fittings with the spherical cap equation.

The evaporation dynamics is intrinsically related to the formation of ringlike deposits. According to the literature, droplets can follow two evaporation schemes [Picknett'77, Jia'02]. In the first, the contact radius decreases as the droplet evaporates, but the contact angle remains the same. In the second case, the contact radius remains constant but the contact angle decreases (see Figure (6.02)). This effect is known as the pinning of contact area and occurs due to roughness or chemical inhomogeneities at the surface [Butt'03]. Previous works report that ringlike deposits occur only when the droplet contact area is pinned [Deegan'97, Uno'98, Deegan'00, Sequeira'03, Sequeira'06]. It was not clear, however, if the droplet pinning is a requirement for deposit formation or rather a consequence of material deposition in the first stages of evaporation.

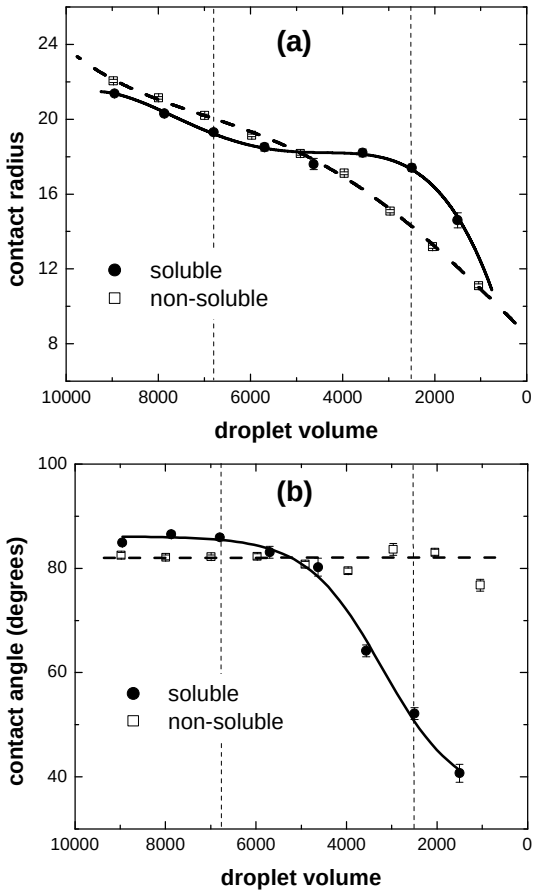

Figure 6.07 Variation of (a) contact radius and (b) contact angle during evaporation. The droplet volume is regarded as the total number of solvent beads remaining in the droplet. The central region limited by the vertical dashed lines corresponds to the pinned contact area evaporation regime in the case of soluble substrate. The thicker lines are visual guides.

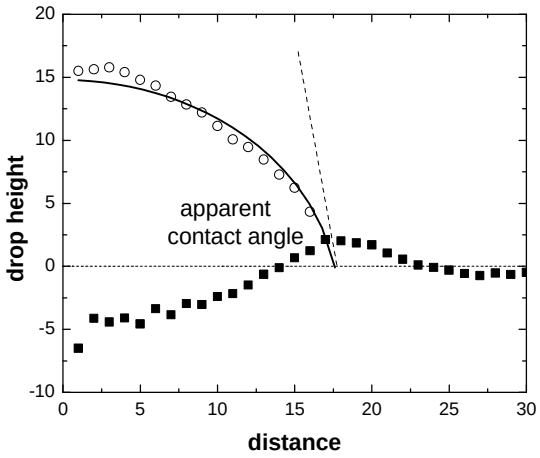

Figure 6.08 Determination of the apparent contact angle in the case of droplets on soluble substrates. The full line represents a spherical cap fitting.

Figure (6.06) compares how the shape of simulated droplets changes with time for two situations, namely the droplet evaporation at insoluble substrate and the evaporation together with substrate swelling. In the first case, since the substrate is perfectly smooth and homogeneous, the evaporation follows the constant contact angle regime. When the substrate is allowed to dissolve, the evaporation also follows this regime at early times. However, as the ring deposition starts, the contact diameter becomes constant and the contact angle starts to decrease, i.e., the droplet is pinned. Figure (6.07) shows a quantitative picture of this effect. The contact diameter and angle obtained for the case of ring formation are just apparent quantities obtained from the spherical cap fitting, since the droplet does not really touch the surface at its original level because of the ring formation (Figure (6.08)). Our simulation results suggest that, at least in the set of parameters explored here, the pinning of the contact area seems to be rather an outcome of the solid material deposition [Cordeiro'05].

6.3.3. Explicit Consideration of Polymer Chains and Influence of Chain Orientation

Simulations in which polymer chains were explicitly considered were based on the same interaction parameters as in the previous section. The difference is that now connectivity between different elements of the substrate was implemented. The substrate had a thickness corresponding to 30 lattice sites and was formed by an ensemble of monodisperse polymer chains with 20 elements each and flexible backbones. A chain size equivalent to 20 elements is comparable to the droplet radius.

It turns out that the initial chain configuration when droplet evaporation and substrate swelling starts has a remarkable impact on the geometry of the pattern generated on the surface. Figure (6.09) shows that, when chains are allowed to reach their equilibrium orientation inside the polymer film before evaporation and substrate swelling starts, the pattern shape resembles the one obtained for the general case, i.e., a depression surrounded by a ringlike deposit. The symmetry is not perfectly radial due to the roughness associated with the small size of the microstructure. Radial symmetry would however become clearer if more simulations were used for the calculation of the final averaged pattern profile. Due to the connectivity between SU elements, the problem of formation of a substrate gas pointed out in the last section is avoided. In Chaper 5, it was shown that polymer chains confined in a thin film are preferably oriented parallel to the surface of the film. This corresponds to a self-induced residual orientation and seems to have no apparent influence on the shape of

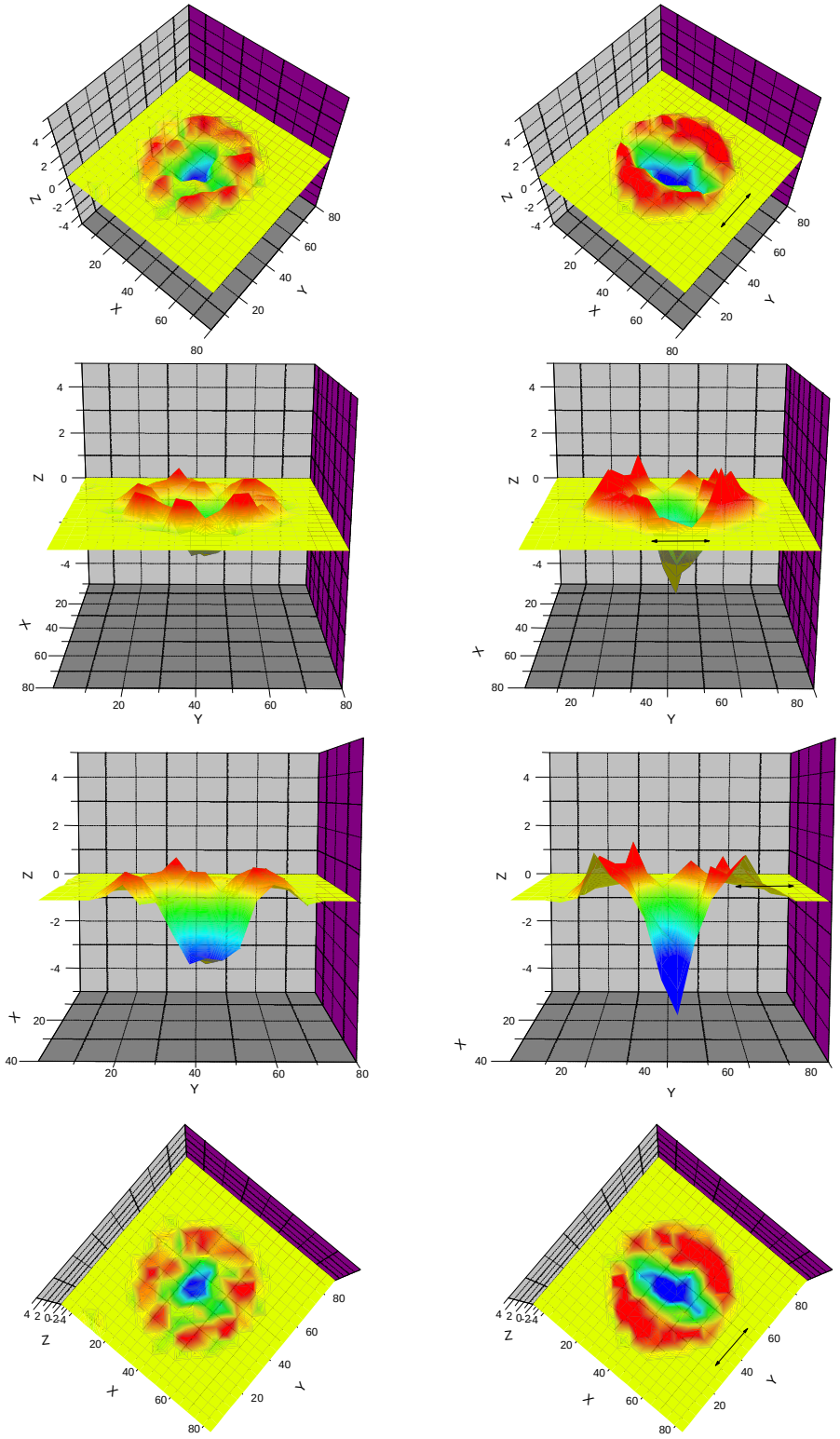

Figure 6.09 Different perspectives of the final pattern shape for substrates where chains had a residual equilibrium orientation (left column) and a strong induced uniaxial orientation (right column) (see Figure (6.03)). Pictures were first averaged from two different simulations with distinct initial conditions and then smoothed by averaging neighboring points at the surface. Black arrows indicate the direction of chain backbones for uniaxially oriented chains.

the microstructure, if compared with the general case of simple molecules. The influence of orientation is observed only in the case of strong induced orientation, i.e. when the initial configuration of chains is perfectly uniaxial and parallel to the surface. Figure (6.09) shows that, in this case, the deposit formed on the substrate has a shape similar to a pair of half moons. The reason is that chains in such configuration are strained along their backbones. To relieve the tension, swollen chains must coil. Take a chain located under the contact line as an example. At one side, it is movable due to the diffusion of solvent inside the film. At the other side, where solvent needs much more time to reach, it is anchored to the solid polymer structure and is not mobile. This tension is reflected on the height of the deposit, which is more pronounced in the direction of the tension.

6.4 Final Considerations

In the case of soluble surfaces, it is possible to simulate the effect of microwell and ringlike deposit formation by properly choosing the interaction parameters between the components of the system. Swollen substrate particles migrate to the border of the droplet to minimize the contact between solvent and vacuum, which costs the most energy. The ring formation in the first stages of evaporation results in pinning of the droplet contact area [Cordeiro'05]. We believe that the knowledge of these features is of relevance for the technological application of droplets in surface microstructuring, in the sense that it clarifies the relevance of molecular interactions and consequently surface tensions in the choice of the appropriate solvents and substrates for pattern formation. The importance of the chemical identity of the surface in determining the formation or the absence of ringlike deposits has been experimentally addressed as well [Uno'98].

The molecular simulation method described here focuses mainly on the contribution of interactions for the final shape of the pattern but does not rule out previously proposed models based on hydrodynamics [Deegan'97, Deegan'00, Sequeira'03, Sequeira'06]. We emphasize that, although liquid fluxes were not explicitly considered in our simulations, they are known to contribute to the pattern formation as well. However, they should not be considered as the only cause for pattern formation. There is a myriad of additional effects that may lead to similar

behavior as predicted by the liquid flux model or even to a completely different pattern shape. Finite element calculations suggest that temperature inhomogeneities may arise from the evaporation process, leading to a thermally induced Marangoni effect [Hu'05]. In this sense, in addition to the flux from the middle to the border of the droplet, another flux in the opposite direction appears as consequence of the thermally induced Marangoni effect. This additional flux tends to homogenize the environment inside the droplet and it is thought to lead to the formation of deposits in the center of the contact area instead of the traditional ringlike pattern at the border [Hu'06]. Another way to explore the Marangoni effect is to use a droplet constituted by a mixture of solvents. If one component is considerably more volatile than the other, it will be fastly depleted from the regions close to the contact line of the droplet, where the evaporative flux is stronger [Hu'02]. In this case, one has a composition gradient along the surface, i.e., a composition-induced Marangoni effect. Droplets of polymer solutions constituted by a mixture of two solvents were demonstrated to generate deposits with the shape of a dot instead of a ringlike deposit [de Gans'04]. This result is very important because frequently one is interested in obtaining a deposit in the shape of a dot, as is the case in inkjet printing, or at least in minimizing the ringlike deposit formation, as may be the case in DNA microarrays [Blossey'02], where a more homogeneous deposit is desired. Equivalent results were obtained by Karabasheva *et al.*, who extended such experiments for the case in which the polymer is not initially inside the droplet, but is gradually dissolved from the substrate [Karabasheva'06]. The generated microstructures exhibited a pronounced focusing effect and the authors pointed out the possibility of applying the method for the fabrication of microlens arrays. Deposit shapes with even more complex structure were also observed in cases in which the fast evaporation leaded to the formation of a glassy polymer skin in the surface [Pauchard'03]. In these cases, the traditional ringlike deposit was not observed.

The last point we would like to consider is the pattern formation when polymer chains are explicitly considered. Our simulations show that chains in their equilibrium configuration do not have an expressive impact on the final shape of the deposit as compared to the general case of simple molecules. However, by considering chains uniaxially oriented parallel to the surface, a pattern with the shape of a hole surrounded by two half moons is observed. The anisotropy in the shape of the pattern is a result of a residual tension that the chains have in the direction along

their backbone. Chains with the conformation considered here are characteristic of stretched or extruded polymer films. Anisotropic patterns were also observed experimentally for the case of extruded polystyrene films [Li'06]. The only difference is that the formation of such structure could be accomplished only without direct contact between the droplet and the surface, just by approaching both and letting the solvent vapor swell the surface. We are still waiting for direct experimental verification in the contact mode.

From the side of simulations, it would also be interesting to simulate bigger systems and study the orientation of deposited chains inside the ringlike deposit. Experimental studies with rigid proteins have shown a strong tangential orientation of the molecules close to the contact line [Vonna'05], a phenomenon that could be exploited in the fabrication of oriented polymer films and fibers.

7

Oscillating Chemical Reactions in Confined Geometries

7.1 Scientific Background

The history behind the field of nonlinear chemical dynamics is maybe one of the best examples of developments in science which were born several decades before the community was ready to acknowledge them. The first observations of chemical reactions displaying periodic oscillations in the concentration of reactants date back at least to the early nineteenth century [Epstein'96]. In the early twentieth century, Lotka developed a simple model based on two sequential autocatalytic reactions giving rise to oscillatory behavior [Lotka'10, Lotka'20]. The model was promptly accepted by ecologists in order to explain the oscillatory dynamics of populations constituted by preys and predators [Epstein'96, Kuhn'00]. However, from the chemical point of view, the model was too abstract and did not have an experimental counterpart. Not to mention that the early experiments showing chemical oscillations were already met with great skepticism by a chemical community whose principles were at this time firmly enrooted in classical thermodynamics. In spite of all resistance, two scientists developed and refined in the 1950s one of the most famous oscillating reactions, which was later named after them as the Belousov-Zhabotinsky (BZ) reaction. This reaction is based on the oxidation of malonic acid by bromate. Using cerium ions as catalyzers and the appropriate redox indicator, a dramatic red-blue color change is observed periodically in the reactor [Györgyi'92, Epstein'96, Kondepudi'98, Kuhn'00]. The BZ reaction gradually began to receive acceptance from the

community, in part due to the advent of the field of nonlinear thermodynamics in the 1940s. During the 1960s, the group of Prigogine in Brussels proposed a chemically plausible model for chemical oscillations, the so called *Brusselator* [Kondepudi'98]. This model is based on a cascade of reactions with an autocatalytic step. It is assumed that reactions occur in a well stirred reactor and that the concentration of reactants is kept constant at a desired non-equilibrium value through appropriate flows, which are also responsible for removing the reaction products as they are formed. The concentration of reaction intermediates involved in the autocatalytic step may reach a steady state or rather oscillate in time, depending on the input parameters such as reaction rates and flow velocities. Another model, the so called *Oregonator*, was later proposed by Field, Körös and Noyes to account for the oscillatory behavior of the BZ reaction in specific [Epstein'96]. The mechanism captures the essential chemistry of the process by means of a three-variable model that is of course oversimplified in comparison with experimental reality. The model is for instance not able to reproduce the observation that the BZ reaction exhibits chaotic behavior under certain circumstances [Strogatz'94]. This was first accomplished by a new scheme proposed by Györgyi and Field [Györgyi'92]. Better theoretical understanding about chemical oscillations allowed the identification and the engineering of several other oscillators in a systematical way [Epstein'96]. Soon it became clear that oscillating reactions constituted not only an isolated curiosity but a widespread phenomenon in nature, with a great impact in society. In general, heterogeneous catalysis involving different adsorbates show complex oscillatory behavior, as is the case with $CO + O_2$ and $NO + H_2$ on Pt surfaces [Caballero'03]. The importance of understanding and optimizing such reactions lies on the toxicity of CO and NO. Oscillating reactions have also biological relevance. An example of in vivo oscillating reaction is the oxidation of NADH by O_2 catalysed by horseradish peroxidase [Epstein'96]. Oscillating reactions are also known to control circadian rhythms. The molecular mechanism of circadian oscillations relies on the negative autoregulation exerted by a protein on the expression of its gene. These oscillations can occur even in constant environmental conditions, for instance constant darkness, meaning that they constitute a kind of "chemical clock" [Gonze'03]. Cardiac cells are also known to exhibit periodical dynamics which may eventually evolve to uncontrolled chaotic behavior [Guevara'81]. Strategies have been designed to control chaos by means of feedback

algorithms [Petrov'93] and periodic perturbations imposed to the chaotic system [Li'04].

There is a wide open space for research in the field of nonlinear chemical dynamics. For instance, motivated by the recent interest on chemistry in confined geometries, one may pose the question on how space restrictions influence the nonlinear behavior of chemical systems. In fact, this specific question is the topic we would like to address in the following sections.

7.2 Methodology

In the present work, our aim was to investigate the effect of geometrical confinement on an oscillating reaction by means of dynamic Monte Carlo simulations with molecular resolution. We were mainly motivated by the growing interest of the scientific community on chemistry in micro and nanoreactors. Furthermore, many oscillating reactions take place *in vivo* inside the cell, which is essentially a confined environment [Minton'92]. It seems reasonable to speculate that spatial restrictions may be a key factor cleverly explored by the cell machinery. Considering the high sensitivity of oscillating reactions to input parameters, their behavior in restricted geometries may be significantly different from the bulk behavior [Provata'99]. As a model reaction we have chosen a variation of the well established mechanism called the *periodically forced Brusselator* [Hao'83, Kruel'90, Liu'96]. This mechanism can be translated into a cascade of plausible elementary chemical reactions and is very well suited for molecular simulations because the discrepancy between the concentrations of several intermediates does not exceed one order of magnitude in the course of reaction. The difference from the classical version of the Brusselator is that now a periodic force is applied to the system and accounts for the appearance of chaotic behavior in specific regions of the parameter space. Reactions taking place in the bulk and under confinement between rigid and non-interacting parallel walls were investigated. Geometrical confinement may have a significant impact on the oscillatory behavior of reactions. We found that a reaction that is periodic in the bulk can burst into chaos when confined and vice-versa, indicating that geometrical confinement may also be regarded as a way of controlling chaos. To explain the

results, we use a mean field lattice theory, in which the effect of confinement is incorporated in the expressions for the reaction rate constants as done in Chapter 4.

There are two ways by means of which confinement can influence the dynamics of oscillatory systems. The first one is associated with the reduced number of elements in the system and consequently with the noise associated with thermal fluctuations. This is essentially a finite size effect and has been already investigated by means of molecular simulations [Zhdanov'01] and stochastic numerical models [Kruel'90, Geysermans'97, Wang'97, Wang'00, Gonze'03]. The second effect is rather classified as a boundary effect. It is related to the steric hindrance imposed by the walls, culminating in the reduced number of realization possibilities for reactions attempted in their vicinity. Our contribution focuses mainly on the boundary effect. Its investigation is not straightforward since high thermal fluctuations constitute an intrinsic limitation of molecular simulations. We searched the parameter space for regions where the system is not much sensible to the noise introduced by thermal fluctuations. In order to separate noise from the deterministic oscillatory behavior, the study of time series was complemented by evaluation of the correspondent attractors [Atkins'02] and Fourier spectra. We also investigated the effect of noise in regions of the parameter space of higher sensitivity. Finally, we applied the mean field model derived here to speculate about the possibility of changing irreversibly the oscillatory behavior of a given bulk system by placing it for short time under parallel walls and then returning it to the bulk condition.

7.3 Model Implementation

Molecular simulations were performed in a fcc lattice with 12 nearest neighbors (see Figure (4.01)), each site representing a single molecule. Reactions in the bulk were simulated in a cubic box with periodic boundary condition in all directions. It had dimensions of 120 molecular elements in each direction, totalizing 8.64×10^5 elements. This means that the size scale investigated here is in the order of nanometers. Confinement was imposed by placing the system between two rigid walls, forming a lamella. The distance between walls was varied to simulate different degrees of confinement, but always keeping the total volume practically constant. The

choice of the reaction mechanism to be taken as a model for oscillating reactions in simulations is not a straightforward task. The mechanism should be simple enough to be translated into a cascade of plausible elementary chemical reactions, but at the same time it must provide a rich scenario of periodic oscillations and chaos. The scheme proposed by Györgyi *et al.* for the BZ reaction [Györgyi'92] would be a candidate if it would not involve simultaneous consideration of species whose concentrations are orders of magnitude different from each other. In such a situation, explicit consideration of individual molecules challenges the computational resources usually available. Examples of mechanisms which fulfill the requirements above are the Willamowski-Rössler [Geysermans'96] and the periodically forced Brusselator [Hao'83, Kruel'90, Liu'96]. In the simulations presented here, we have chosen a reaction scheme that is very similar to the well established periodically forced Brusselator. The reaction cascade with the correspondent rate constants *k* is expressed as:

$$\mathrm{A} \xrightarrow{k_1} \mathrm{X}, \tag{7.01a}$$

$$\mathrm{B} + \mathrm{X} \xrightarrow{k_2} \mathrm{Y} + \mathrm{S}, \tag{7.01b}$$

$$2\mathrm{X} + \mathrm{Y} \xrightarrow{k_3} 3\mathrm{X}, \tag{7.01c}$$

$$\mathrm{C} + \mathrm{X} \xrightarrow{k_4} 2\mathrm{S}. \tag{7.01d}$$

The system is open with respect to the species A, B and C, whose concentration is held constant. In practice, this means that there is an inflow of these reactants in the system. Species labeled as S represent either the reaction products or the chemically inert solvent used in the reaction. There is no distinction between both because they do not take active part in any reaction and can be removed by an outflow [Geysermans'96]. Oscillations in concentration involve species X and Y, which participate in the autocatalytic step represented by Equation (7.01c). The reactions above are similar to the classical version of the Brusselator [Kondepudi'98]. The only difference is that, in the present case, Equation (7.01d) was considered as a bimolecular instead of monomolecular reaction. This change allowed to better

distinguish this reaction from others also involving species X and to facilitate the model implementation and the translation of rate constants into reaction probabilities used as input parameters in simulations. Although these reactions account for the appearance of periodic oscillations, their parameter space does not exhibit regions of chaotic behavior unless a periodic force is imposed on the system. This force is accomplished by removing molecules of species X in a periodic fashion. Following mass action laws and assuming that the reactor is constantly stirred to eliminate diffusion effects, the reaction dynamics under the influence of a force is expressed as:

$$\frac{dX}{dt} = k_1 A - k_2 BX + k_3 X^2 Y - k_4 CX + F(t)\,, \tag{7.02}$$

$$\frac{dY}{dt} = k_2 BX - k_3 X^2 Y\,, \tag{7.03}$$

with the time dependent behavior of the force $F(t)$ being given as:

$$F(t) = a\cos(wt) - bw\ . \tag{7.04}$$

In previous works, the parameters a and b were taken as constants and w as a bifurcation parameter [Hao'83, Liu'96]. In these works, regions of the parameter space such as the one where k_1A = 0.46, k_2B = 1.2, k_3 = 1, k_4C = 1, a = 0.05 and b = 0.2 were thoroughly explored [Hao'83, Liu'96]. The advantage of choosing this particular set of parameters is that, by varying w between 0.5 and 1, a very rich scenario was obtained, including regions of periodic behavior, period doubling bifurcations and deterministic chaos [Liu'96]. In the present work, we focused on similar regions of the parameter space but added a new variable: the geometrical confinement.

After choosing the desired region of the parameter space, the correspondent parameters were used as input values in molecular simulations. The phenomenological rate constants k are related to the reaction probabilities, which determine if a reaction attempt is successful or not in simulations. Later, it will be discussed in more details how to translate k to a probability value P so that simulations can be compared to the phenomenological kinetic equations. For now, let

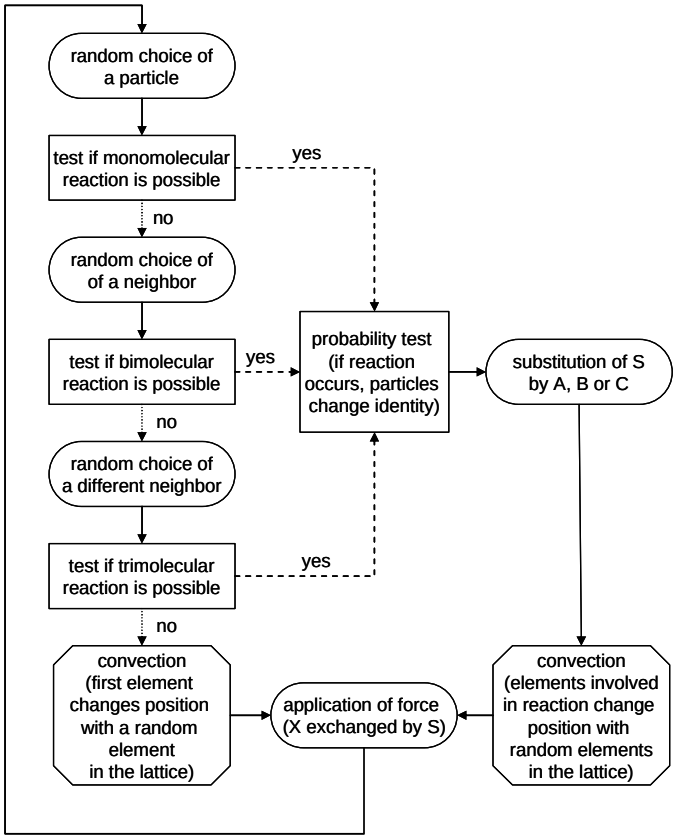

Figure 7.01 Sequence of steps performed during a single iteration in molecular simulations.

us consider the general simulation procedure. Figure (7.01) brings a schematic description of the sequence of steps performed iteratively in simulations. First, an element is randomly chosen in the lattice. In case of it being an A, the reaction attempt is identified as the monomolecular process (Equation (7.01a)), otherwise one of its 12 neighbors is randomly chosen and the program tests if the combination corresponds to one of the bimolecular processes (Equations (7.01b) and (7.01d)). If it is still not the case, one of the remaining 11 neighbors is chosen to identify an eventual trimolecular process (Equation (7.01c)). A reaction that is identified is not necessarily realized, since its probability must first be computed. In analogy to the Metropolis test (see Section (2.1.3)), reaction attempts are considered as successful only when the reaction probability exceeds a random number between 0 and 1 generated by the computer. If a reaction is successful, the program changes the identity of the involved species. Every time an element of species A, B or C is consumed, an element S is chosen and promptly substituted by the consumed species

in order to keep its concentration constant [Geysermans'96]. It is assumed that diffusion and convection effects are fast enough to keep the system homogeneous, at least in the nanoscopic length scale of the systems simulated here. Therefore, after a reaction attempt, the program selects all the elements involved in it and changes their positions with elements randomly chosen in any position of the lattice. The process of cooperative rearrangements is not necessary here since molecular motions are performed by means of random jumps between two positions in the lattice, independent of the distance between them. This prevents the formation of concentration correlations and patterns, a more complicated scenario that we would like to indicate as a possible candidate for future studies. Finally, the program imposes a controlled force to the system by removing X elements and substituting them by S, as dictated by the force in Equation (7.04). This returns the algorithm to the step of selecting a new random element. The process is then repeated iteratively. It is considered that one unit of time comprises a number of iterations equal the number of elements in the system.

In order to have a connection with the phenomenological model, reaction probabilities *P* in simulations must be appropriately derived from the rate constants *k*. Applying basic probability theory, one finds that:

$$P_i = \frac{k_i}{\Omega g^{\,\Omega-1}}, \tag{7.05}$$

where Ω denotes the number of realization possibilities, that equals 1, 2 or 3 for mono, bi or trimolecular reactions, respectively. The parameter *g* stays for the value of molar fraction that was chosen as the concentration unit in simulations. More specifically, the concentration of a given reactant was taken as 1 when its molar fraction *g* corresponded to 0.1, i.e. one tenth of the total amount of molecules. Results obtained from molecular simulations were compared to the numerical solution of Equations (7.02) and (7.03) with the correspondent parameters. The set of nonlinear differential equations was integrated in a discretized way by the recurrence formula:

$$X_{t+\Delta t} = X_t + \left(\frac{dX}{dt}\right)_t \Delta t, \tag{7.06}$$

TABLE 7.01: Parameters Adopted in Molecular Simulations and in the Mean Field Model

parameter	value	units[a]
A, B, C	1	[concentration]
k_1	$0.46\,l$	$[\text{time}]^{-1}$
k_2	$1.2\,l$	$[\text{concentration}]^{-1}\,[\text{time}]^{-1}$
k_3	l	$[\text{concentration}]^{-2}\,[\text{time}]^{-1}$
k_4	l	$[\text{concentration}]^{-1}\,[\text{time}]^{-1}$
a	$0.05\,l$	$[\text{concentration}]\,[\text{time}]^{-1}$
w	varied from $0.5\,l$ to l	$[\text{time}]^{-1}$
b	varied from 0.1 to 0.2	[concentration]
l	0.03	—

[a] The concentration unit was considered as corresponding to the molar fraction $g = 0.1$ and the time unit as the number of reaction attempts equal to the total number of molecules in the system. Quantities derived from the parameters listed here hold correspondent units.

which can be applied for Y as well. It is important to point out that Equation (7.06) does not provide a rigorous solution and may not be reliable in regions close to bifurcation points. Besides that, the solution may exhibit dependence on the mesh size. An investigation with such level of details is nevertheless not the objective here. The most important point is that Equation (7.06) is easy to handle and provides results that are very close to those reported in other works where the same set of nonlinear differential equations was solved in a more rigorous way [Kruel'90, Liu'96]. In the regions of parameter space explored here, time series calculated with Equation (7.06) can be safely compared to simulation results. Difficulties may arise, however, because the numerical solution is deterministic while molecular simulations are essentially stochastic. Simulations exhibit thermal fluctuations which may mask the underlying deterministic behavior [Kruel'90, Geysermans'97, Geysermans'96, Wang'97, Wang'00, Gonze'03]. To minimize the influence of noise, we have selected regions of the parameter space that turned out to be less sensible to fluctuations.

Table (7.01) lists the set of input parameters adopted here. Note that the rate constants are equivalent to those adopted in previous works [Hao'83, Kruel'90, Liu'96], with the difference that here they were multiplied by a constant l. The parameter l is a normalization factor that optimizes simulations by setting the value of the highest probability close to 1 in Equation (7.05). The normalization requires the constants a and w in Equation (7.04) to be also multiplied by l. Using the appropriate

parameters, simulations started from a mixture of components uniformly and randomly distributed, whose initial concentrations were $A = B = C = 1$ (held fixed throughout the process), $X_0 = 0.4$ and $Y_0 = 3$. The remaining sites were filled with S. Time series were recorded after a transient period of time. Following a previous approach [Kruel'90], the study of time series in combination with the correspondent attractors [Atkins'02] and Fourier spectra [Press'88, Jordan'94] was used a diagnostic test for periodic or chaotic behavior.

7.4 Simulation Results and Discussion

The first point we would like to demonstrate is that reactions which oscillate periodically in the bulk may burst into chaos under confinement. First, it is necessary to identify regions of the parameter space which are periodic in the bulk. This was already done by numerical solution of Equations (7.02) and (7.03) [Hao'83, Liu'96]. Figure (7.02) brings an example of a region of the parameter space specified in Table (7.01) with $b = 0.2$ and $w = 0.74l$. In the bulk, the concentrations of components X and Y exhibit sustained oscillations which agree very well with the numerical solution of the nonlinear differential equations. Focusing on the time series obtained from molecular simulations, it is observed that successive concentration minima fluctuate as function of time, but this should not be confused with chaos. This is rather induced by thermal fluctuations. Due to these fluctuations, simulations exhibit a limit cycle scattered around the deterministic predictions. Fourier transformation of the time series clearly separates the deterministic and stochastic components. Both simulation and numerical solution show a well defined band followed by its discrete harmonics, a behavior that is characteristic of periodicity. Molecular simulations deviate from the deterministic model only in the baseline which is slightly noisy. It turns out, however, that not all the periodic regions predicted by the numerical solution are appropriate for simulations. Figure (7.03) brings an example with $b = 0.2$ and $w = 0.575l$ in which the system sensitivity to noise is so high that fluctuations mask the periodic behavior. Comparing the deterministic and stochastic cases, it is observed in some moments that something similar to a phase delay appears. Evaluation of the limit cycle obtained from simulations does not allow to diagnose periodic behavior. The attractor

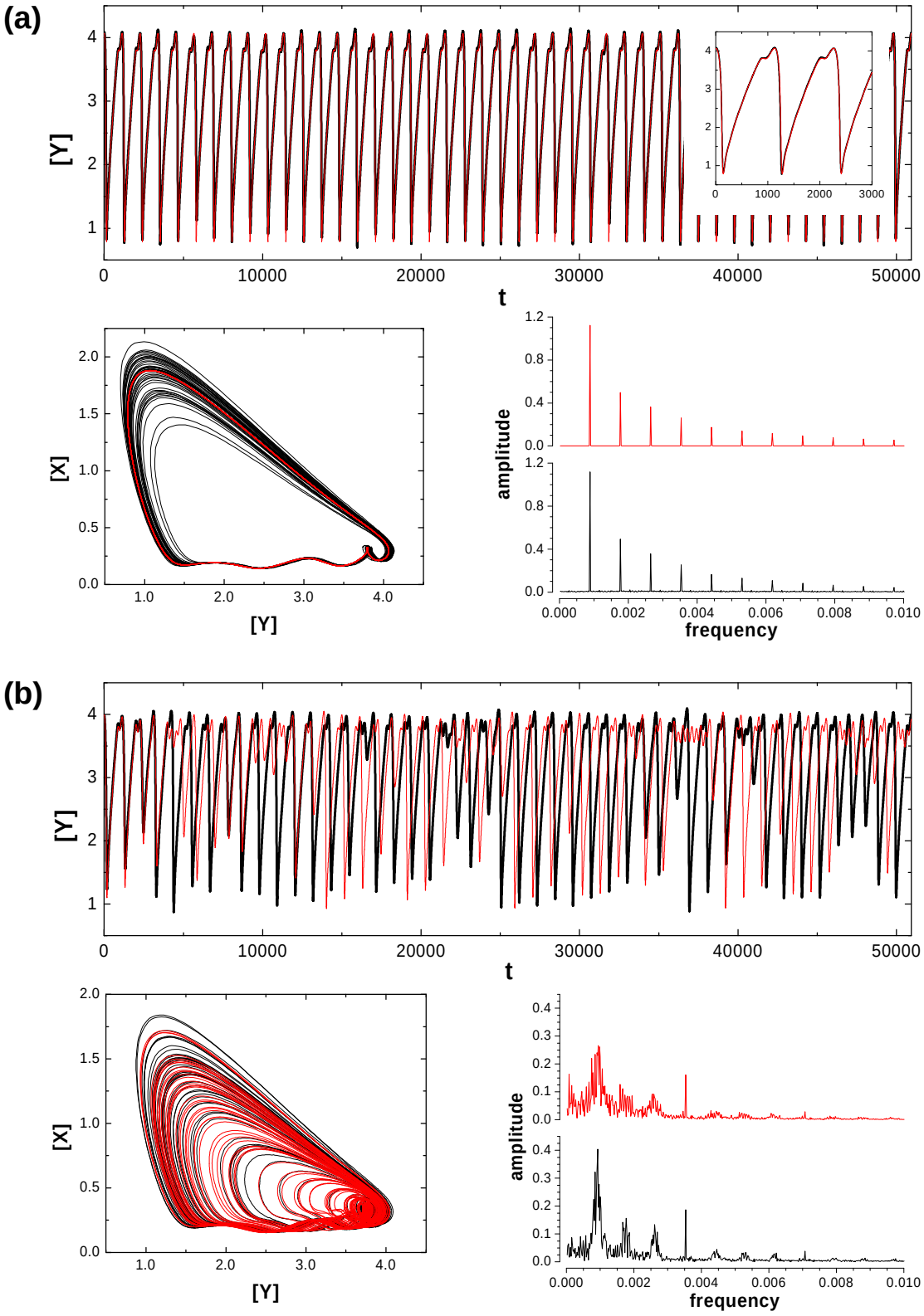

Figure 7.02 Oscillatory behavior of a reaction (a) in the bulk and (b) confined in a lamella with thickness of 10 molecular layers (parameters specified in Table (7.01), with b = 0.2 and $w = 0.74\,l$). Upper graphs are time series (inset shows an expanded scale), to be compared with attractors (lower left) and the Fourier spectra (lower right). Black lines represent results from molecular simulations and red lines the numerical solutions according to the mean field model.

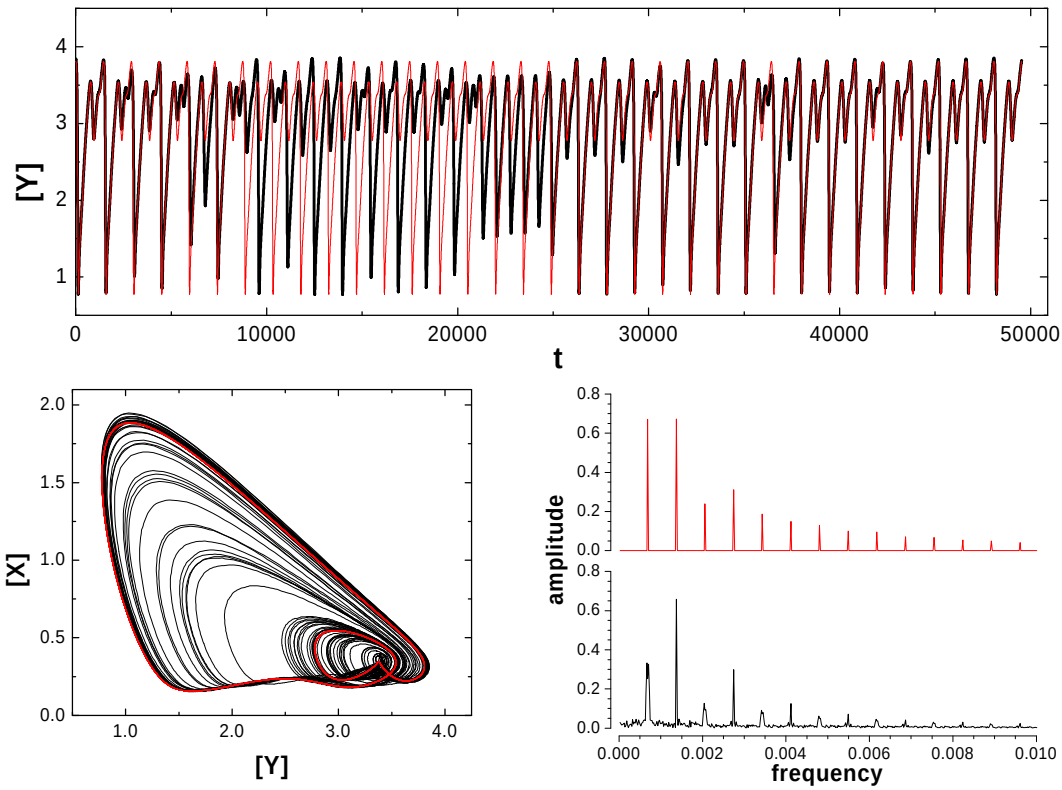

Figure 7.03 Oscillatory behavior of a reaction in the bulk (parameters specified in Table (7.01), with b = 0.2 and $w = 0.575\,l$). Upper graphs are time series, to be compared with attractors (lower left) and the Fourier spectra (lower right). Black lines represent results from molecular simulations and red lines the numerical solutions according to the mean field model.

predicted by the numerical solution is a double cycle. However, fluctuations in simulations seem to spread the trajectory between these two cycles, giving rise to a scenario that rather resembles the strange attractor [Atkins'02] of a chaotic system [Geysermans'97]. The apparent phase shift observed in some parts of the time series occurs because the reaction does not alternate evenly between the large and the small cycles. Fluctuations may force the simulated reaction to go for instance twice through the same cycle before exploring the other one. This is an intrinsic limitation associated with the finite size of simulated systems. A clearer hint about periodic behavior is given only by the band structure of the frequency spectrum. Even then, regions of the parameter space with such high sensitivity and providing dubious results were avoided in the study developed here.

Returning to Figure (7.02), the reaction with the same parameters as in the bulk was performed under space restrictions, in a lamellar system confined in one direction by parallel rigid walls. Figure (7.02) shows the behavior when the reaction is

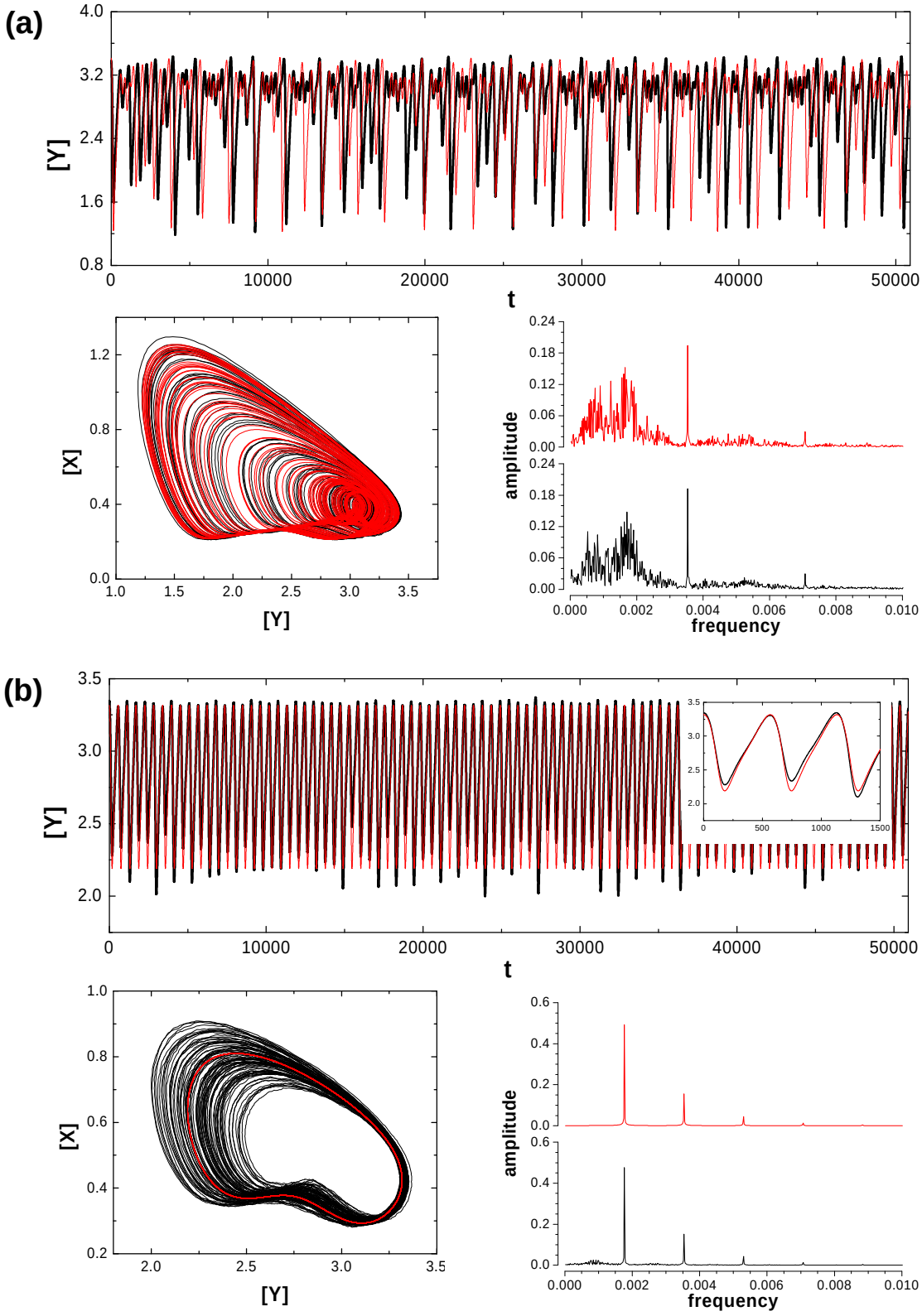

Figure 7.04 Oscillatory behavior of a reaction (a) in the bulk and (b) confined in a lamella with thickness of 4 molecular layers (parameters specified in Table (7.01), with b = 0.1 and $w = 0.74\,l$). Upper graphs are time series (inset shows an expanded scale), to be compared with attractors (lower left) and the Fourier spectra (lower right). Black lines represent results from molecular simulations and red lines the numerical solutions according to the mean field model.

confined in a lamella with thickness equivalent to 10 molecular elements. The time series exhibit now aperiodic behavior. We developed a mean field lattice model, similar to the one described in Chapter 4, in order to incorporate the effect of confinement on the deterministic solution of Equations (7.02) and (7.03). This model incorporates the geometrical confinement on the expression for rate constants by considering it as a boundary effect. This is different from a finite size effect arising from the low number of agents in the system. A boundary effect is rather related to the steric hindrance imposed by the walls. As shown in Figure (4.01), molecules close to the walls have no longer 12 neighbors as potential partners in the reactions, but only 8. This reduced number of realization possibilities in the lattice is incorporated in the model by a mean field approach. Confinement changes the rate constant of bimolecular and trimolecular reactions because they depend on encounters between different molecules. Differently, the rate constant of the monomolecular reaction remains unchanged because it involves “decomposition” of a single molecule. Calling q the fraction of molecules in the vicinity of a wall (i.e. a quantity related to the area/volume ratio), the rate constants under confinement can be expressed as:

$$k_{mono}^{conf} = k_{mono}^{bulk}, \tag{7.07}$$

$$k_{bi}^{conf} = \left[(1-q)+\frac{8}{12}q\right]k_{bi}^{bulk} = \left(1-\frac{2}{3d}\right)k_{bi}^{bulk}, \tag{7.08}$$

$$k_{tri}^{conf} = \left[(1-q)+\frac{8}{12}\cdot\frac{7}{11}q\right]k_{tri}^{bulk} = \left(1-\frac{38}{33d}\right)k_{tri}^{bulk}, \tag{7.09}$$

where d is the lamella thickness expressed as the number of molecular layers, so that $d = 2q^{-1}$ (see Chapter 4 for an analogous treatment of the dependence of reaction rate constants on confinement). Confinement changes the rate constants by different relative amounts and this may lead to a drastic change of the oscillatory pattern. Incorporating Equations (7.08) and (7.09) in the deterministic solution of the nonlinear differential equations (Equations (7.02) and (7.03)) leads to results very close to those obtained from simulations, as demonstrated by Figure (7.02). Chaotic behavior in the confined system is observed both in molecular simulations and the

mean field solution. A perfect superposition of the deterministic and stochastic time series should not be expected due to the very high sensitivity of chaotic systems. However, the Fourier transforms of both are very similar. The frequency spectrum shows a broadband structure characteristic of chaotic systems. Intriguingly, there is a well defined single band at a frequency of 0.0035 that is very robust against confinement.

Maybe more interesting than a transition from periodicity to chaos induced by confinement would be the opposite case, i.e., when confinement is able to control the chaotic behavior of a bulk system leading it to periodicity. Figure (7.04) shows that such an effect can be observed in a different region of the parameter space, where b = 0.1 and $w = 0.74\,l$. A good agreement with the mean field model is again observed. In fact, simulations in other regions of the parameter space not shown here exhibit a fairly good agreement with the mean field predictions, as long as thermal fluctuations are small enough to allow a comparison. With this in mind, we incorporated the lamella thickness in the parameter space and mapped part of it by solving numerically the nonlinear differential equations. Figure (7.05) shows two-dimensional maps of the oscillatory behavior considering the lamellar thickness d and the frequency w of the periodic perturbation as variable parameters. Maps are shown for two different values of the parameter b, namely 0.2 and 0.1. Different oscillatory regimes are characterized by the number of intersections between the attractor in its three-dimensional form (X, Y, coswt) and the Poincaré plane coswt = 1 [Kruel'90, Liu'96]. Existence of a few intersections indicates periodic behavior and a large number of intersections (tending to infinity for infinitely large sampling times) indicates chaos. To a good approximation, the black regions in the maps of Figure (7.05) represent chaos or nearly chaotic behavior, whereas all the other colored regions represent periodic behavior with different degrees of complexity. Obviously, especially close to bifurcation points, the maps may be unprecise due to approximations in the calculations and finite sampling time. Figure (7.05) also brings bifurcation diagrams showing specific regions of the parameter maps which were investigated in Figures (7.02) and (7.04), illustrating in detail the transitions from periodicity to chaos and vice-versa. Note that the behavior of Y as function of w in the bulk system where b = 0.2 is very close to previously obtained results [Liu'96], even being our strategy of solving the nonlinear differential equations based on a non-rigorous integration

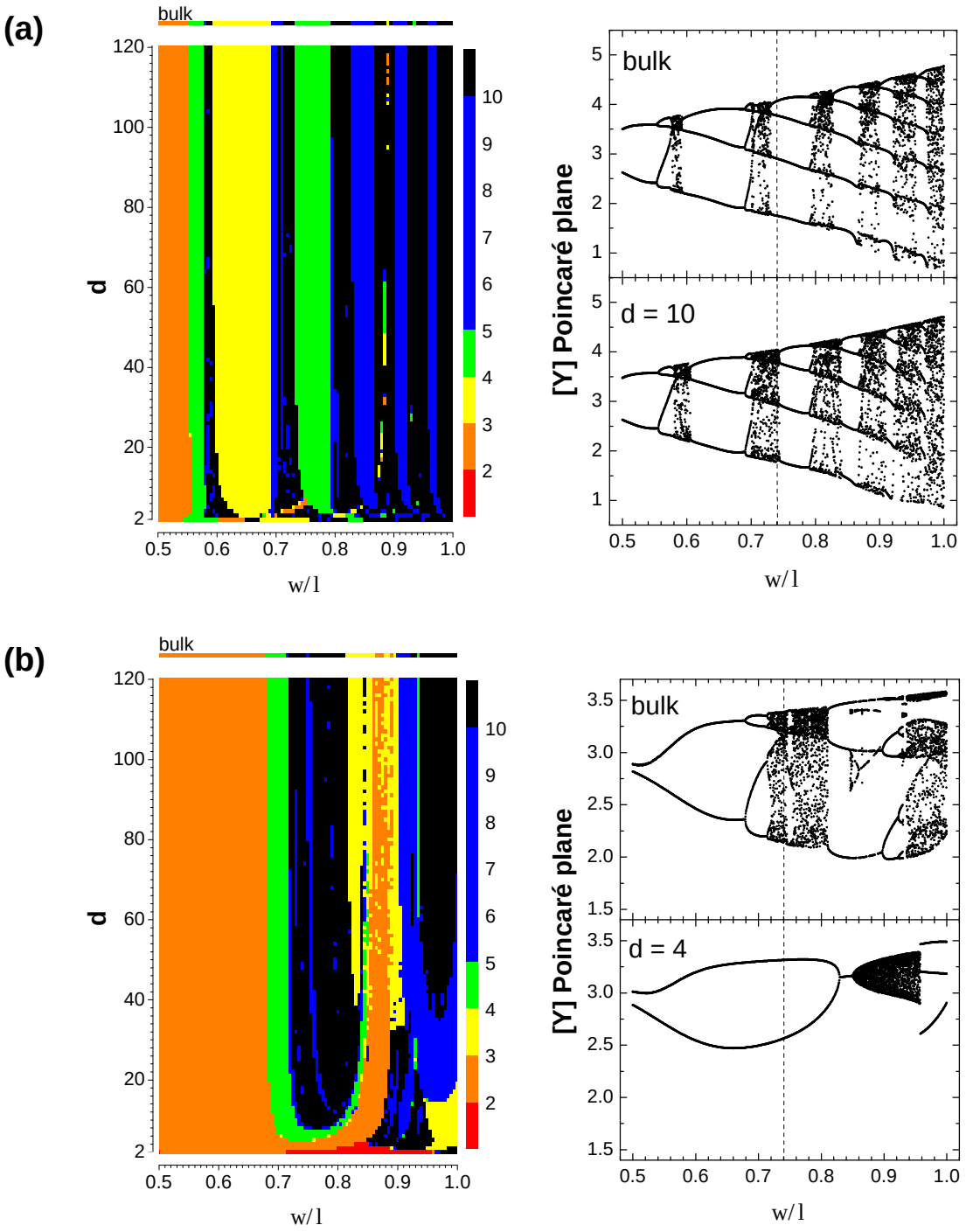

Figure 7.05 Maps representing (d,w) sections of the parameter space (left column) and (Y,w) bifurcation diagrams (right column) as predicted by numerical solution of the mean field model (Equations (7.08) and (7.09)) for two values of b : (a) 0.2 and (b) 0.1. All other parameters were hold fixed at the values specified in Table (7.01), with X_0 = 0.4 and Y_0 = 3. Different colors in the maps indicate the number of intersections of the (X, Y, coswt) attractor with the Poincaré plane coswt = 1. Very complex periodicity or even chaotic behavior may be found in regions inside the black areas (10 or more intersections). Dashed lines in the bifurcation diagrams show in more detail the transitions from periodicity to chaos or vice-versa depicted in Figures (7.02) and (7.04) and predicted by the mean field model.

method (Equation (7.06)). The most remarkable prediction of the parameter maps in Figure (7.05) is that, by imposing confinement to a system, a dramatic change of the oscillatory pattern in comparison to the bulk behavior may be observed even at relatively large values of thickness. Take as an example the case when b = 0.1 and w = 0.82l. The reaction oscillates periodically in the bulk but the transition to chaotic behavior is already observed at thicknesses of approximately 60 molecular layers. Unfortunately, this could not be tested by molecular simulations due to the high sensitivity in these regions, meaning that the results would be strongly masked by fluctuations. The high sensitivity of chemical oscillations is not observed in other reactions such as the case of polymerization treated in Chapter 4, where confinement plays a significant role only at thicknesses smaller than a few molecular layers.

An interesting feature of the periodically forced Brusselator is the reported dependence of the oscillatory behavior on the initial concentrations X_0 and Y_0 [Hao'83]. Since this happens only in specific regions of the parameter space with very high sensitivity, the effect could be investigated in the present work only by the mean field approach and not by molecular simulations. Figure (7.06) shows the oscillatory behavior obtained by the solution of the nonlinear differential equations for a reaction taking place initially in the bulk. The parameters adopted are those listed in Table (7.01) with b = 0.1 and w = 0.817l. The initial concentrations X_0 and Y_0 were 0.3 and 3.14, respectively. There is a barely recognizable transient time in the beginning but the reaction soon reaches periodicity. At $t = 5 \times 10^4$, the system is suddenly confined in a lamella with thickness d = 10. In the mean field approach, this is taken into account by a sharp change of the value of the rate constants as predicted by Equations (7.08) and (7.09). After another short transient time, the system acquires a different oscillatory pattern, which is still periodic but with smaller amplitude. By releasing confinement and returning the reaction to the bulk condition at the appropriate time ($t = 1 \times 10^5$), chaotic behavior is observed, as indicated by the Fourier spectrum in Figure (7.06). The same bulk system that was previously periodic has been now irreversibly driven to chaos. The reason for this is that the values of X, Y and coswt at the very moment when confinement was released act as the starting conditions for the new bulk system. By releasing confinement at the appropriate time, this conditions may be considerably different from those selected at t = 0, so that the system assumes a completely different oscillatory regime. Figure (7.07) maybe illustrates better the

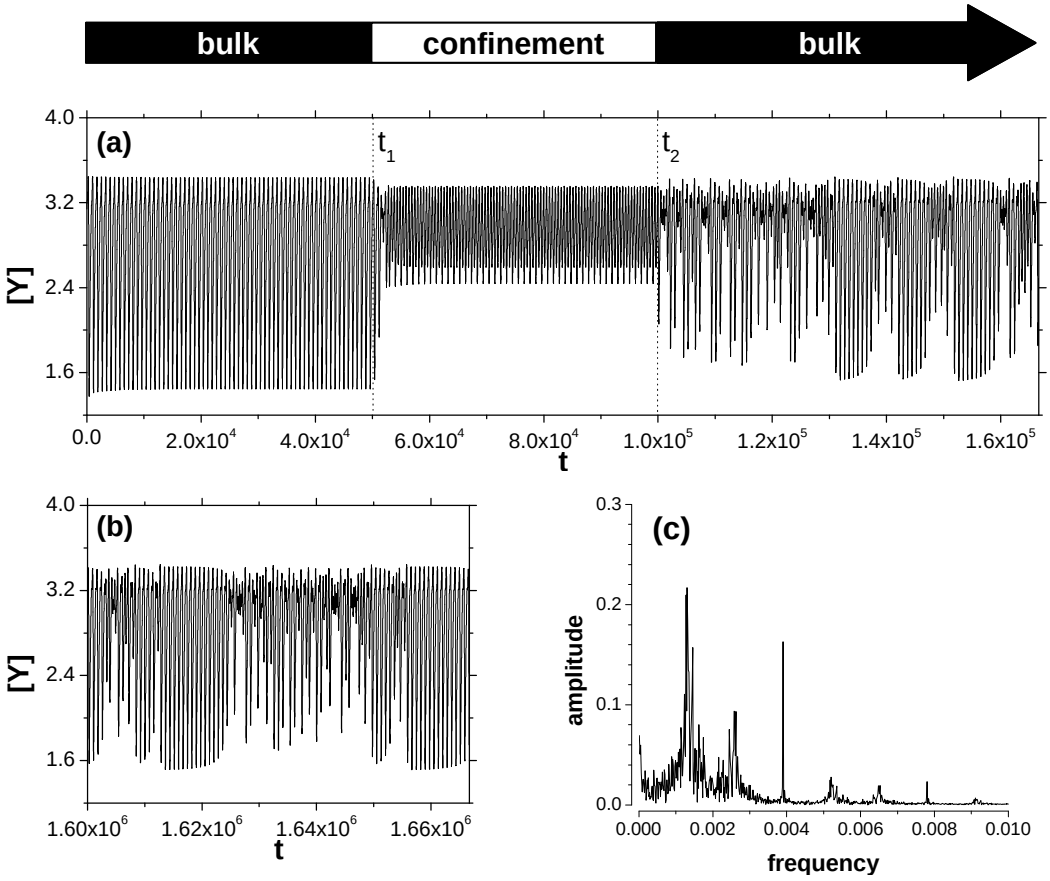

Figure 7.06 (a) Time series obtained by numerical solution of the mean field model (Equations (7.08) and (7.09)) in a region of the parameter space very sensible to initial conditions. The parameters are those from Table (7.01) with $b = 0.1$, $w = 0.817\,l$, $X_0 = 0.3$ and $Y_0 = 3.14$. The arrow on top specifies the confinement conditions imposed to the systems as function of time. At $t_1 = 5 \times 10^4$, confinement at $d = 10$ is imposed and released only at $t_2 = 1 \times 10^5$, driving the system to an oscillatory regime which is completely different from the one it had in the beginning. (b) Time series at later times and (c) the correspondent Fourier spectrum.

idea behind it by showing how the phenomenon can be explored in the inverse way, i.e., to generate an irreversible change from chaos to periodicity. Both time series depicted in Figure (7.07) have exactly the same parameters and initial conditions as the case previously discussed. At $t = 3.5 \times 10^4$, both systems are perturbed by suddenly adding X and Y to them so that $\Delta X = 0.5$ and $\Delta Y = 1$. This drives the systems to chaos (we calculated more extensive time series than those exhibited here to be sure it was chaos and not only a transient period). At $t = 7 \times 10^4$, the systems were drastically confined in a bylayer ($d = 2$) and reached a different periodic regime. After some time, confinement was released in the first system and the chaotic

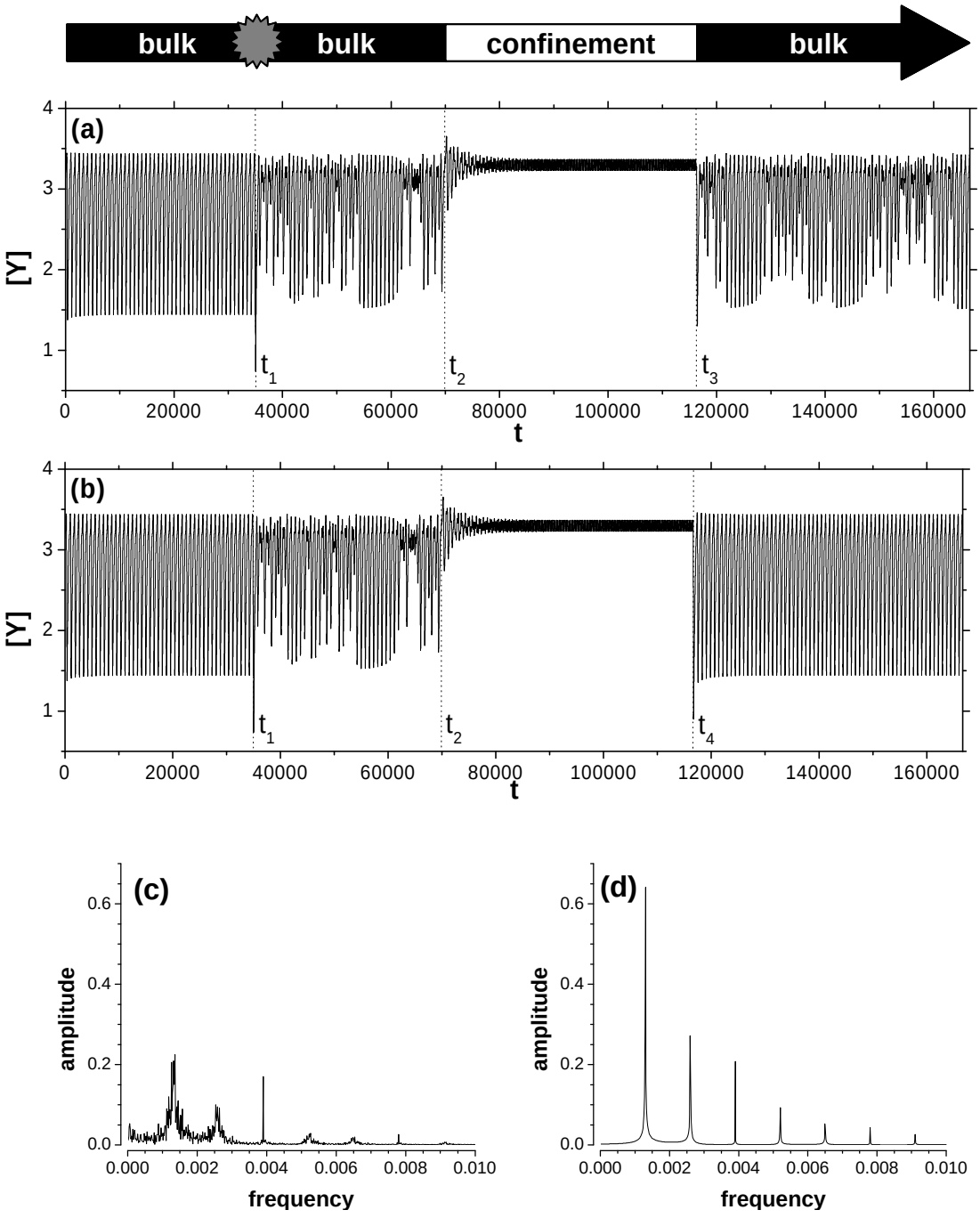

Figure 7.07 Time series obtained by numerical solution of the mean field model (Equations (7.08) and (7.09)) in a region of the parameter space very sensible to initial conditions. The parameters are those from Table (7.01) with $b = 0.1$, $w = 0.817\,l$, $X_0 = 0.3$ and $Y_0 = 3.14$. The arrow on top specifies the confinement conditions imposed to the systems as function of time. The grey star represents an external perturbation at $t_1 = 3.5 \times 10^4$ characterized by $\Delta X = 0.5$ and $\Delta Y = 1$. At $t_2 = 7 \times 10^4$, confinement is imposed with $d = 2$ and released at two different times: (a) in the first case, at t_3, giving rise to chaotic behavior, and (b) in the second case at $t_4 \sim t_3 + 330$, generating periodic behavior. Fourier spectra (c) and (d) correspond to the time series (a) and (b), respectively (at later times, after the release of confinement).

behavior induced after the perturbation was retrieved. In the second system, however, confinement was released with a delay $\Delta t \sim 330$ which is very small but enough to generate a behavior completely different from the previous one. While in the first case chaos was retrieved, in the second one the system reached the periodic behavior it had before the perturbation. Releasing the confinement in the two systems at slightly different times produces two scenarios, each one having different initial conditions and consequently different oscillatory patterns. Special attention should be paid to these calculations because they are in a very sensitive region of the parameter space and the results may exhibit dependence on the mesh size selected for the solution of Equation (7.06).

7.5 Final Considerations

In the present work, we have demonstrated by means of molecular simulations that the oscillatory regime of a hypothetical chemical reaction following the mechanism of the periodically forced Brusselator may be drastically changed by geometrical confinement. Reactions which are periodic in the bulk may burst into chaos when confined in a lamella. Analogously, chaotic reactions in the bulk may become periodic in confined geometries. This means that, in particular cases, confinement may be applied to control chaos.

To explain the confinement effect, we proposed a mean field lattice model, according to which the reaction rate constants change as function of confinement due to the lower number of realization possibilities associated to reactions attempted close to the walls. Each rate constant is affected by a different extent depending on the reaction molecularity. Since the reaction cascade in the periodically forced Brusselator is constituted by reactions with different molecularities, confinement has a remarkable impact. Of course, the model developed here is far simpler than real examples and should not be inadvertently compared to experimental systems such as the BZ reaction involving dozens of steps. The work performed here is rather intended to serve as a proof of principle that boundary effects may have a great impact over oscillating reactions, which are *per se* already very sensitive to external conditions. We hope the ideas developed here will encourage experimental investigation of

individual cases, respecting the own complexity of each one. Furthermore, we would like to call attention to the fact that the cell machinery, where oscillatory biochemical processes occur, is essentially a confined environment, with pores, interstices and channels [Minton'92]. This suggests that, to understand the chemical phenomena taking place *in vivo*, confinement may be a key issue.

Using the mean-field model, we speculated about the possibility of changing irreversibly the oscillatory behavior of a given bulk system by placing it for short time under parallel walls and then returning it to the bulk condition. However, simulations at these regions did not provide fruitful results because they were highly masked by noise. The problem remains open but could be possibly overcome by increased computational resources.

Finally, we consider as possible extensions of the simulations performed here the implementation of van der Waals interactions between molecules and the walls. It is known that the proximity between molecules and walls may change the molecular electronic configurations and consequently the activation energies for different reactions. In the work presented here, simulated systems were constantly homogenized. However, it would also be interesting to perform these simulations under the condition of low diffusivity of molecules. The CMA method could be very helpful to simulate that, in the sense that molecules would need to diffuse in a collective way. Rustici *et al.* found that the oscillatory regime of the BZ reaction can be driven from chaos to periodicity by the presence of micelles in the solution [Rustici'01]. The phenomenon was explained by the increase of viscosity and consequent decrease of the molecular mobility in the solution containing micelles. Reduced molecular mobility is known to give rise to spatial patterns of concentration in the reactor [Epstein'96]. Under appropriate conditions, these patterns may become stationary structures, the so called *Turing patterns* [Agladze'92, Epstein'96, Kondepudi'98]. There have been propositions that such phenomenon contributes in part to biological morphogenesis [Kondepudi'98]. Therefore, it would be very interesting to investigate the effects of restricted mobility in confined geometries as well.

8

Summary

The *cooperative motion algorithm* was applied on the molecular simulation of complex chemical reactions and macromolecular orientation phenomena in confined geometries.

First, we investigated the case of equilibrium step-growth polymerization in lamellae, pores and droplets. In such systems, confinement was quantified as the area/volume ratio. Results showed that, as confinement increases, polymerization becomes slower and the average molecular weight (MW) at equilibrium decreases. This is caused by the sterical hindrance imposed by the walls since chain growth reactions in their close vicinity have less realization possibilities. For reactions inside droplets at surfaces, contact angles usually increased after polymerization to compensate conformation restrictions imposed by confinement upon growing chains.

In a second investigation, we considered monodisperse and chemically inert chains and focused on the effect of confinement on chain orientation. Simulations of thin polymer films showed that chains are preferably oriented parallel to the surface. Orientation increases as MW increases or as film thickness *d* decreases, in qualitative agreement with experiments with low MW polystyrene. It is demonstrated that the orientation of simulated chains results from a size effect, being a function of the ratio between chain end-to-end distance and *d*. This study was complemented by experiments with thin films of π-conjugated polymers like MEH-PPV. Anisotropic refractive index measurements were used to analyze chain orientation. With increasing MW, orientation is enhanced. However, for MEH-PPV, orientation does not depend on *d* even at thicknesses much larger than the chain contour length. This

contradiction with simulations was discussed by considering additional causes for orientation, for instance the appearance of nematic-like ordering in polymer films.

In another investigation, we simulated droplet evaporation at soluble surfaces and reproduced the formation of wells surrounded by ringlike deposits at the surface, as observed experimentally. In our simulations, swollen substrate particles migrate to the border of the droplet to minimize the contact between solvent and vacuum, which costs the most energy. Deposit formation in the beginning of evaporation results in pinning of the droplet. When polymer chains at the substrate surface have strong uniaxial orientation, the resulting pattern is no longer similar to a ring but to a pair of half-moons.

In a final stage, as an extension for the model developed for polymerization in nanoreactors, we studied the effect of geometrical confinement on a hypothetical oscillating reaction following the mechanism of the so called *periodically forced Brusselator*. It was shown that a reaction which is chaotic in the bulk may be driven to periodicity by confinement and vice-versa, opening new perspectives for chaos control.

References

[Agladze'92] K. Agladze, E. Dulos and P. De Kepper, *J. Phys. Chem.* **1992**, *96*, 2400.

[Atkins'02] P. W. Atkins and J. de Paula, *Atkins' Physical Chemistry*; Oxford: Oxford, 2002.

[Bahtiar'04] A. Bahtiar, *Optical Waveguides of Conjugated Polymers for All-Optical Switching Devices*; Ph. D. dissertation, University of Mainz: Germany, 2004.

[Baschnagel'95] J. Baschnagel and K. Binder, *Macromolecules* **1995**, *28*, 6808.

[Berry'80] R. S. Berry, S. A. Rice and J. Ross, *Physical Chemistry*; Wiley: New York, 1980.

[Binder'04] K. Binder, M. Müller and J. Baschnagel, *Polymer Models on the lattice*. In *Simulation Methods for Polymers*; M. Kotelyanskii and D. N. Theodorou, Eds.; Marcel Dekker: New York, 2004.

[Blossey'02] R. Blossey and A. Bosio, *Langmuir* **2002**, *18*, 2952.

[Boese'92] D. Boese, H. Lee, D. Y. Yoon, J. D. Swalen and J. F. Rabolt, *J. Polym. Sci.: Part B: Polym. Phys.* **1992**, *30*, 1321.

[Bonaccurso'05] E. Bonaccurso, H.-J. Butt, B. Hankeln, B. Niesenhaus, and K. Graf, *Appl. Phys. Lett.* **2005**, *86*, 124101.

[Bornside'89] D. E. Bornside, C. W. Macosko and L. E. Scriven, *J. Appl. Phys.* **1989**, *66*, 5185.

[Bueche'62] F. Bueche, *Physical Properties of Polymers*; Interscience: New York, London, 1962; pp 22 – 23.

[Butt'03] H.-J. Butt, K. Graf and M. Kappl, *Physics and Chemistry of Interfaces*; Wiley-VCH: Weinheim, 2003.

[Caballero'03] F. V. Caballero and L. Vicente, *Chem. Eng. Sci.* **2003**, *58*, 5087.

[Carslaw'86] H. S. Carslaw and J. C. Jaeger, *Conduction of Heat in Solids*; Clarendon: Oxford, 1986.

[Castellan'83] G. W. Castellan, *Physical Chemistry*; Addison-Wesley, 1983.

[Chen'02] S.-H. Chen, A.-C. Su, Y.-F. Huang, C.-H. Su, G.-Y. Peng and S.-A. Chen, *Macromolecules* **2002**, *35*, 4229.

[Chen'04] S. H. Chen, A. C. Su, H. L. Chou, K. Y. Peng and S. A. Chen, *Macromolecules* **2004**, *37*, 167.

[Coburn'94] J. C. Coburn, M. T. Pottiger, S. C. Noe and S. D. Senturia, *J. Polym. Sci.: Part B: Polym. Phys.* **1994**, *32*, 1271.

[Cordeiro'05] R. M. Cordeiro and T. Pakula, *J. Phys. Chem. B* **2005**, *109*, 4152.

[Crank'85] J. Crank, *The Mathematics of Diffusion*; Clarendon: Oxford, 1985.

[Creutz'83] M. Creutz, *Phys. Rev. Lett.* **1983**, *50*, 1411.

[Deegan'97] R. D. Deegan, O. Bakajin, T. F. Dupont, G. Huber, S. R. Nagel and T. A. Witten, *Nature* **1997**, *389*, 827.

[Deegan'00] R. D. Deegan, O. Bakajin, T. F. Dupont, G. Huber, S. R. Nagel and T. A. Witten, *Phys. Rev. E* **2000**, *62*, 756.

[de Gans'04] B.-J. de Gans and U. S. Schubert, *Langmuir* **2004**, *20*, 7789.

[de Gennes'02] P. G. de Gennes, *Eur. Phys. J. E* **2002**, *7*, 31.

[Diao'05] J. Diao and D. W. Hess, *Thin Solid Films* **2005**, *483*, 226.

[Doi'86] M. Doi and S. F. Edwards, *The Theory of Polymer Dynamics*; Clarendon: Oxford, 1986.

[Doi'96] M. Doi, *Introduction to Polymer Physics*; Clarendon: Oxford, 1996.

[Doruker'02] P. Doruker, *Polymer* **2002**, *43*, 425.

[Eisenberg'90] A. Eisenberg, B. Hird and R. B. Moore, *Macromolecules* **1990**, *23*, 4098.

[Epstein'96] I. R. Epstein and K. Showalter, *J. Phys. Chem.* **1996**, *100*, 13132.

[Fitrilawati'02] F. Fitrilawati, M. O. Tjia, S. Pfeiffer, H.-H. Hörhold, A. Deutesfeld, H. Eichner and C. Bubeck, *Opt. Mater.* **2002**, *21*, 511.

[Frank'96] C. W. Frank, V. Rao, M. M. Despotopoulou, R. F. W. Pease, W. D. Hinsberg, R. D. Miller and J. F. Rabolt, *Science* **1996**, *273*, 912.

[Friend'99] R. H. Friend, R. W. Gymer, A. B. Holmes, J. H. Burroughes, R. N. Marks, C. Taliani, D. D. C. Bradley, D. A. dos Santos, J. L. Brédas, M. Lögdlund and W. R. Salaneck, *Nature* **1999**, *397*, 121.

[Gauger'93] A. Gauger, A. Weyersberg and T. Pakula, *Makromol. Chem., Theory Simul.* **1993**, *2*, 531.

[Geysermans'96] P. Geysermans and F. Baras, *J. Chem. Phys.* **1996**, *105*, 1402.

[Geysermans'97] P. Geysermans and F. Baras, *Europhys. Lett.* **1997**, *40*, 1.

[Gonuguntla'04] M. Gonuguntla and A. Sharma, *Langmuir* **2004**, *20*, 3456.

[Gonze'03] D. Gonze, J. Halloy, J.-C. Leloup and A. Goldbeter, *C. R. Biol.* **2003**, *326*, 189.

[Guevara'81] M. R. Guevara, L. Glass and A. Shrier, *Science* **1981**, *214*, 1350.

[Guggenheim'45] E. A. Guggenheim, *J. Chem. Phys.* **1945**, *13*, 253.

[Guggenheim'85] E. A. Guggenheim, *Thermodynamics, An Advanced Treatment for Chemists and Physicists*; North-Holland: Amsterdam, 1985.

[Györgyi'92] L. Györgyi and R. J. Field, *Nature* **1992**, *355*, 808.

[Hao'83] B.-L. Hao, G.-R. Wang and S.-Y. Zhang, *Commun. in Theor. Phys.* **1983**, *2*, 1075.

[Hasegawa'96] M. Hasegawa, T. Matano, Y. Shindo and T. Sugimura, *Macromolecules* **1996**, *29*, 7897.

[Hill'86] T. L. Hill, *An Introduction to Statistical Thermodynamics*; Dover: New York, 1986.

[Hu'00] D. Hu, J. Yu, K. Wong, B. Bagchi, P. J. Rossky and P. F. Barbara, *Nature* **2000**, *405*, 1030.

[Hu'02] H. Hu and R. G. Larson, *J. Phys. Chem. B* **2002**, *106*, 1334.

[Hu'05] H. Hu and R. G. Larson, *Langmuir* **2005**, *21*, 3963; H. Hu and R. G. Larson, *Langmuir* **2005**, *21*, 3972.

[Hu'06] H. Hu and R. G. Larson, *J. Phys. Chem. B* **2006**, *110*, 7091.

[Jia'02] W. Jia and H. Qiu, *Int. J. Mass Heat Trans.* **2002**, *45*, 4141.

[Jordan'94] D. W. Jordan and P. Smith, *Mathematical Techniques: An Introduction for the Engineering, Physical, and Mathematical Sciences*; Oxford: Oxford, 1994.

[Karabasheva'06] S. Karabasheva, S. Baluschev and K. Graf, *Appl. Phys. Lett.* **2006**, *89*, 031110.

[Kawase'01] T. Kawase, H. Sirringhaus, R. H. Friend and T. Shimoda, *Adv. Mater.* **2001**, *13*, 1601.

[Kondepudi'98] D. Kondepudi and I. Prigogine, *Modern Thermodynamics: From Heat Engines to Dissipative Structures*; Wiley: Chichester, 1998.

[Kotelyanskii'04] M. Kotelyanskii and D. N. Theodorou, *Background*. In *Simulation Methods for Polymers*; M. Kotelyanskii and D. N. Theodorou, Eds.; Marcel Dekker: New York, 2004.

[Koynov'04] K. Koynov, A. Bahtiar, T. Ahn, H.-H. Hörhold and C. Bubeck, *Appl. Phys. Lett.* **2004**, *84*, 3792.

[Koynov'06] K. Koynov, A. Bahtiar, T. Ahn, R. M. Cordeiro, H.-H. Hörhold and C. Bubeck, *Macromolecules* **2006**, *39*, 8692.

[Kruel'90] T.-M. Kruel, A. Freund and F. W. Schneider, *J. Chem. Phys.* **1990**, *93*, 416.

[Kuhn'00] H. Kuhn and H.-D. Försterling, *Principles of Physical Chemistry: Understanding Molecules, Molecular Assemblies, Supramolecular Machines*; Wiley: Chichester, 2000.

[Kumar'88] S. K. Kumar, M. Vacatello and D. Y. Yoon, *J. Chem. Phys.* **1988**, *89*, 5206.

[Kumar'90] S. K. Kumar, M. Vacatello and D. Y. Yoon, *Macromolecules* **1990**, *23*, 2189.

[Landau'00] D. P. Landau and K. Binder, *A Guide to Monte Carlo Simulations in Statistical Physics*; Cambridge: Cambridge, 2000.

[Law'00] C. W. Y. Law, K. S. Wong, Z. Yang, L. E. Horsburgh and A. P. Monkman, *Appl. Phys. Lett.* **2000**, *76*, 1416.

[Lee'03] C. Lee, J. Seo, Y. Shul and H. Han, *Polym. J.* **2003**, 35, 578.

[Li'97] F. Li, K. Kim, E. P. Savitski, J. Chen, F. W. Harris and S. Z. D. Cheng, *Polymer* **1997**, *38*, 3223.

[Li'99] B. Li, T. He and M. Ding, *Polymer* **1999**, *40*, 789.

[Li'04] Q. S. Li and R. Zhu, *Chaos, Solitons & Fractals* **2004**, *19*, 195.

[Li'06] G. Li, N. Höhn and K. Graf, *Appl. Phys. Lett.* **2006**, *89*, 241920.

[Lin'93] L. Lin and S. A. Bidstrup, *J. Appl. Polym. Sci.* **1993**, *49*, 1277.

[Lin'94] L. Lin and S. A. Bidstrup, *J. Appl. Polym. Sci.* **1994**, *54*, 553.

[Lísal'06] M. Lísal, J. K. Brennan and W. R. Smith, *J. Chem. Phys.* **2006**, *124*, 064712.

[Liu'96] J.-X. Liu, W.-M. Zheng and B.-L. Hao, *Chaos, Solitons & Fractals* **1996**, *7*, 1427.

[Losurdo'03] M. Losurdo, M. M. Giangregorio, P. Capezzuto, G. Bruno, F. Babudri, D. Colangiuli, G. M. Farinola and F. Naso, *Macromolecules* **2003**, *36*, 4492.

[Lotka'10] A. J. Lotka, *J. Phys. Chem.* **1910**, *14*, 271.

[Lotka'20] A. J. Lotka, *J. Am. Chem. Soc.* **1920**, *42*, 1595.

[Luck'91] W. A. P. Luck, *How to Understand Liquids?* In *Intermolecular Forces, An Introduction to Modern Methods and Results*; P. L. Huyskens, W. A. P.Luck and T. Zeegers-Huyskens, Eds.; Springer: Berlin, 1991; pp 55- 78.

[McBranch'95] D. McBranch, I. H. Campbell, D. L. Smith and J. P. Ferraris, *Appl. Phys. Lett.* **1995**, *66*, 1175.

[McGehee'00] M. D. McGehee and A. J. Heeger, *Adv. Mater.* **2000**, *22*, 1655.

[McQuarrie'76] D. A. McQuarrie, *Statistical Mechanics*; Harper Collins: New York, 1976.

[Metropolis'53] N. Metropolis, A. N. Rosenbluth, M. N. Rosenbluth, A. H. Teller and E. Teller, *J. Chem. Phys.* **1953**, *21*, 1087.

[Milchev'02] A. Milchev, *Eur. Phys. J. E* **2002**, *8*, 531.

[Minton'92] A. P. Minton, *Biophys. J.* **1992**, *63*, 1090.

[Morii'04] N. Morii, G. Kido, H. Suzuki, S. Nimori and H. Morii, *Biomacromolecules* **2004**, *5*, 2297.

[Ozawa'05] K. Ozawa, E. Nishitani and M. Doi, *Jpn. J. Appl. Phys.* **2005**, *44*, 4229.

[Pakula'91] T. Pakula, *J. Chem. Phys.* **1991**, *95*, 4685; T. Pakula and E. B. Zhulina, *J. Chem. Phys.* **1991**, *95*, 4691.

[Pakula'00a] T. Pakula and K. Harre, *Comp. Theor. Polym. Sci.* **2000**, *10*, 197.

[Pakula'00b] T. Pakula, *J. Mol. Liquids* **2000**, *86*, 109.

[Pakula'04] T. Pakula, *Simulations on the Completely Occupied Lattice*. In *Simulation Methods for Polymers*; M. Kotelyanskii and D. N. Theodorou, Eds.; Marcel Dekker: New York, 2004.

[Parisse'96] F. Parisse and C. Allain, *J. Phys. II* **1996**, *6*, 1111.

[Parisse'97] F. Parisse and C. Allain, *Langmuir* **1997**, *13*, 3598.

[Pauchard'03] L. Pauchard and C. Allain, *Phys. Rev. E* **2003**, *68*, 052801; L. Pauchard and C. Allain, *C. R. Phys.* **2003**, *4*, 231.

[Petrov'93] V. Petrov, V. Gáspár, J. Masere and K. Showalter, *Nature* **1993**, *361*, 240.

[Picknett'77] R. G. Picknett and R. Bexon, *J. Colloid Interface Sci.* **1977,** *61*, 336.

[Picu'03] R. C. Picu and M. S. Ozmusul, *J. Chem. Phys.* **2003**, *118*, 11239.

[Press'88] W. H. Press, B. P. Flannery, S. A. Teukolsky and W. T. Vetterling, *Numerical Recipes in C: The Art of Scientific Computing*; Cambridge: Cambridge, 1988.

[Prest'79] W. M. Prest and D. J. Luca, *J. Appl. Phys.* **1979**, *50*, 6067.

[Prest'80] W. M. Prest and D. J. Luca, *J. Appl. Phys.* **1980**, *51*, 5170.

[Provata'93] A. Provata, J. W. Turner and G. Nicolis, *J. Stat. Phys.* **1993**, *70*, 1195.

[Provata'99] A. Provata, G. Nicolis and F. Baras, *J. Chem. Phys.* **1999**, *110*, 8361.

[Ree'94] M. Ree, C. Chu and M. J. Goldberg, *J. Appl. Phys.* **1994**, *75*, 1410.

[Rouault'97] Y. Rouault and A. Milchev, *Macromol. Theory Simul.* **1997**, *6*, 1177.

[Rowlinson'84] J. S. Rowlinson and B. Widom, *Molecular Theory of Capilarity*; Clarendon: Oxford, 1984; pp 173- 189.

[Russel'83] T. P. Russel, H. Gugger and J. D. Swalen, *J. Polym. Sci.: Polym. Phys. Ed.* **1983**, *21*, 1745.

[Rustici'01] M. Rustici, R. Lombardo, M. Mangone, C. Sbriziolo, V. Zambrano and M. L. T. Liveri, *Faraday Discuss.* **2001**, *120*, 39.

[Schabel'03] W. Schabel, P. Scharfer, M. Müller, I. Ludwig and M. Kind, *Chem. Ing. Tech.* **2003**, *75*, 1336.

[Schmidt'01] H. Schmidt, *Präparation und Charakterisierung dünner Schichten aus Polymeren*; private report, 2001.

[Schmitt'93] V. Schmitt, F. Lequeux and C. M. Marques, *J. Phys. II* **1993**, *3*, 891.

[Schubert'97] D. W. Schubert, *Polym. Bull.* **1997**, *38*, 177.

[Sequeira'03] C. Stupperich-Sequeira, K. Graf and W. Wiechert, *Conference Proceedings 4th Mathmod*. In: *ARGESIM-Reports*; I. Troch and F. Breitenecker, Eds.; Vienna, 2003.

[Sequeira'06] C. Stupperich-Sequeira, K. Graf and W. Wiechert, *Math. Comput. Model. Dyn. Syst.* **2006**, *12*, 263.

[Spangler'90] L. L. Spangler, J. M. Torkelson and J. S. Royal, *Polym. Eng. Sci.* **1990**, *30*, 644.

[Strogatz'94] S. H. Strogatz, *Nonlinear Dynamics and Chaos With Applications to Physics, Biology, Chemistry, and Engineering*; Perseus Books: Reading, 1994.

[Tammer'02] M. Tammer and A. P. Monkman, *Adv. Mater.* **2002**, *14*, 210.

[Tanford'61] C. Tanford, *Physical Chemistry of Macromolecules*; Wiley: New York, 1961.

[Thomas'03] A. Thomas, S. Polarz and M. Antonietti, *J. Phys. Chem. B* **2003**, *107*, 5081.

[Thompson'84] S. M. Thompson, K. E. Gubbins, J. P. R. B. Walton, R. A. R. Chantry and J. S. Rowlinson, *J. Chem. Phys.* **1984**, *81*, 530.

[Tien'70] P. K. Tien and R. Ulrich, *J. Opt. Soc. Am.* **1970**, *60*, 1325.

[Tien'77] P. K. Tien, *Rev. Mod. Phys.* **1977**, *49*, 361.

[Tribet'94] C. Tribet, A. Provata and G. Nicolis, *J. Chem. Phys.* **1994**, *100*, 6082.

[Tsige'04] M. Tsige and G. S. Grest, *Macromolecules* **2004**, *37*, 4333.

[Uno'98] K. Uno, K. Hayashi, T. Hayashi, K. Ito and H. Kitano, *Colloid Polym. Sci.* **1998**, *276*, 810.

[Vacatello'02] M. Vacatello, *Macromol. Theory Simul.* **2002**, *11*, 53.

[Vonna'05] L. Vonna, L. Limozin, A. Roth and E. Sackmann, *Langmuir* **2005**, *21*, 9635.

[Wang'97] H. Wang and H. Xin, *J. Chem. Phys.* **1997**, *107*, 6681.

[Wang'00] H. Wang and Q.-S. Li, *Phys. Chem. Chem. Phys.* **2000**, *2*, 1951.

[Wittmer'98] J. P. Wittmer, A. Milchev and M. E. Cates, *J. Chem. Phys.* **1998**, *109*, 834.

[Yang'95] Y. Yang, A. Kloczkowski, J. E. Mark, B. Erman and I. Bahar, *Macromolecules* **1995**, *28*, 4920.

[Zhao'93] W. Zhao, M. H. Rafailovich, J. Sokolov, L. J. Fetters, R. Plano, M. K. Sanyal, S. K. Sinha and B. B. Sauer, *Phys. Rev. Lett.* **1993**, *70*, 1453.

[Zhdanov'01] V. P. Zhdanov, *Phys. Chem. Chem. Phys.* **2001**, *3*, 1432.

[Zhokhavets'04] U. Zhokhavets, G. Gobsch, H. Hoppe and N. S. Sariciftci, *Thin Solid Films* **2004**, *451-452*, 69.

[Zollweg'71] J. Zollweg, G. Hawkins and G. B. Benedek, *Phys. Rev. Lett.* **1971**, *27*, 1182.

List of Publications

1. R. M. Cordeiro and T. Pakula, “Behavior of Evaporating Droplets at Nonsoluble and Soluble Surfaces: Modeling with Molecular Resolution”, *J. Phys. Chem. B* **2005**, *109*, pp. 4152 – 4161.

2. K. Koynov, A. Bahtiar, T. Ahn, R. M. Cordeiro, H.-H. Hörhold and C. Bubeck, “Molecular Weight Dependence of Chain Orientation and Optical Constants of Thin Films of the Conjugated Polymer MEH-PPV”, *Macromolecules* **2006**, *39*, 8692 – 8698.